Georgia State University

ScholarWorks @ Georgia State University

Physics and Astronomy Dissertations

Department of Physics and Astronomy

5-4-2020

Migration Enhanced Plasma Assisted Metal Organic Chemical Vapor Deposition of Indium Nitride

Zaheer Ahmad

Follow this and additional works at: https://scholarworks.gsu.edu/phy_astr_diss

Recommended Citation

Ahmad, Zaheer, "Migration Enhanced Plasma Assisted Metal Organic Chemical Vapor Deposition of Indium Nitride." Dissertation, Georgia State University, 2020.

doi: https://doi.org/10.57709/17572142

This Dissertation is brought to you for free and open access by the Department of Physics and Astronomy at ScholarWorks @ Georgia State University. It has been accepted for inclusion in Physics and Astronomy Dissertations by an authorized administrator of ScholarWorks @ Georgia State University. For more information, please contact scholarworks@gsu.edu.

MIGRATION ENHANCED PLASMA ASSISTED METAL ORGANIC CHEMICAL VAPOR DEPOSITION OF INDIUM NITRIDE

by

ZAHEER AHMAD

Under the Direction of Alexander Kozhanov, PhD

ABSTRACT

The influence of various plasma species on the growth and structural properties of indium nitride in migration-enhanced plasma-assisted metalorganic chemical vapor deposition (MEPA-MOCVD). The atomic nitrogen ions' flux has been found to have a significant effect on the growth rate as well as the crystalline quality of indium nitride. No apparent effect of atomic neutrals, molecular ions, and neutral nitrogen molecules has been observed on either the growth rate or crystalline quality.

A thermodynamic supersaturation model for plasma-assisted metalorganic chemical vapor deposition of InN has also been developed. The model is based on the chemical combination of

indium with plasma-generated atomic nitrogen ions. In supersaturation was analyzed for indium nitride films grown by PA-MOCVD with varying input flow of indium precursor. Raman spectroscopy, X-Ray diffraction, and atomic force microscopy provided feedback on structural properties and surface morphology of grown films. We found that InN films grown at widely different growth conditions but with the same supersaturation exhibit similar structural properties and surface morphology.

The effect of various growth parameters on the plasma potential has also been discussed. The plasma potential has been found to depend on the concentration of atomic nitrogen ions. The samples grown at increased plasma potential have exhibited better optoelectronic properties than the those grown at lower plasma potential.

INDEX WORDS: Indium nitride, Plasma assisted deposition, Metalorganics, FTIR, Raman spectroscopy, XRD, Optical microscopy.

MIGRATION ENHANCED PLASMA ASSISTED METAL ORGANIC CHEMICAL VAPOR DEPOSITION OF INDIUM NITRIDE

by

ZAHEER AHMAD

A Dissertation Submitted in Partial Fulfillment of the Requirements for the Degree of

Doctor of Philosophy

in the College of Arts and Sciences

Georgia State University

2020

Copyright by
Zaheer Ahmad
2020

MIGRATION ENHANCED PLASMA ASSISTED METAL ORGANIC CHEMICAL VAPOR DEPOSITION OF INDIUM NITRIDE

by

ZAHEER AHMAD

Committee Chair: Alexander Kozhanov

Committee: Sidong Lei

Vadym Apalkov

Fabien Baron

Electronic Version Approved:

Office of Graduate Services

College of Arts and Sciences

Georgia State University

May 2020

DEDICATION

This work is dedicated to my grandfather Mr. Gul Zaman, my parents Mr. Shabir Ahmad and Mrs. Rukhsana, my siblings Junaid, Komal and Wishma and my fiancé Ayesha.

ACKNOWLEDGEMENTS

I would like to thank my academic advisor Dr. Alexander Kozhanov for his guidance and support during my whole tenure of PhD at Georgia State University. His working method of providing me complete freedom to pursue my research projects independently and at the same time giving important suggestions from time to time to keep the projects focused and research-oriented, made my PhD project a learning and exciting experience. I would also like to acknowledge my funding sources US Department of Energy, Pacific Northwest National Laboratories and National Science Foundation.

I would like to extend my sincere gratitude to Dr. Daniel Deocampo for providing access to his XRD facility, Brendan Cross for help with FTIR and AFM studies of InN films and Mark Vernon for valuable discussions on supersaturation calculations and for help on PA-MOCVD reactor. I would also like to extend my sincere gratitude to Daniel Seidlitz for the initial training on PA-MOCVD reactor. I would like to acknowledge my fellow graduate students especially Rupesh Ghimire and Kushan Wijewardena and technical staff at Department of Physics and Astronomy for their help, support and jokes during the course of my PhD.

I would like to pay my tributes to my first Doctoral Advisor Late Dr. Nikolaus Dietz and to my high school teacher and my first mentor in the Physics research, Dr. Younas Khan.

Finally, I would like to thank my parents, Mr. Shabir and Mrs. Rukhsana, for their love and sacrifices and my brother Junaid and sisters Komal and Wishma, for their continuous love and affection throughout my life.

TABLE OF CONTENTS

ACKNOWLEDGEMENTS V

LIST OF TABLES IX

LIST OF FIGURES X

LIST OF ABBREVIATIONS XIV

1 INTRODUCTION 1

2 INDIUM NITRIDE 4

2.1 Indium nitride synthesis 4

2.2 Crystal Structure 10

2.3 Lattice Strains 12

2.4 Band structure 14

2.5 Effective mass 16

2.1 Phonon structure 17

3 EXPERIMENTAL METHODS 18

3.1 Substrates for indium nitride growth 18

3.2 Thin films epitaxy by Metal-Organic Chemical Vapor Deposition (MOCVD) 20

3.3 Precursors and their packaging 22

3.4 Gas manifold 25

3.5 Reaction chamber 26

3.6 Growth process 27

3.7 Characterization techniques 28

3.8 Raman spectroscopy 28

3.9 X-ray diffraction (XRD) 36

3.10 FTIR 40

3.11 Atomic force microscopy (AFM) 41

4 INFLUENCE OF PLASMA ACTIVATED NITROGEN ON INDIUM NITRIDE GROWTH 43

4.1 Introduction 43

4.2 Sample growth 45

4.3 Plasma emission spectroscopy measurements 47

4.4 Results and discussion 53

4.4.1FTIR measurements 53

4.4.2 Impact of RF power on plasma parameters 55

4.4.3 Atomic nitrogen ions are the main contributors from nitrogen plasma 56

4.4.4 Impact of nitrogen plasma species on InN structural properties 58

4.5 Conclusions 61

5 SUPER-STURATION MODEL FOR INDIUM NITRIDE PA-MOCVD 62

5.1 Supersaturation 62

5.2 Calculation of supersaturation 63

5.3 Sample growth 68

5.4 Results and discussion 70

5.4.1 Influence of indium supersaturation on structural properties of InN 70

5.4.2 Influence of indium supersaturation on the surface morphology of InN 77

5.5 Conclusions 77

6 IMPACT OF PLASMA POTENTIAL ON INDIUM NITRIDE PA-MOCVD GROWTH KINETICS AND STRUCTURAL PROPERTIES 79

6.1 Plasma potential and plasma sheath 79

6.2 Plasma sheath dynamics 80

6.3 Sample growth, plasma potential measurement and emission spectra acquisition 84

6.4 Correlation of plasma potential (V_P) with various plasma species 86

6.5 The impact of plasma potential on structural properties of InN 93

6.6 Conclusions 97

7 CONCLUSIONS 98

REFERENCES 101

LIST OF TABLES

Table 3.1 Lattice constant for InN and its potential substrates and their % lattice 19

Table 3.2 Physical properties of commercially available metalorganics 24

Table 3.3 Character table and the symmetry operation for C_{6v} point group symmetry................33

Table 3.4 The phonon modes associated with a unit cell with N basis atoms 35

Table 4.1 Growth conditions for three sets used in this study of InN growth..............................45

Table 4.2 Boltzmann plot for the N+ spectral lines (dots) and its linear fit (dashed line) 50

Table 4.3 Fitting parameters for the plasma emission spectra from sample set A 51

Table 4.4 Fitting parameters for plasma emission spectra from sample set B 51

Table 5.1 The growth conditions used for sample sets D and E. For set D the supersaturation was varied by varying the input indium. For set E, three samples grown at widely different growth conditions resulting into indium supersaturation ~ 2 68

Table 5.2 Phonon relaxation time for sample sets D and E. For set A the supersaturation was varied by varying the input indium. For set E, three samples grown at widely different growth conditions resulting into indium supersaturation of 2 73

Table 5.3 The crystallite sizes in (0002) direction determined from XRD for sample set B grown at indium supersaturation ~ 2..75

Table 5.4 Growth rate vs. supersaturation for sample sets D. The supersaturation was varied by varying the input indium...76

Table 6.1 Growth conditions for sample sets A, B and C 84

Table 6.2 Growth conditions for set D; the grid bias series 86

LIST OF FIGURES

Figure 2.1 The allotropic forms of indium nitride crystal lattice 11

Figure 2.2 Schematic of high-symmetry crystalline planes in wurtzite indium nitride................12

Figure 2.3 First Brillouin zone and the symmetry points of the hexagonal structure..................14

Figure 2.4 Schematic of energy band structure at Γ point for InN 15

Figure 2.5 The dependence of bandgap on lattice constant for wurtzite structure 15

Figure 3.1 A schematic diagram of three most frequently occurring growth modes on a flat surface substrate 21

Figure 3.2 Thin film growth regimes according to the substrate temperature 22

Figure 3.3 Schematic drawing of a metalorganic bubbler...24

Figure 3.4 Schematic of gas manifold used for precursor delivery to reaction chamber with plasma-assisted MOCVD system in the present study...25

Figure 3.5 Schematic of a plasma-assisted MOCVD reaction chamber (left) and reaction kinetics on substrate surface (right)..27

Figure 3.6 The fundamental interaction of light with a molecule in Raman scattering................29

Figure 3.7 Jablonski diagram for Rayleigh and Raman scattering processes 30

Figure 3.8 Schematic of Raman scattering measurement system used in this work 31

Figure 3.9 Optical phonon modes of wurtzite structure...36

Figure 3.10 Schematic representation of x-ray diffraction; Bragg's diffraction (left) and relationship of the incident, diffracted, and scattering vectors with respect to the crystal37

Figure 3.11 The example geometry for the X-ray diffractometer and sample reference frame with axes of rotation. The φ axis is normal to sample while ω is in plane with the sample......39

Figure 3.12 Schematic of FTIR measurement system 40

Figure 3.13 A schematic of a typical AFM [153] 42

Figure 4.1 Growth conditions for sample set B 46

Figure 4.2 (Left) The optical emission spectrum of nitrogen plasma at RF power ~ 300W and 2..2 Torr reactor pressure. The boxed section represents the the spectral range used to analyze the plasma composition in the present study. (Right) Nitrogen plasma glow......47

Figure 4.3 Nitrogen emission spectrum (solid line) and its multi-peak fit (dashed line) measured above the sample surface. N+ spectral transitions are labelled.......................................48

Figure 4.4 Boltzmann plot for the N+ spectral lines (dots) and its linear fit (dashed line)...........50

Figure 4.5 InN growth rate and nitrogen plasma species concentrations dependence on plasma power level for sample sets A (a), B (b), and C (c)...53

Figure 4.6 FTIR spectra fitting for sample set A 54

Figure 4.7 FTIR spectra fitting for sample set B 54

Figure 4.8 FTIR spectra fitting for sample set C 55

Figure 4.9 The film growth rate as a function of atomic nitrogen ion flux for three different sets of samples 57

Figure 4.10 Raman spectra measured on InN films plotted for set A (a), set B (b) and Set C (c) . Numbers indicate the RF power levels. (d) The E2-high phonon mode relaxation time dependence on nitrogen ion flux 58

Figure 4.11 Example fitting of the Raman spectra measured on InN films plotted on the InN sample grown at 450W in set C. The phonon modes are labelled 59

Figure 4.12 XRD spectra measured on InN films grown at 2.2Torr, V/III ratio of 57, at varying RF powers indicated in the legend 61

Figure 5.1 The dependence of supersaturation on substrate temperature 66

Figure 5.2 The dependence of supersaturation on reactor pressure 67

Figure 5.3 The dependence of supersaturation on input trimethyl indium 67

Figure 5.4 Growth conditions for sample set D..69

Figure 5.5 Raman spectra measured on InN films plotted for set D. Numbers indicate the indium supersaturation levels 71

Figure 5.6 Raman spectra measured on InN films plotted for set E. Numbers indicate the growth conditions resulting in indium supersaturation level of 2...71

Figure 5.7 The E2-high and A1-LO phonon mode relaxation time dependence on indium supersaturation level for set A. 72

Figure 5.8 XRD spectra measured on InN films grown at widely different conditions, all of which result into Indium supersaturation level 2 74

Figure 5.9 Experimental IR reflectance spectra measured on InN films plotted for set D and their simulated fitting..76

Figure 5.10 Surface morphology measured on InN films plotted for set E via Atomic Force Microscopy. Numbers at the bottom of each image indicate the growth conditions resulting in indium supersaturation level of 2...77

Figure 6.1 Schematic of the electric potential distribution in the remote PA-MOCVD system. OES represents the optical emission spectroscopy (distances are not to the scale) 80

Figure 6.2 Variation in plasma potential and plasma composition with plasma N_2 flow rate 89

Figure 6.3 Variation in plasma potential and plasma composition with reactor pressure 90

Figure 6.4 Variation in plasma potential and plasma composition with plasma RF power..........91

Figure 6.5 Variation in plasma composition with plasma grid bias. $V = 0$ at the dotted line 92

Figure 6.6 The dependence of plasma potential on the concentration of atomic ions 93

Figure 6.7 Raman spectra for the sample set A 94

Figure 6.8 Raman spectra for the sample set B 95

Figure 6.9 Raman spectra for the sample set C 95

Figure 6.10 Raman spectra for the sample set D 96

Figure 6.11 The impact of plasma potential on the E2-high phonon mode relaxation time 96

Figure 7.1 InN quantum dots on GaN, grown by migration-enhanced plasma-assisted MOCVD (MEPA-MOCVD) 100

LIST OF ABBREVIATIONS

Abbreviation	Meaning
CVD	Chemical vapor deposition
MOVPE	Metalorganic vapor phase epitaxy
MOCVD	Metalorganic chemical vapor deposition
MEPA-MOCVD	Migration-enhanced plasma-assisted metalorganic chemical vapor deposition
RF-MBE	Radio frequency molecular beam epitaxy
ALD	Atomic layer deposition
XRD	X-ray diffraction
FTIR	Fourier transform infrared spectroscopy
InN	Indium nitride
InGaN	Indium gallium nitride
AlGaN	Aluminum gallium nitride
TMI	Trimethyl indium
TEI	Trimethyl indium
MFC	Mass flow controller
FWHM	Full width at half maximum

1 INTRODUCTION

Indium nitride is a significant III-nitride semiconductor with numerous possible applications. The alloys of InN with other III-nitrides (e.g., InN) made it possible to extend the emission of III-nitride LEDs from UV to IR[2]'[3-5]'[8, 9]'[10]. The effective electron mass was predicted to be lowest for InN among III-nitrides semiconductors[11]. InN is to exhibit the highest peak overshoot velocity, and InN based FETs are predicted to have an extremely high speed. A two-junction tandem solar cell as InN a top cell material[12] can obtain a conversion efficiency of over 30%. The growth and integration of InN and In-rich alloys such as InGaN and InGaAlN also opens doors for the fabrication of Terra Hertz detectors and emitters[13], applications as chemical sensor[14], and highly-efficient energy conversion device applications like solid-state lightning[15], tandem photovoltaics[15], and solid integrated LED displays[16].

This thesis is focused on establishing the growth physics of InN thin films by migration-enhanced plasma-assisted MOCVD (MEPA-MOCVD) method and to understand their physical characteristics. The research methodology followed in this research is to optimize the migration-enhanced plasma-assisted MOCVD growth for indium nitride and its alloys, for possible novel device applications. The outline of the thesis is described in the following.

Chapter 2 concisely gives a review of the history indium nitride research, a discussion on its physical properties, a report on the various methods, and challenges in the growth of InN and its alloys.

Chapter 3 gives a detailed discussion of the thin film growth system used in the present study and on the various spectroscopic and surface characterization techniques. A discussion on the underlying physics and methods of probing InN thin film structural, crystallographic, optical,

and optoelectronic characteristics by Raman spectroscopy, X-ray diffraction (XRD), and Fourier transform infrared (FTIR) reflection spectroscopy and Atomic force microscopy (AFM).

Chapter 4 gives a detailed overview of the influence of various plasma species on InN growth chemistry and its structural properties. The chapter provides an in-depth discussion on the methods of atomic emission spectroscopy to determine the plasma composition and the energies of various plasma species from an in-situ emission spectrum of the plasma.

Chapter 5 provides a detailed discussion on a thermodynamic supersaturation model. The author developed the supersaturation model for plasma-assisted metalorganic chemical vapor deposition of InN. It is based on the chemical combination of indium with plasma-generated atomic nitrogen ions. Indium supersaturation was analyzed for InN films grown by PA-MOCVD with varying input flow of indium precursor. Atomic force microscopy, Raman spectroscopy and X-ray diffraction provided feedback on surface morphology and structural properties of grown films. The growth parameter variation effect on indium supersaturation was analyzed. It was also found that the InN films that were grown at varying growth parameters resulting in the same In supersaturation value exhibit similar structural properties and surface morphology.

Chapter 6 gives a detailed overview of the possibility to control the growth, morphology, and structural properties in InN thin films by varying the electric potential on a grid above the growth surface. A systematic change in the grid potential above the substrate alters the ion flux onto the substrate accordingly, which is otherwise dictated by the floating potential of the grid. The floating potential at the grid is the result of a continuous bombardment of the various plasma species onto the grid. It is the function of different process parameters such as chamber pressure, nitrogen flow through plasma source, and the plasma power. Hence an external control over the grid potential may result in high crystalline quality thin films in parameter space, which would

otherwise result in the films with relatively poor crystalline quality. The dependence of plasma potential on the growth parameters such as chamber pressure, plasma N_2 flow, and RF power is also discussed in detail. A study on the variation of grid potential in the range -100V to 100V and its effect on morphology, crystalline quality, and growth rate of the resulting InN thin films is presented.

Finally, Chapter 7 gives a summary of the research results and proposes future directions for the potential applications of this research.

2 INDIUM NITRIDE

2.1 Indium nitride synthesis

The first synthesis of InN was achieved by Juza and Hahn in 1938, who produced powdered InN by the decomposition of $(NH_4)_3InF_6$ in ammonia (NH_3) stream. They reported the InN crystal structure as wurtzite with lattice parameters a = 3.53 Å and c = 5.69 Å.[17] Between 1940 to 1960 InN growth methods adopted were either by chemical reactions of various indium compounds with ammonia or thermal decompositions of complex compounds[18],[19],[20]. The first CVD growth of InN was attempted by Pastrnak et al. in1963. They grew InN by chemical reaction between $InCl_3$ and N_2 gas [21]. It was established that the synthesis of InN is not possible by direct reaction of In metal with nitrogen gas in an inactivated form even at very high temperature [22],[23].

A study by McChesney et al. [24] in 1970 suggested that the InN dissociation temperature is ~527°C at atmospheric pressure, and low growth temperatures has to be utilized to synthesize InN. The first plasma assisted growth of InN was achieved by Hovel et al. in 1970. InN was grown by reactive RF sputtering using In target and pure N_2 [25]. They grew polycrystalline and n-type InN films on Si and sapphire substrates, that had high carrier concentrations of ~$(5\text{-}8)\times10^{18}$ cm^{-3}. Bandgap was measured to be 1.9 eV.

Tansley et al. reported, room temperature, low background carrier concentration ~ 5.3×10^{16} cm^{-3} and high Hall mobility ~ 2700 $cm^2V^{-1}s^{-1}$ in polycrystalline InN films grown by sputtering on Si and glass substrates[26]. The bandgap energy of these films was updated to 1.89 eV[27].

Mosaic crystalline epitaxial InN layers were grown by Marasina et al. in 1977 chemical vapor deposition[28] (CVD). The growth was achieved by the chemical reaction of $InCl_3$ with ammonia NH_3 on sapphire (0001) substrates. The samples were n-type with electron concentration ~ 8×10^{21} to 2×10^{20} cm^{-3} and Hall mobility ~ 35 - 50 $cm^2V^{-1}s^{-1}$.

Between 1940 and 1970 it was established that single crystal InN is difficult to grow compared to GaN and AlN, mainly because of the lower dissociation temperature of InN. Wakahara et al. in 1989 reported that they achieved epitaxial growth of InN on sapphire. The growth was performed by microwave-excited metalorganic vapor phase epitaxy (ME-MOVPE) at the growth temperatures of 400-600°C[29].

In the same year, Yuichi et al. reported the epitaxial growth of InN on a GaAs substrate ((111)A and (100) oriented) by RF-excited reactive evaporation. The films were of fairly good crystalline quality with XRD rocking curve full width at half-maximum (FWHM) of 17 s. [30] InN and $In_xGa_{1-x}N$ was also grown on sapphire by Matasuoka et al. [31] and later reproduced by Yamamto et al. [32] using MOVPE.

Ability to grow highly crystalline InN films lead to the update of its bandgap value first to 0.9 eV [33] in 2001 and then to 0.7 eV later [34],[35].

As-grown InN films were usually found to be n-type, while unintentional p-doping occurred rarely. Jenkins et al. investigated the doping and electronic structure InGaN, InAlN and InN in 1989, and concluded that the nitrogen vacancies induce the n-doping[36]. For the first time, Feiler et al. [37] used pulsed laser deposition (PLD) to grow unintentionally doped InN films on sapphire (0001) at 5 mTorr growth pressures. The films were polycrystalline with mobility in the range 30 $cm^2V^{-1}s^{-1}$ and 240 $cm^2V^{-1}s^{-1}$ and the carrier concentration in range ~ 6.5×10^{20} cm^{-3} and 4.7×10^{19} cm^{-3}. Butcher et al. showed in 2004 that the high n-type carrier concentration for RF sputtered InN films originated from excess nitrogen instead of nitrogen vacancies[38].

Many groups have predicted the mobility of InN e.g. Chin et al. predicted that the maximum mobility of the InN to be 4400 $cm^2V^{-1}s^{-1}$ at room temperature and 33000 $cm^2V^{-1}s^{-1}$ at 77 K [39]. Similarly predicted highest value of mobility at room temperature for InN films by

Nag et al. was around 4000 $cm^2V^{-1}s^{-1}$. However, none of these predictions were close to the experimentally reported values.

Fareed et al. used migration enhanced metalorganic chemical vapor deposition to grow InN films on GaN/Al_2O_3 and found the dependence of carrier concentration and mobility on the film thickness [40]. They found, when the InN film thickness increases from 75 nm to 900 nm the carrier concertation varies form 5.5×10^{19} cm^{-3} to 4.1×10^{18} cm^{-3} and mobility varies from 12 $cm^2V^{-1}s^{-1}$ to 846 $cm^2V^{-1}s^{-1}$. The increased film thickness caused to decrease the lattice strains and reduction of defects.

Sato et al. found the carrier concentration and mobility to decrease with decreased growth rates [41]'[42]. In their studies using plasma-assisted MOCVD when the growth rate dropped from 230 nm/h to 50 nm/h, the carrier concentration decreased from 3.2×10^{20} cm^{-3} to 4.3×10^{18} cm^{-3} and mobility decreased from 34.7 $cm^2V^{-1}s^{-1}$ to 0.6 $cm^2V^{-1}s^{-1}$. At the lower rates the adatoms had to more time to find lower energy sites in the lattice and hence better film with improved electrical properties.

Guo et al.[43] investigated the dependence of the carrier concentration and mobility of InN films deposited by RF magnetron sputtering. They found that with the increase in substrate temperature from 100°C to 500°C carrier concentration remained ~10^{20} cm^{-3} and the mobility increased from 18 $cm^2V^{-1}s^{-1}$ to 115 $cm^2V^{-1}s^{-1}$. In the same year Ikuta et al. [44] grew InN films using ZnO as a buffer layer on (0001) sapphire. They found that Hall mobility of the films grown on the ZnO buffer was higher (60 $cm^2V^{-1}s^{-1}$) compared to the ones on bare sapphire (30 $cm^2V^{-1}s^{-1}$) at the same growth conditions. Yamaguchi et al.[45] grew InN on GaN for first time by MOVPE.

Typical MOCVD growth temperature window for Ga and Al based nitrides is between 900°C and 1200°C. While indium based nitrides such as InN, InGaN, and InAlN require low

temperature growth because of the relatively weak In and N bond. Atomic layer epitaxy (ALE) was suggested as a solution to this problem[46],[47],[48],[49].

The lower substrate temperature for InN growth reduces the surface migration of In ad-atoms resulting in indium droplet formation and high defect density in the resulting films. In migration enhanced epitaxy (MEE), gas pulsing allows In ad-atoms more time on the surface to find energetically optimal final position. This allows InN growth at lower substrate temperatures [50]. Lu et al. investigated the InN layers deposited by MEE on sapphire. The highest mobility of 542 $cm^2V^{-1}s^{-1}$ and lowest electron carrier concentration of 3×10^{18} cm^{-3} at room temperature were found at the growth temperatures around 500°C[50]. This study also indicated that a AlN buffer layer between InN and spphire substrate may be used to improve the electrical properties of InN films. Further studies of the effect of the AlN buffer layer on the epitaxial growth of InN by MBE were carried out later by Lu et al.[51]. They found a Hall mobility of 805.3 $cm^2V^{-1}s^{-1}$ with a carrier concentration ~2.5×10^{18} cm^{-3} at room temperature of InN film grown on AlN buffer layer[51].

In 2003, Lu et al. reported no apparent improvement of electrical properties of InN films with thickness[52]. They also reported the improvement of Hall mobility due to the reduced defect density away from the lattice-mismatched buffer. For the *c*-plane film, Lu et al. found that impurities from the growth environment are not responsible for the high background doping of InN [94, 95]. However, for *a*-plane InN, a significant decrease of structural defects along the growth direction were not observed[52].

Inushima et al. successfully deposited 15nm InN film using plasma-assisted MBE on sapphire with reported bandgap of 0.89eV, carrier concentration of 5×10^{19} cm^{-3} and mobility of 1700 $cm^2V^{-1}s^{-1}$ [33]. In 2001, Yoshiki et al. used RF-MBE to deposit single crystal InN layers on sapphire (0001) with an intermediate InN nucelation layer grown at 300 °C. The highest mobility

and lowest carrier concentration of 760 $cm^2V^{-1}s^{-1}$ and 3×10^{19} cm^{-3} were measured for films grown at 550°C substrate temperature and 240W RF power[53].

Raman and IR reflectance spectra of InN films grown on GaAs (111) and sapphire (0001) by microwave excited MOVPE and RF magnetron sputtering were studied by Qian et al.[54] In the Raman spectra, A_1(LO) modes at 589 cm^{-1} and E_2(high) modes at 490 cm^{-1} were observed. A blue shift in the frequencies for the E_1(TO) and A_1(LO) phonon modes was attributed to the residual compressive stress. In the IR spectra, phonon modes of A_1(TO) at 449 cm^{-1}, E_1(TO) at 488 cm^{-1}, free carrier concentration and mobility were extracted. The electrical characteristics of the films extracted from IR spectra were smaller than those from Hall measurements. According to Qian et al. this discrepancy is due to the increased scattering for the carrier coupling with the incident phonons in the optical measurements[54].

Goldhahn et al. studied InN properties by spectroscopic ellipsometry. They extracted the anisotropic dielectric function of the *a*-plane InN layers deposited on *r*-plane sapphire with an AlN nucleation layer and a GaN buffer[55]. The dielectric function from IR to ultraviolet range by spectroscopic ellipsometry for InN films was later studied by Kasic et al.[56] They determined plasma frequency, plasma damping and film thickness of InN layers with free carrier concentrations in the range 7.7×10^{17} cm^{-3}- 1.4×10^{19} cm^{-3}. Yang et al. studied the extinction coefficient and refractive index as a function of energy with different growth conditions for InN films on GaAs (111) grown by RF reactive magnetron sputtering[57].

Yamamoto et al. showed that improvement of surface morphology is needed to achieve high electron mobility in InN films using atomic force microscopy (AFM). Films used in the study were grown by MOVPE at atmospheric pressure[58]. Further improvement in the electrical properties of the InN is one of the known challenges[23]. The quality of InN films is also sensitive

to surface preparation steps especially nitridation of the substrates[59]. The nitridation of substrate has been investigated by various researchers using various techniques[60]'[61]'[62]'[63]. According to Pan et al. the film quality of InN film is sensitive to the mechanism of nitridation, specifically the nitridation period and temperature at which nitridation is performed. They showed that nitridation of sapphire for 40 minutes at 1000°C improves quality of InN films grown on it[64]'[65]. However, the prolonged nitridation and very high temperatures are not helpful for electrical properties, surface morphology and crystalline quality of the films as shown by Maleyre et al.[66]. Drago et al.[67] optimized the nitridation conditions using ammonia in MOVPE for the best InN quality that resulted in electron mobility of ~450 $cm^2V^{-1}s^{-1}$ and electron concentration of ~6×10^{18} cm^{-3}. Skuridina et al.[68] discovered the formation of a crystalline AlN layer during the nitridation process sapphire above 800°C and deposited a single crystal plane surface of N-polar InN layer on top of AlN buffer layer. However, for the nitridation temperatures below 800°C an amorphous AlN_xO_y layer was observed that resulted in polycrystalline In-polar InN films with rough surface.

The influence of substrate polarity on the InN films deposited by MBE was investigated by Xu et al.[69] They found that FWHM of the XRD rocking curve of (0002) InN peak for N-polar films was 220 arcsec and for (0002) In-polar InN 600 arcsec. For N-polar films, the electron concentration was ~ (1 - 5) $\times10^{18}$ cm^{-3} and mobility ~ 500 - 1200 $cm^2V^{-1}s^{-1}$. For In-polar films these were in the range (4 - 10) $\times10^{18}$ cm^{-3} and 300 – 900 $cm^2V^{-1}s^{-1}$ respectively.

Lin et al.[69] investigated the properties of the InN film deposited by MOCVD on GaN/sapphire at different temperatures. The best results (mobility of 1300 $cm^2V^{-1}s^{-1}$, carrier concentration of 4.6×10^{18} cm^{-3}) were achieved for the samples grown at 625°C. High mobility of

InN layers grown with high temperature GaN and low temperature GaN buffer layer by MOCVD has been reported by Xie et al. [70].

Rich InN study history provided us with many of structural, optical, electronic and other information of InN. However, InN growth is still remains not optimized. There are also numerous controversies about its properties, including the origin of unintentional doping. Impurities, such as hydrogen, oxygen and silicon, behave as donors, dislocations also might be a source for the unintentional n-type doping of InN[71]. Himmerlich et al.[72] indicated that there is an increase in electron concentration with carbon incorporation. However, the dislocation densities are independent of carbon incorporation. Control of carbon impurities incorporation is a challenge, and InN films are usually unintentionally doped with carbon by any growth method based on gas-phase epitaxy. It is also observed that the electron mobility and concentration is affected by the edge dislocations[71],[73],[74].

2.2 Crystal Structure

Indium nitride occurs in three crystalline forms. Each of these structure exhibits different physical properties. The allotropes are wurtzite: a hexagonal α – phase structure which is thermodynamically stable under STP conditions., the zinc-blende: a cubic β – phase structure that is metastable at ambient conditions and, rock salt: a structure that forms as phase transition from the wurtzite structure at hydrostatic pressure of 21.6 GPa [75],[76],[77].

The stable crystalline forms of InN are wurtzite and the cubic structures. In both of these cases each indium atom is attached to four nitrogen atoms and vice versa. However, the difference between them lies in their stacking sequence of the close-packed diatomic plane. If the In-N-In bonds are denoted by ABC, the stacking sequence for the wurtzite structure is ABAB of (001)

close-packed plane, while for the zinc-blende the stacking structure is ABCABC of (111) close-packed plane. The wurtzite, zinc-blende, and rock salt crystalline structures of InN are shown in Fig. 2.1.

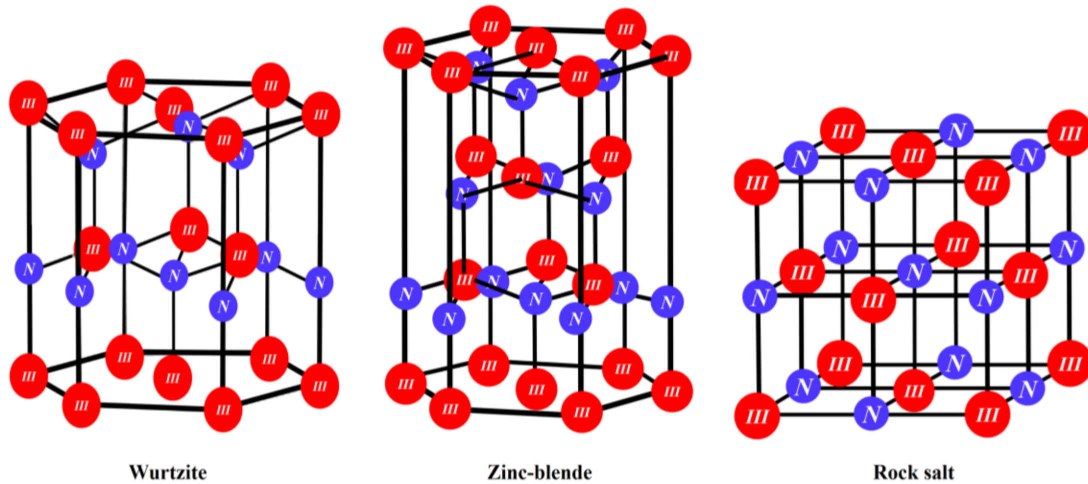

Figure 2.1 The allotropic forms of indium nitride crystal lattice

The present study will be focused on the wurtzite structure of InN. Wurtzite structure is made of two overlapped hexagonal close-packed (HCP) lattices shifted along c-axis in the [0001] direction. Fig. 2.2 demonstrates the crystal planes and axes of wurtzite structure.

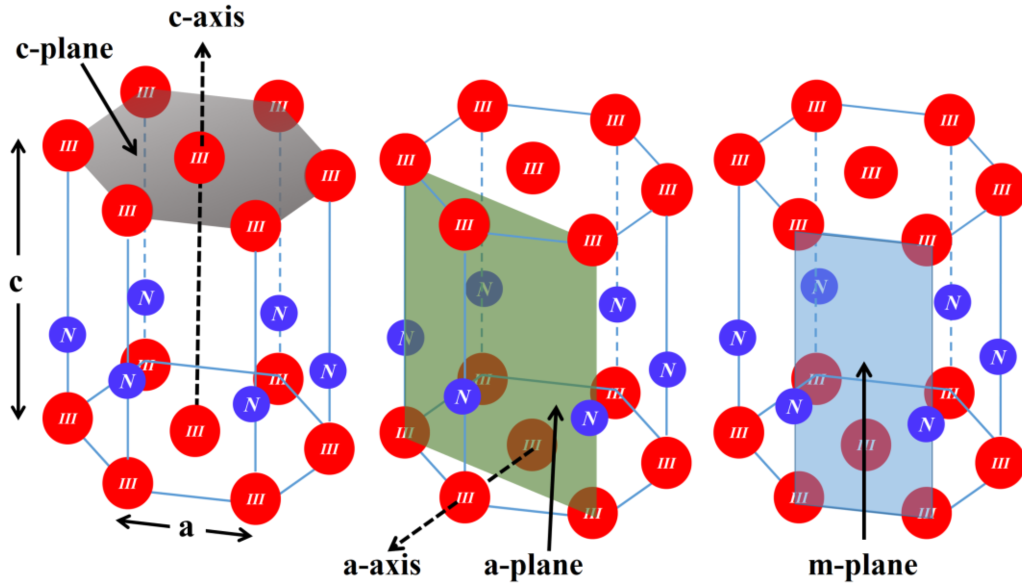

Figure 2.2 Schematic of high-symmetry crystalline planes in wurtzite indium nitride

The lattice constant *c* is the height of hexagonal prism while *a* is the side length of the hexagonal base as demonstrated in figure 2.2 [78]. The lattice constants *a* and *c* of InN films grown on sapphire or on GaN by MOCVD or MBE were found as in the range $3.501 - 3.536$ Å for a and $5.69 - 5.705$ Å for *c* [78].

The presence of residual stress and strain induced by substrate, and inhomogeneity or impurities may result in the deviation of structural properties from ones predicted on the base lattice parameters. Conversely, the information on the residual stress/strain, impurity concentrations and thermal expansion coefficients of the thin films can be extracted from the measured values (from X-ray diffraction) of the lattice parameters[79].

2.3 Lattice Strains

Generally, indium nitride thin films are grown on non-InN substrates. This process of growing one material on another is called hetero-epitaxy. The lattice mismatch between substrate

and the overgrown film gives rise to lattice strain / stress in the grown film. The strain in the film may result in crystalline defect formation. The lattice strain is large for sufficiently thin epitaxial layers, generally for a first few atomic layers, and interfaces are coherent due to these strains [80]. When the strain energy exceeds a critical threshold the system gets relaxed and certain misfit dislocations are induced by this strain [80],[81]. The difference between the thermal expansion coefficients of the substrate and the overgrown film results in residual internal strain, when the systems cools down after the overgrowth. The lattice mismatch and thermal expansion coefficient mismatch induced strain is named as biaxial strain.

If the lattice constant of the film is larger than that of the substrate, the film is said to be in a compressive strain. Conversely, when the lattice constant of the film is smaller than that of the substrate, the film will be said to have a tensile strain. The biaxial strain in a film is defined in terms of the lattice constants of the substrate and overgrown film by the equation[82],[83] 2.1.

$$\varepsilon = \frac{a_{film} - a_{substrate}}{a_{substrate}} \qquad (2.1)$$

a_{film} and $a_{substrate}$ are the lattice constants of the film and the substrate.

The physical properties of a strained film deviate from an unstrained film. For example, the surface morphology of the InN film will drastically change due to the influence of lattice strain on the surface mobility of indium ad-atoms will change during the growth [84]. Moreover, the film strain will greatly influence the lattice constant of the film, which means that the interatomic distances are affected and that will consequently change the bandgap energy of the grown film. The frequencies of phonon modes will also increase or decrease for the compressive and tensile strains respectively [84]. A measure of the lattice strain in a film can be obtained via Raman spectroscopy, transmission electron microscopy (TEM) or X-ray diffraction (XRD)[82].

2.4 Band structure

The optoelectronic properties of a semiconductor material directly depend on its bandgap and dielectric function which in turn depend on its crystal structure and electronic band structure.

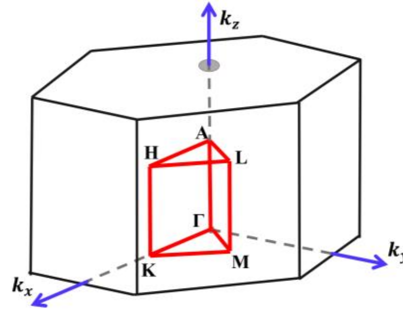

Figure 2.3 First Brillouin zone and the symmetry points of the hexagonal structure

The first Brillouin zones of wurtzite InN structure is shown in Fig. 2.3. The Γ point in the Brillouin space located at the zone center with k=0 has the highest symmetry out of the other symmetry points. For InN (and other III-nitrides as well) the Γ point is where conduction band minima and the valence band maxima occur at the same position in the k-space. Hence, all the III-nitrides are called direct bandgap semiconductors. The band structure in a wurtzite structure is affected by two basic exchange mechanism namely crystal field splitting and spin-orbit splitting. Various ab-initio and other numerical methods can be employed to calculate their band structure at the Γ point. For example, Green's function and the screened Coulomb interaction quasiparticle approach with exact-exchange optimized effective potential (OEPx) and local density approximation (LDA)[85],[86].

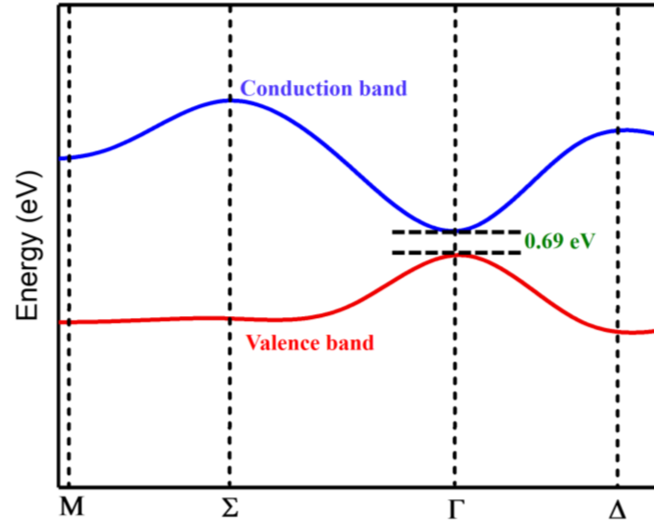

Figure 2.4 Schematic of energy band structure at Γ point for InN

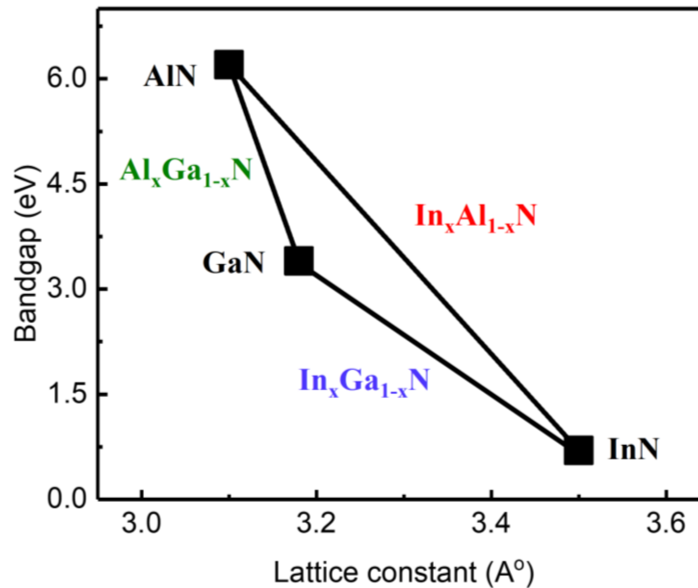

Figure 2.5 The dependence of bandgap on lattice constant for wurtzite structure

The fundamental bandgap for a material is the energy difference between the conduction band minimum and the valence band maximum, and for direct bandgap material like InN it will be located at the Γ point. The bandgap value for InN is 0.7eV[87],[88]. The dependence of bandgap for III-nitrides on the lattice parameters in shown in Fig. 2.5. It should be noted that the lattice

constant of most commonly used substrate i.e. is 4.785A° creating a lattice mismatch of about 25%.

2.5 Effective mass

The mass of electron determined experimentally, in solids deviates from the free electron mass [89]. The experimentally determined electron mass is called the effective mass (m*). The effective electron mass differs from the free electron mass due to interaction of drifting electrons with the atoms of the lattice in a solid.

The effective mass is mathematically expressed as [89]

$$m^* = \frac{h^2}{\frac{d^2E}{dk^2}} \qquad (2.2)$$

According to the equation 2.2 the effective mass is function of electronic band structure. At the Γ point in Fig. 2.4, $\frac{d^2E}{dk^2} > 0$ for conduction band bottom so the effective mass is positive. Similarly for valence band top at the same Γ point in Fig. 2.4, $\frac{d^2E}{dk^2} < 0$, hence effective mass is negative. The negative effective electron mass means a kind of particle that will accelerate opposite to that of electron in response to an electric field (hole) [89].

The effective electron mass in InN determined by high magnetic field measurements is $m^*= 0.055m_0$, where m_0 is the electron mass in vacuum [90]·[91].

2.1 Phonon structure

Phonons are quasiparticles corresponding to crystal lattice vibrations solids. Phonon modes vibrational modes can be called a “fingerprint” of given material: materials crystal structure and particular atoms its built of defines the phonon spectrum [84].

There are two major types of phonons in a solid having two or more types of atoms in its unit cell. The acoustic phonons are caused by coherent movements of atoms of the crystal about their equilibrium positions. When the lattice atoms are in vibrational motion in the direction of wave propagation, the corresponding phonons are called longitudinal and are called transverse when the vibration is perpendicular to the wave propagation. Hence the types longitudinal acoustic (LA) and transverse acoustic (TA). The optical phonons are due to out of phase movements of the atoms in the crystal structure. Following the same pattern as before, the optical phonons can also be either longitudinal optical (LO) and transverse optical (TO).

The phonon spectrum of a solid vital in defining the kinetic, optical and dynamical characteristics of the carriers especially in semiconductors [92]. Another important aspect of the phonons is their interaction with free carriers. The phonon lifetimes (can be determined directly from Raman line width) are important in determining the structural and optical properties of a material[93]. There will be a detailed discussion on the phonon structure of InN in chapter 3 in the “Raman spectroscopy” section and on the determination of phonon life time in chapter 4 in the section “Influence of plasma species on structural properties of InN”.

3 EXPERIMENTAL METHODS

There are several growth techniques resulting in epitaxial films. In this work I use MOCVD technique to grow InN films. In this chapter I give a brief introduction to the MOCVD and focus on plasma-assisted MOCVD growth technique for III-N thin-film epitaxial growth. Metalorganic chemical vapor deposition (MOCVD), also called metalorganic vapor-phase epitaxy (MOVPE) is a chemical vapor deposition process for growing crystalline semiconductor materials, which can be used to grow complex semiconductor heterostructures. Typically, the chamber pressures around 20 to 200 Torr are used during growth. MOCVD is also preferred for the fabrication of devices and is recognized as a key process in the manufacture of optoelectronics. The MOCVD process was invented in 1968 at North American Aviation Science Center by Harold M. Manasevit. In this chapter, the MOCVD growth process and its variant PA-MOCVD will be discussed in detail. There will also be a detailed discussion on the characterization techniques used for thin-film analysis in this work, namely Raman spectroscopy, X-ray diffraction, Fourier transform infrared spectroscopy (FTIR), UV-Vis Normal incidence reflectance spectroscopy (NIRS), Optical microscopy and Atomic force microscopy (AFM).

3.1 Substrates for indium nitride growth

The structural and optoelectronic properties of deposited thin films are greatly influenced by the substrates and growth processes. Hence, it is of high importance to keep the followings factors into consideration, while choosing a substrate. Firstly, the thermal mismatch of the substrate with the film to be overgrown. Secondly, the lattice mismatch of the substrate and the overgrown layer. And finally, the cost of the substrate. Several materials are used as a substrate

for III-N epitaxial growth. The lattice mismatch between the various substrates and the III-nitrides are summarized in Table 3.1.

Table 3.1 Lattice constant for InN and its potential substrates and their % lattice

Substrate	Lattice constant (A°)	% lattice mismatch
Al_2O_3	4.785	~25[1]
Si	5.43	~8
GaAs	5.65	~11.3
SiC	4.35	~14
AlN	3.11	13
GaN	3.19	~11
InN	3.53	0

3.1.1 Substrate preparation for InN growth

Sapphire (0001) is the common substrate used for III-nitride growth. It is a low-cost substrate available in different wafer sizes. It is stable at high-temperatures and has high surface and crystal quality. To overcome the lattice mismatch induced problems the buffer layers (or interlayers) are grown on sapphire instead of directly depositing a III-N layer. For example, during InN growth, inserting a GaN or AlN in between the InN film and sapphire substrate can shrink the lattice mismatch from ~25% to 11% or 13%, respectively[1]. The crystalline quality of the III-N film can also be improved by the nitridation of the sapphire substrate before III-N growth. For example, Gao. et al.[94] grew InN films on sapphire substrates nitridized by N plasma. They

showed that an ordered and flat AlN interlayer is generated on the sapphire surface during the nitridation between the substrate and the InN film[94], which improved the surface migration of In atoms on the substrate, and consequently a single-crystalline c-plane InN film of high quality can be obtained.

3.2 Thin films epitaxy by Metal-Organic Chemical Vapor Deposition (MOCVD)

Epitaxy is a thin-film deposition process onto a crystalline substrate. There are two basic types of epitaxy: homo-epitaxy and hetero-epitaxy. In the homo-epitaxy epitaxial layer is deposited on the same material (e.g., GaN on GaN). Hetero-epitaxy is when epitaxial layers of a material are deposited on a different substrate (e.g. GaN on sapphire or on Si). The process of homo-epitaxy results in high-quality films with lower defect density and doping control. However, hetero-epitaxy is often required in optoelectronic structures and bandgap engineered devices.

The three possible epitaxial growth modes are: Volmer Weber or Island growth, Frank van der Merwe or layer by layer growth, and Stranski-Krastanov or layer plus island growth.

In Volmer–Weber (VW) growth the interactions between the adatom themselves are stronger than their interactions with the surface. This leads to the formation of clusters or islands. When the interactions of adatoms with the surface are strong the layer by layer growth Frank–van der Merwe (FM) happens. Stranski–Krastanov growth is a mix of both 2D layer and 3D island growth[95][96][97].

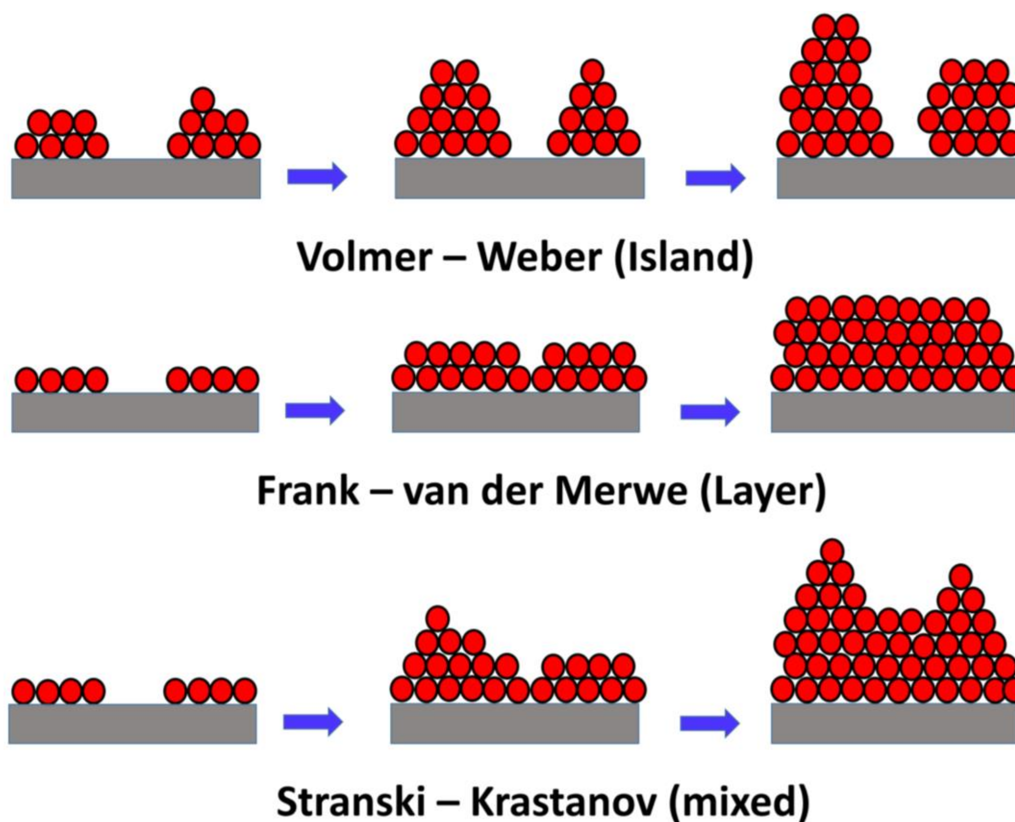

Figure 3.1 A schematic diagram of three most frequently occurring growth modes on a flat surface substrate

The occurrence of these growth modes depends on the lattice mismatch between the substrate and the film, the flux of the crystallizing phase, the growth temperature, and the adhesion energy [98]. A schematic representation of these growth modes on a flat surface substrate is shown in figuire 3.1.

This film growth in the MOCVD chamber is controlled by several growth parameters such as the substrate temperature, chamber pressure, input molar flows of group III and group V precursors, and plasma RF power (in case of plasma-assisted MOCVD). Generally, the substrate temperatures used for III-V growth range from 500 – 1200°C. The dependence of the growth rate on the substrate temperature is usually divided into three regions [99],[100],[101],[102],[103], as shown in Fig. 3.2.

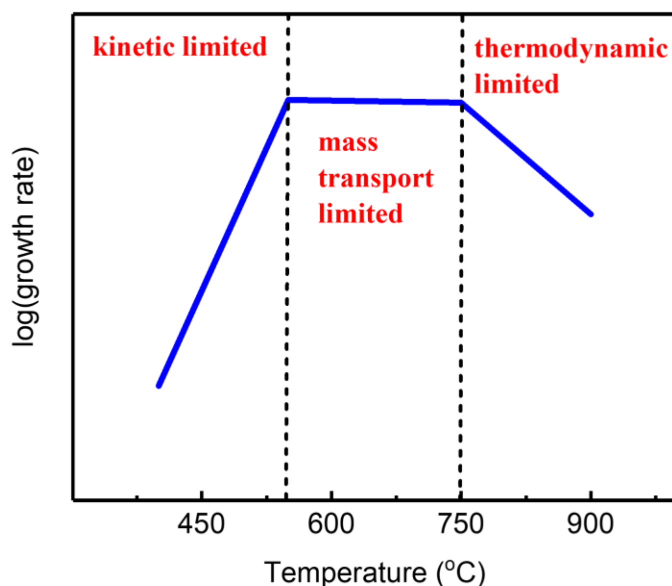

Figure 3.2 Thin film growth regimes according to the substrate temperature

At the temperatures below ~500°C, the growth rate is controlled by the gas phase reactions and by the chemical reactions that take place on the substrate surface. In the mass transport limited regime (~550°C – 750°C), the growth rate is independent of the substrate temperature and instead depends on the in-flux of the precursor flow. In the third region, the decrease in growth rate with increasing substrate temperature is due to thermodynamic effects or reactant depletion due to upstream reactions[103],[104].

Following are the four basic components of a MOCVD system, and are discussed in detail in the next sections, precursors and their packaging, gas manifold, reaction chamber and exhaust system.

3.3 Precursors and their packaging

Most commonly used group III precursors are TMA (trimethylaluminium), TEA (trimethylaluminium), TMG (trimethylgallium), TEG (trimethylgallium), TMI (trimethylindium),

and TEI (trimethylindium). Most of the mentioned above metalorganic (MO) precursors are pyrophoric, and therefore require reliable, hermetic packaging to stop the material from coming in contact with air to prevent fires. The MO compounds are usually obtained from the supplier in a package that will be directly connected to film growth system. For liquid sources, the container is in the form of a bubbler. Carrier gas (N_2 or H_2) is passed through the bottom of the material using a dip tube as shown in Figure 3.3. The carrier gas then transports the source material into the reactor. When a thermodynamic equilibrium is established between the vapor and the condensed phase, the precursor can be written as:

$$\upsilon = P_\upsilon(f_\upsilon/RT_O)P_O/P_{cyl} \qquad (3.1)$$

where υ is the MO molar flow (moles/min), P_v is MO-species vapor pressure (at given temperature), f_v is volume flow rate of carrier gas through the bubbler, R is the gas constant, To = 273°C, P_o = 1 atm, and P_{cyl} is the total pressure in the MO container. P_v can be calculated from the data in Table 3.1. Typical molar flows for MO species are in the range of 1 – 30 µmol/min.

In conventional MOCVD, NH_3 is used as the group V precursor in III-nitride growth. However, in the plasma-assisted MOCVD, plasma-activated nitrogen ions using nitrogen gas source is used as group V precursor. The N_2 (liquid) and NH_3 (gas) are usually shipped by the supplier in large cylinders that will be directly connected to the film growth system.

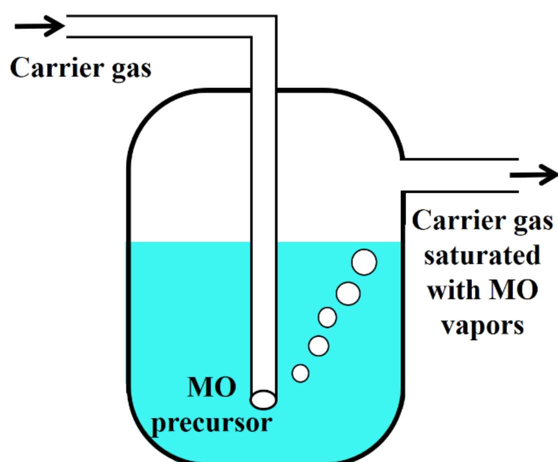

Figure 3.3 Schematic drawing of a metalorganic bubbler

Table 3.2 Physical properties of commercially available metalorganics

chemical	abbreviation	melting temp (°C)	vapor pressure (log P) (P in torr and T in K)	Use
Tri-ethyl aluminum	TEAl	-52.5	$8.999 - 2361.2/(T - 73.82)$	Al source, AlN AlGaN, InAlN
Tri-methyl aluminum	TMAl	15.4	$8.2 - 21.8/T$	Al source, AlN AlGaN, InAlN
Tri-ethyl gallium	TEGa	-82.3	$8.08 - 2162/T$	Ga source,GaN AlGaN, InGaN
Tri-methyl gallium	TMGa	-15.8	$8.07 - 1703/T$	Ga source,GaN AlGaN, InGaN
Tri-ethyl indium	TEIn		$8.93 - 2815/T$	In source, InN InAlN, InGaN
Tri-methyl indium	TMIn	88	$10.52 - 3014/T$	In source, InN InAlN, InGaN

3.4 Gas manifold

The gas manifold comprises of computer controlled valves, mass flow controllers and pipes that control the precursor flows and pressures. All the flows are must be precisely controlled without fluctuations. Any fluctuations in precursor flows can result in variations in film composition and thickness. Precursor flows may be measured accurately using mass flow controllers (MFCs). MFCs and pressure controllers are important parts of a growth system. An MFC uses a flow meter as a feedback to an electronically controlled needle valve to control the flow. The TMI flow is kept separate from N_2 precursor flows before introduction into the reaction chamber. The separation of the reactants excludes the possibility of gas phase reactions in the gas manifold pipes to avoid deposition in pipes [105].

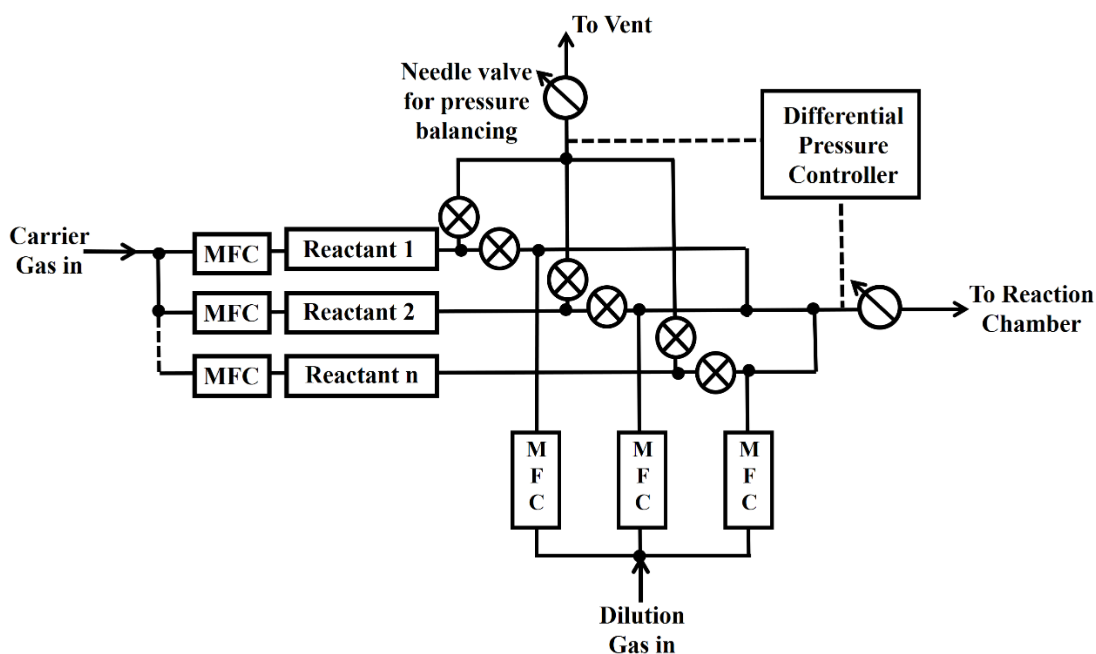

Figure 3.4 Schematic of gas manifold used for precursor delivery to reaction chamber with plasma-assisted MOCVD system in the present study

Gas manifold works in a “vent/run” configuration [106],[107], as shown in Fig 3.4. This configuration helps in making sure that precursor flows are steadily established at the intended

values to the vent before directing them to the reaction chamber. The flows are then switched from vent line to run line that goes directly to the reaction chamber to start the film growth process.

3.5 Reaction chamber

The thermal decomposition of indium precursors and the deposition reactions occur in the reaction chamber. The reaction chamber used in present study is cold walled, hence the substrate holder or susceptor is the only part of the reaction chamber that is being deliberately heated. Cooling the walls reduce the possibility of competing reactions at the walls that can affect the final yield of the deposition reaction on the substrate. Reaction chamber walls are made of stainless steel.

The reaction chamber is equipped with a N_2 flushed load lock to keep the ambient air from coming in contact with the reaction chamber during the loading and unloading of the sample. The optical access to the system is possible through the viewports. This allows measuring… The substrates are placed on the wafer carrier, that is heated from underneath using a resistive heater. The reaction chamber has vertical geometry [108],[109] in which the nitrogen plasma generated by hollow cathode plasma source comes down to the substrate to chemically react with the indium atoms as shown in figure 3.5. .

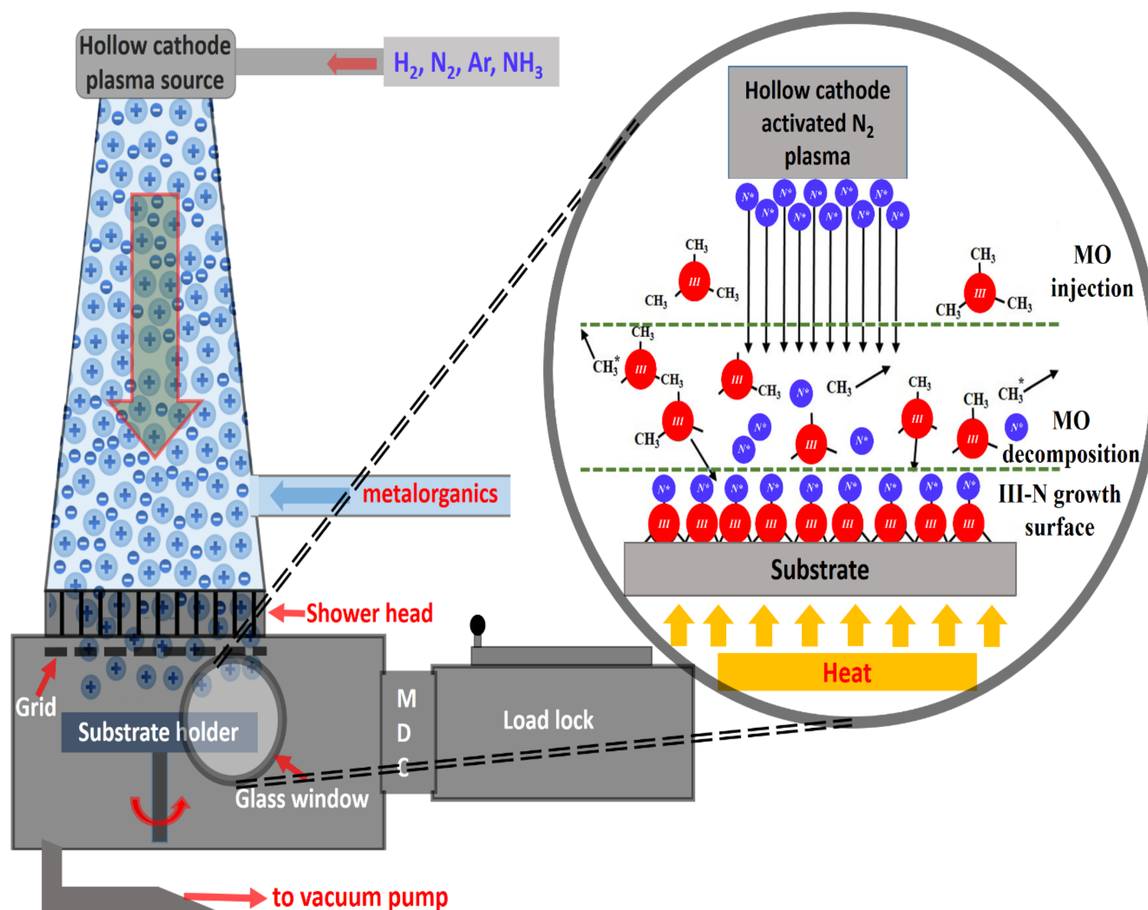

Figure 3.5 Schematic of a plasma-assisted MOCVD reaction chamber (left) and reaction kinetics on substrate surface (right)

3.6 Growth process

The growth process in the present study is as follows. TMI is injected into the chamber above the showerhead. The showerhead helps distributing the TMI evenly over the substrate surface. The decomposition of TMI occurs near to substrate due to heat coming out of the substrate. The activated nitrogen species are generated by hollow cathode plasma source operating at 13.56MHz. The chemical combination between indium and activated nitrogen species occurs at the substrate surface as shown in the insert of Fig. 3.5.

3.7 Characterization techniques

Grown indium nitride films were characterized by X-Ray diffraction (XRD), Raman spectroscopy and Fourier Transform Infrared spectroscopy (FTIR). Furthermore, the Atomic Force Microscopy (AFM) which is a non-optical method is also used to study the surface morphology of the films[110]. In this section each of the characterization method description is given as follows.

3.8 Raman spectroscopy

Raman spectroscopy is a light scattering technique, in which a very small amount of light is scattered at different wavelengths than the incident light. Incident light usually comes from a laser light source. A large percentage of the scattered light is at the same wavelength as the laser source, hence doesn’t contain any useful information on the material it is scattered from – this is called Rayleigh Scatter, there is no energy exchange of the radiation with matter and is therefore elastic scattering. But, a small quantity of light (10^{-8} %) which is scattered at different wavelengths (is therefore inelastic scattering), depends on the chemical structure of the analyte – this is called Raman Scatter. The inelastic scattering of light was theoretically predicted by A. Smekal in 1923 [111],[112] and the first experimental demonstration of this effect was achieved by C.V. Raman and K. S. Krishnan in 1928 [113]. The effect was later named after C.V. Raman as Raman effect.

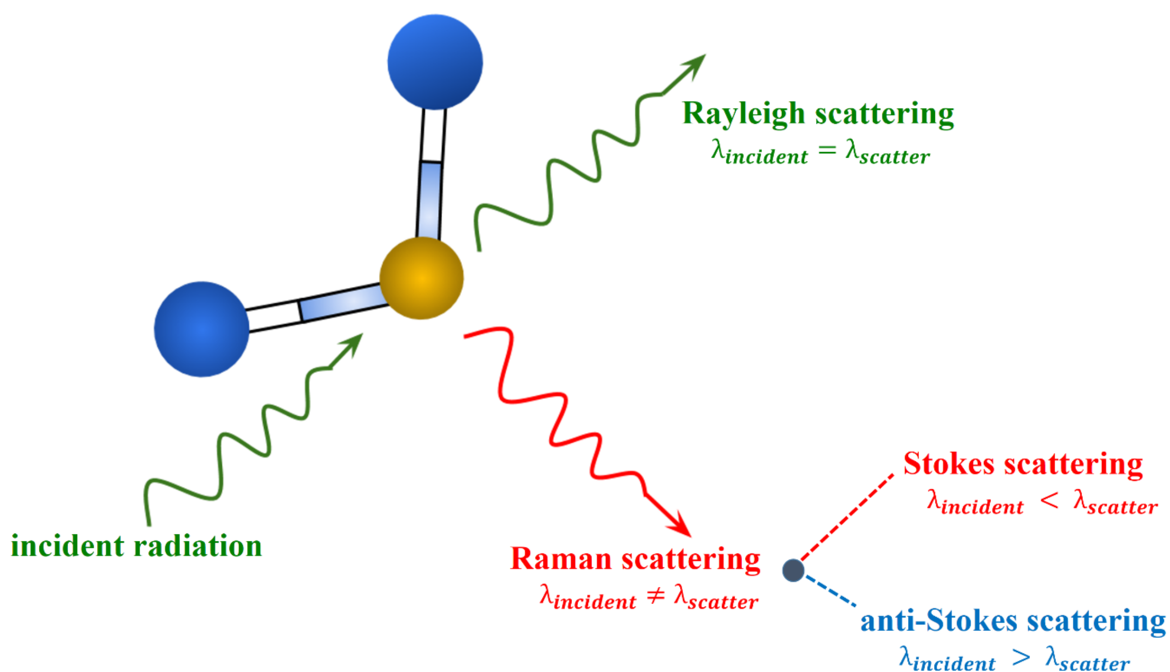

Figure 3.6 The fundamental interaction of light with a molecule in Raman scattering

A Raman spectrum comprises of a number of peaks, showing the frequency and intensity of the Raman scattered light, each of which, corresponds to a specific molecular bond vibration, individual bonds, groups of bonds, lattice modes, etc.

There are two fundamental types of Raman scattering processes. When the frequency of scattered radiation is decreased compared to the exciting radiation, the process is called Stokes scattering in which molecule or atom absorbs energy. If the scattered radiation has a larger frequency compared to the exciting radiation, the process is called anti-Stokes scattering, in which molecule or atom loses the energy.

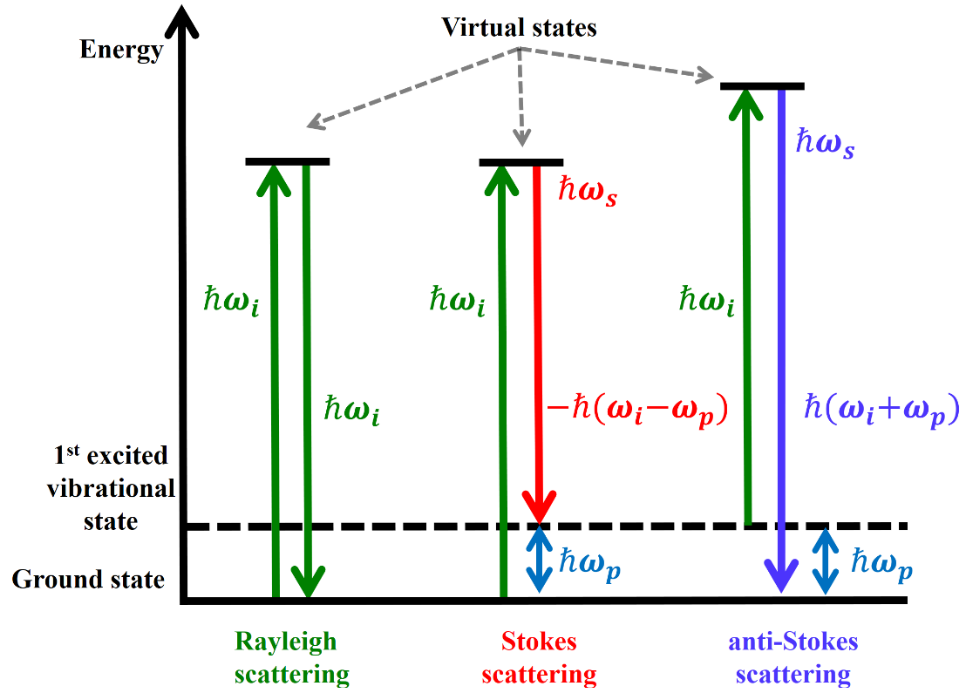

Figure 3.7 Jablonski diagram for Rayleigh and Raman scattering processes

Raman effect happens based on the following series of events. The material gets excited to a virtual state by absorbing an incoming photon of frequency "ω" and wave vector "k". An elementary excitation of frequency ω_p and wave vector q is generated (Stokes process) or annihilated (anti-Stokes process). In case of solids these excitations can be magnons, plasmons or phonons. A scattered photon of frequency ω_s and wave vector k_s is generated by a recombination. The processes of Rayleigh, Stokes, and anti-Stokes scattering are described in fig 3.7.

(i) Experimental setup

The schematic of the experimental setup used to measure Raman spectra of the InN films in the present study is shown in the Figure 3.8. Since a Raman signal is generally very weak (only ~10^{-8} of the total scattered photons are Raman scattered), a laser is used as the excitation source. The choice of laser wavelength depends entirely on the application.

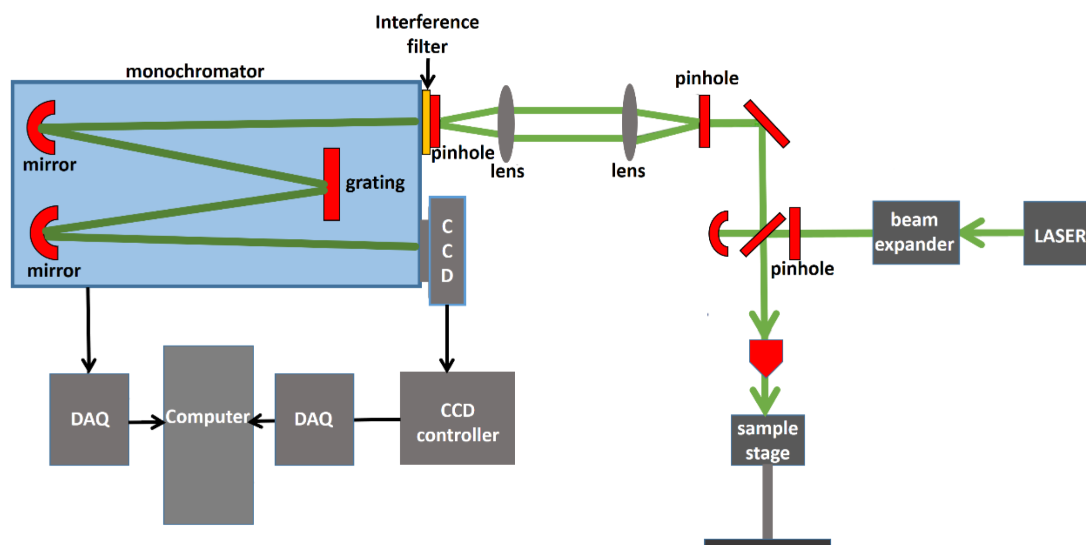

Figure 3.8 Schematic of Raman scattering measurement system used in this work

The laser light is focused onto the sample through a beam-splitter and confocal optics, and the scattered light from the sample is also collected by confocal lens and beam-splitter. This beam is focused onto a mirror. The reflected light from the mirror is focused onto the McPherson double subtractive monochromator. An interference or Rayleigh rejection filter is used to filter only the Raman scattering light. A high resolution spectrum is generated by a grating 1800 lines/mm. The signal from the grating is collected by the liquid nitrogen cooled charged coupled device (CCD). The CCD measures the light intensity from each wavelength section. Data collection and system control is performed by the0LabVIEW-based software run on personal computer.

(ii) Kinematical limitations for Raman scattering

Considering only the first-order Raman scattering, the conservation of energy and momentum equations are,

$$\hbar\omega_s = \hbar\omega_i \pm \hbar\omega_p \quad (3.2)$$

$$k_s = k_i \pm q \quad (3.3)$$

where, '+' is the case of anti-Stokes and '-' for the case of Stokes scattering. Also the incident wave vector is $k_i = \omega_i n(\omega_i)/c$ and the scattered wave vector is given by $k_i = \omega_s n(\omega_s)/c$; *n* is the refractive index, and *c* is the speed of light in vacuum.

Let us consider an ideal crystal with translational symmetry. Momentum conservation holds only for those samples with large scattering. Light scattering experiments are generally performed with visible light (i.e. $\omega/2\pi \sim 10^{14}$-10^{15} Hz). The frequency of exciting radiation is of the order of $\omega/2\pi \sim 3\times10^{11}$-$10^{14}$ Hz (10 - 3000 cm^{-1}) which corresponds to far- to near-infrared spectral range [113]. Since the energy transfer is smaller compare to the energy of the photons in the incident radiation this implies that $\omega_p = \omega_i$ and $|k_i| \approx |k_s|$. Using these approximations the wave vector can be written as $|q| \approx 2\,|ki|sin(\theta/2)$; θ is the angle between the incident and scattered radiation. The maximum value excitation wave vector is $|q_{max}| \approx 2\,|ki| \approx \omega_i n(\omega_i)/c$ and follows the condition $|q_{max}| < 3 \times 10^{-3} A^{o^{-1}}$ for typical Raman scattering experiments. This is small compared to the size of the Brillouin zone boundary $|q_{max}| \approx \frac{2\pi}{a} \approx 1\text{Å}^{-1}$; a is the lattice constant of the crystal [114]. This concludes that the Raman scattering experiments can probe only those excitations that are very close to the Brillouin zone center ($|q_{max}| \approx 0$).

(iii) Raman and IR Allowed Phonons for Hexagonal Structure

The space group for the hexagonal structure is C_{6v}^4. The C_{6v}^4 includes the translations, reflections and rotation operations. To find the symmetry of IR and Raman active phonon modes, the irreducible representations of a vector in the structure must be identified. When the space group

is known, the corresponding character table can be found in the literature. A character table consists of a complete set of possible symmetry operations for a point group. The character table for C_{6v}^4 point group symmetry [115] derived from group theory is shown in Table 3.3.

Table 3.3 Character table and the symmetry operation for C_{6v} point group symmetry

C_{6v}		E	$2C_6(z)$	$2C_3(z)$	$C_2(z)$	$3\sigma_v$	$3\sigma_d$	linear functions	quadratic functions	cubic functions
A_1	Γ_1	+1	+1	+1	+1	+1	+1	z	x^2+y^2, z^2	z^3, $(x^2+y^2)z$
A_2	Γ_2	+1	+1	+1	+1	-1	+1	R_z	---	---
B_1	Γ_3	+1	-1	+1	-1	+1	-1	---	---	$x(x^2 - 3y^2)$
B_2	Γ_4	+1	-1	+1	-1	-1	-1	---	---	$y(3x^2 - y^2)$
E_1	Γ_5	+2	+1	-1	-2	0	0	(x, y) (R_x, R_z)	(xy, yz)	(xz^2, yz^2), $(x(x^2+y^2)$, $y(x^2+y^2))$
E_2	Γ_6	+2	-1	-1	+2	0	0	---	$(x^2 - y^2$, xy)	$(xyz,\ z(x^2-y^2))$

C_{6v}^4 in the character table 3.3, is Schoenflies symbol is for the point group. The first column shows Mulliken symbols given by the irreducible representations. Ai denotes the symmetry with respect to rotation of the principle axis. Bi denotes the antisymmetric with respect to rotation around principle axis, and Ei shows that representation is doubly degenerated. E denotes the

identity operation. Cn denotes n-fold rotation i.e. rotation by 2π/n about an axis of symmetry. Wurtzite structure has two six-fold (2C6) symmetry axes that are parallel to the [0001] direction i.e. 2π/6 rotation and10π/6 rotation, two threefold (3C3) rotations about the [0001] direction i.e. 2π/3 and 4π/3, one two-fold (C2) rotation around the [0001] direction by π, there are six mirror planes three ($3\sigma\ v$) of them are passing opposite vertices of the hexagon making π/3 each other and three ($3\sigma\ d$) are passing through faces of hexagon making π/3 each other [116]'[117].

The x, y and z are the Cartesian coordinates and the rotation about these axes are Rx, Ry, and Rz.. The p_x, p_y, and p_z orbitals have the same symmetry as x, y, and z. The dipole moments along these axes is $\mu_x = -ex$, $\mu_y = -ey$ and $\mu_z = -ez$.

The dipole selections for IR spectroscopy is $(\partial\mu/\partial Q)_0 \neq 0$, this implies that any vibration must change the dipole moment of the molecule for a phonon to be IR active. Since x, y, z and the atomic displacements and behave likewise, the IR active modes transform as x, y or z. Following the Table 3.3, A_1 and E_1 are IR active phonon modes.

The orbitals *p* and *d* orbitals (d_{xy}, d_{xz}, d_{yz}, $d_{x^2-y^2}$, and d_{z^2}) correspond to the terms xy, xz, yz, x^2-y^2 and z^2. A complex polarizability tensor (also termed as the susceptibility) must alter for a phonon mode to be a Raman active. As the polarizability operator obeys the identical symmetry for binary and quadratic functions of x, y, and z, the phonon modes transform these functions, and hence are Raman active phonon modes. According to the Table 3.3, A_1, E_1, and E_2 are the Raman active phonon modes [118]. Table 3.4 summarizes the number of the different long-wavelength phonon modes with N atoms unit cell.

Table 3.4 The phonon modes associated with a unit cell with N basis atoms

Phonon	**Number of modes**
Longitudinal acoustic	1
Transverse acoustic	2
Longitudinal optical	N – 1
Transverse optical	2N – 2
Total # of optical modes	2N – 3

The irreducible representation of phonon modes for the wurtzite structure can be found by constructing a table for reducible representation of symmetry operations in wurtzite structure and reconstructing the irreducible representations of phonons afterwards. The phonon modes at the Brillouin zone center are,

$$\Gamma_{irreducible} = \Gamma_{Acoustic} + \Gamma_{Optical} = 2A_1 + 2B_1 + 2E_1 + 2E_2 \qquad (3.4)$$

The table 3.3 implies that the B_1 phonon mode is not Raman or IR active. Hence, for the optical phonon modes that are Raman-active,

$$\Gamma_{Optical} = A_1 + E_1 + 2E_2 \qquad (3.5)$$

A_1 and E_1 are the polar phonons that split into longitudinal acoustic and longitudinal optical (LA, LO), as well as into transverse acoustic and transverse optical (TA, TO). The optical branches of A_1 and E_1 are both Raman and IR active. The non-polar B_1 and E_2 phonons are labelled as high or low according to their frequencies. The optical phonon modes for wurtzite structure are illustrated in Fig. 3.9.

The Raman scattering measurements used in the present work (schematically shown in Figure 3.8) are done in backscattering geometry. The phonon modes that can be observed in z(x,

x)$\bar{z}$ backscattering geometry are A_1-LO and E_2 phonon modes. The symbols, outside the bracket left to right indicate the direction of the incident and scattered light, respectively. The symbols in the z(x, x)$\bar{z}$, left to right show the direction of the incident and scattered polarization, respectively. The *z*- direction is along the *c*-axis and *x*- and *y*- directions are perpendicular to the *c*-axis.

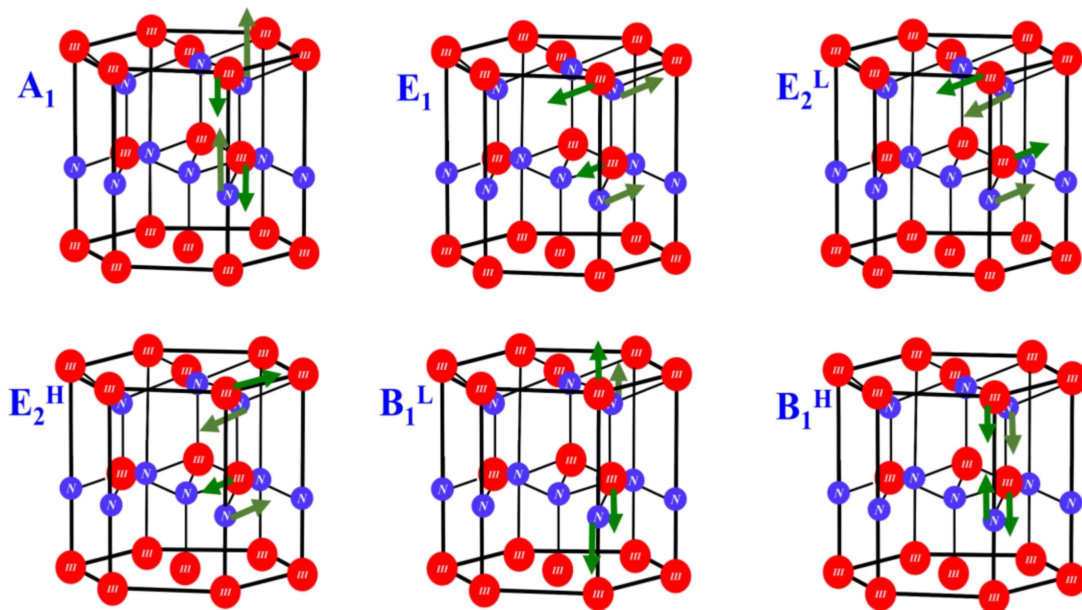

Figure 3.9 Optical phonon modes of wurtzite structure

3.9 X-ray diffraction (XRD)

X-ray diffraction or simply XRD is a versatile tool for the structural analysis of materials. Monochromatic X-rays are generally chosen for material analysis. When the x-rays are directed on a crystal, ray reflection of different atomic planes result in diffraction pattern with angular resolution of interference fringes originating from lattice planes with different spacing. Constructive interference occurs when the path difference is equal to an integral multiple of the

wavelength. The path difference between interfering waves can be expressed as a function of the lattice spacing and the angle of incidence[119]. The relation between the lattice spacing d and incidence angle θ (Bragg's law) can be written as:

$$n\lambda = 2d_{hkl}sin\theta \quad (3.6)$$

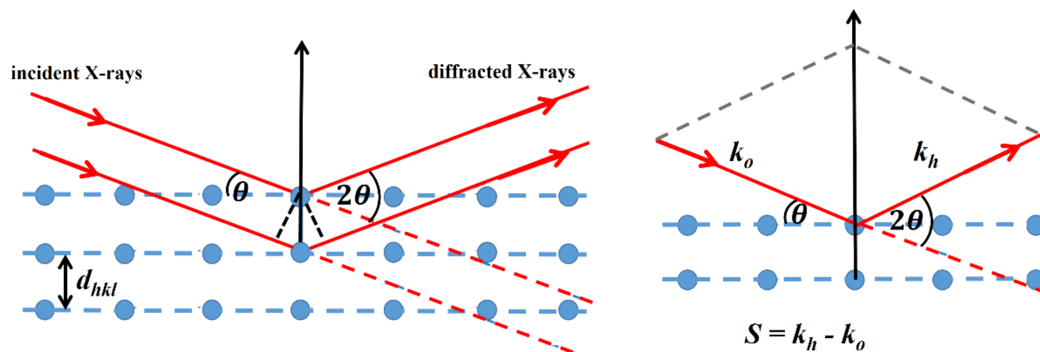

Figure 3.10 Schematic representation of x-ray diffraction; Bragg's diffraction (left) and relationship of the incident, diffracted, and scattering vectors with respect to the crystal

Here n is the order of diffraction, λ is the X-Ray wavelength, θ is the angle of incidence and d_{hkl} inter-planner spacing in the lattice. Conditions for constructive interference is illustrated in the Figure 3.10 [120].

The angle 2θ between the incident X-ray and the detector, is measured experimentally. The crystal acts as a 3-dimensional diffraction grating. If the sample, or detector, or both move, a collection of diffraction maxima can be obtained. Each collection of crystalline planes produces a diffraction spot. The shape and location of these diffraction spots are correlated with the crystalline

inter-planner spacing and crystallite sizes. The diffraction spots and crystalline planes in reciprocal space form a 3D reciprocal lattice [120].

The direction of the S vector depends on the angle ω as shown in Fig. 3.10. The reciprocal lattice can be investigated using the scattering vector and the magnitude of the S vector dependence on the angle 2θ [120]. Reciprocal space can be found by rotating the detector and the sample in an X-ray diffractometer.

The lattice parameter c may be determined for a hexagonal crystal system by measuring the two high angle symmetric reflections (d_{0006} and d_{0004}) and using the Eq. 3.7[120].

$$\frac{1}{d_{hkl}^2} = \frac{4}{3}\frac{h^2 + k^2 + hk}{a^2} + \frac{l^2}{c^2} \qquad (3.7)$$

From high-angle asymmetric reflections measurements (usually, $d_{10\text{-}15}$, $d_{20\text{-}25}$, or $d_{20\text{-}24}$) and the previously calculated lattice parameter value “c”, the lattice parameter “a” can be determined.

A diffractometer used in our work has a sample stage allowing only in-plane rotation. Both source and detectors can rotate around the sample stage allowing independent control of Theta and Omega angles.

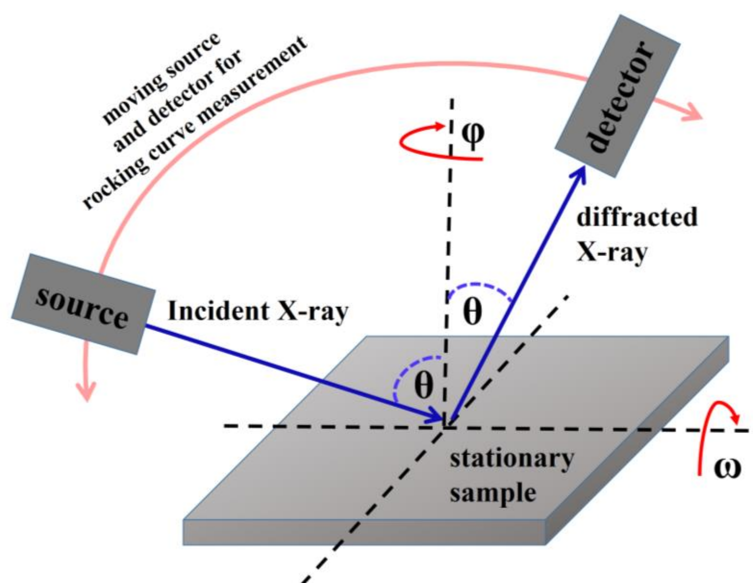

Figure 3.11 The example geometry for the X-ray diffractometer and sample reference frame with axes of rotation. The φ axis is normal to sample while ω is in plane with the sample

In order to record the diffractogram, the sample was placed on the sample stage. Initial coarse Theta-2Theta scan was performed. With the detector positioned at the InN (0002) peak (or sapphire (0006) peak) the sample was rotated in plane to optimize PHI. Then the Theta-2Theta scan data was collected in the range of interest. The angle of incidence was set to be relatively shallow (~18°) allowing XRD spectrum to be recorded using the available sample holder. Shallower angle resulted in stronger detected signal, given the typical studied film thicknesses ranging from 2 nm to 500 nm.

I am thankful to Dr. Daniel Deocampo at Georgia State University for sharing his XRD facility that was used to measure samples in the present study.

3.10 FTIR

In the present study the FTIR reflection spectroscopy was to used to measure film thickness. Schematic of FTIR spectrometer based on Michelson interferometer used in this work is shown in Fig. 3.11. The light coming from the source is split into two parts by the beam splitter. One beam can be partially reflected onto the fixed mirror and the other beam can be transmitted to the movable mirror, which moves a very short distance away from the beam splitter. The two partial beams that are reflected off from the mirrors, interfere at the beam splitter. The waves acquire phase difference with respect to each other for different positions of the moving mirror. The output of the detector is a function of the position of the mirror x/2. The optical path difference between the two beams is x.

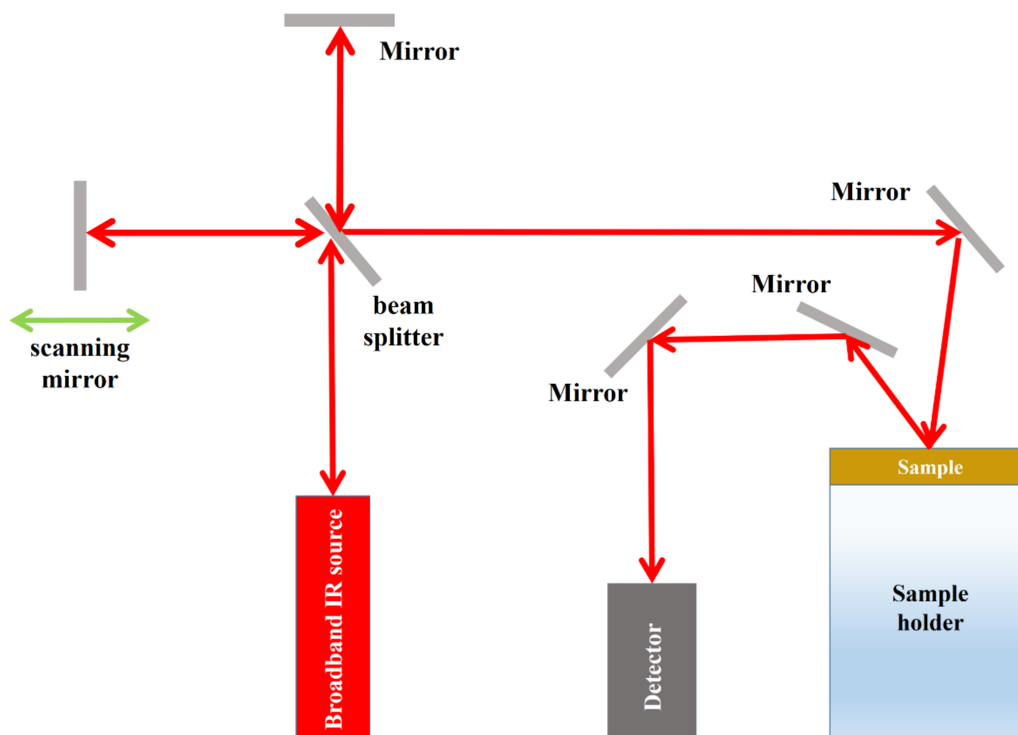

Figure 3.12 Schematic of FTIR measurement system

The result of this path difference is an interference pattern *I(x)*. This is then Fourier Transformed to obtain the spectrum by the computer. The spectrum S is given by

$$S(v) = \int_{-\infty}^{+\infty} I(x)e^{2\pi ivx}dx = F^{-1}[I(x)] \qquad (3.8)$$

$$I(x) = \int_{-\infty}^{+\infty} S(v)e^{-2\pi ivx}dv = F[S(v)] \qquad (3.9)$$

The integral in Eq. 3.8 is the inverse Fourier Transform while the one given by Eq. 3.9 is the Fourier Transform. FTIR spectrometers usually use the Globar source as the IR source for MIR region. For the far IR and near-IR region mercury discharge lamp and tungsten-halogen lamp are used, respectively.

3.11 Atomic force microscopy (AFM)

Atomic force microscopy is a technique that uses the measurement of forces between a sharp tip and the sample surface to construct the material surface topography at nanoscale. Figure 3.1 illustrates basic components of a typical AFM system. The sharp tip is mounted on the cantilever. The deflection of the light beam reflected of the cantilever is measured to calculate the cantilever deflection, which is then converted into the tip-material interaction force. The change in force is recorded as a function of the tip position on the surface and a topography map of the surface is generated. There are three critical components that must be controlled to achieve high resolution. A cantilever with a sharp tip. The stiffness of cantilever must be less than the effective spring constant that is keeping atoms together. The tip are made with curvature radius as small as possible (typically it ranges within 20 – 50 nm). A piezo-electric tube scanner is used to control the movement of the sample in the x, y, and z-directions.

AFM can operate in two basic modes. Constant force mode is performed with the feedback control mode. In this mode, moving the sample up and down, the piezo will adjust the tip-separation to maintain a constant force and deflection mode, without the feedback control mode, this mode is useful for imaging very flat samples at high resolution.

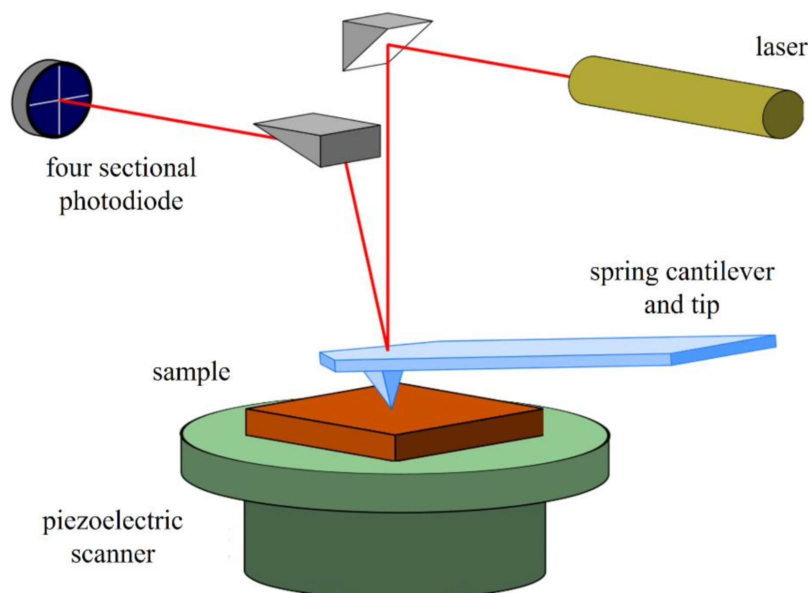

Figure 3.13 A schematic of a typical AFM [153]

In this work AFM in tapping mode was used to measure the surface morphology of all samples. In tapping mode, the cantilever is set to oscillate at its resonant frequency. A constant oscillation amplitude is retained with constant frequency and amplitude of the driving signal while scanning the sample. The cantilever oscillation is done with the help of a piezo element in its holder. The oscillation amplitude varies from a few nm to 200 nm. The cantilever oscillation amplitude is used as a feedback parameter. The distance between the cantilever tip and the sample surface is kept constant as the tip scans over the surface. Vertical cantilever motion that keeps this distance constant is recorded as the surface topology profile. [121].

4 INFLUENCE OF PLASMA ACTIVATED NITROGEN ON INDIUM NITRIDE GROWTH

4.1 Introduction

Plasma is a quasineutral medium in which there are approximately equal numbers of positively and negatively charged particles (mainly ions and electrons). In the laboratory, plasma may be produced by heating a gas to extremely high temperatures, or by the application of DC or low frequency RF (<100 kHz) or high frequency RF(~13.56 MHz) electric fields, to the gap between two metal electrodes, the latter being called capacitively coupled plasma (CCP). In this work the plasma used for InN PA-MOCVD, CCP technique has been used.

Upon excitation the plasma constituents will lose their energy fairly quickly. Out of all the possible mechanisms through which this energy can be lost, the most important one is by releasing a photon to carry the energy away. And this gives rise to the typical plasma glow. In optical atomic spectroscopy, the wavelength of the emitted photon can be used to determine the identity of the different plasma species and the number of photons is directly proportional to the concentration of that specie in the plasma. The methods of atomic emission spectroscopy, when applied to such a emission spectrum, yield the energy and concentrations of various plasma species.

In the present study the nitrogen plasma has been used as a nitrogen precursor for plasma-assisted MOCVD growth of InN. In principle the atomic nitrogen ions from the plasma chemically combine with the indium atoms to form InN at the substrate. Atomic nitrogen ions in this work were generated directly from N_2 by ionizing it in CCP source. This approach has not been used in CVD, but PAMBE is well known.

The understanding of various growth parameters in the plasma composition and ion energies is vital to achieve high quality growth of InN. Properties of plasma can be measured by atomic emission spectroscopy.

In this chapter, the methods of atomic spectroscopy are discussed to analyze the nitrogen plasma composition and the composition of plasma affects the InN growth process and its structural properties. The change in energy and concentration of various plasma species (neutral and ionized, atomic and molecular) were extracted from the in-situ optical emission spectra (example spectrum is shown in Fig. 4.1) measured at the growth surface. The plasma emission spectra were analyzed using atomic emission spectroscopy[122]. A strong correlation has been found between the growth rate of InN films and atomic nitrogen ion (N^{+}, N^{+2}, N^{+3}) flux.

Numerous investigations of the RF-nitrogen plasma have been previously done by optical emission spectroscopy[123],[124, 125] and quadrupole mass spectrometry[123, 126, 127]. These investigations indicated that the outputs of the RF-sources contain atomic nitrogen, metastable molecular nitrogen, and molecular nitrogen ions. The molecular nitrogen ions have been proposed as the responsible species for the growth of GaN under the metastable growth conditions used in PA-MBE[128]. In this chapter I describe experiments that demonstrate that the atomic nitrogen ions have a dominant effect on the PA-MOCVD growth of InN films and their structural properties.

4.2 Sample growth

Three sample sets of InN were grown at different reactor pressures. The RF power was varied within each set. Power dependence on the pressure info. (theory). The power range for sample sets A (2.2 Torr, V/III=57), B(3.8 Torr, V/III=805) and C (4.2 Torr, V/III=822) was 100W – 300W, 300W – 425W and 350W – 550W respectively. Nitrogen flow through the plasma source was kept the same within each set. Table 4.1 summarizes the growth conditions used for each sample set.

Table 4.1 Growth conditions for three sets used in this study of InN growth

Set	V/III molar ratio	Growth pressure(Torr)	Growth Temperature(°C)	RF power (W)
A	57	2.2 ± 0.24	775	100 - 300
B	805	3.7 ± 0.26	775	300 - 425
C	822	4.2 ± 0.26	775	350 - 500

The substrate preparation steps for three sets were kept same and are as follows. Sapphire substrates were heated to 250°C. At 250°C the substrates were exposed to 100sccm of H2 gas at 201Torr for 5 minutes. After that, the substrates were further heated to 500°C in nitrogen gas keeping the pressure at 2.1Torr. The InN nucleation layer was deposited at 500°C, 2.1Torr, 150W RF power, 750sccm N_2 plasma and 250sccm Trimethylindium for 5 minutes. The samples were further heated to 775°C. And then films were at the conditions mentioned in the Table 4.1.

For all the samples, the plasma spectra were recorded during growth above the growth surface. The grown samples were characterized by FTIR, Raman and XRD. Results of these measurements are provided in sections 4.5 of this chapter.

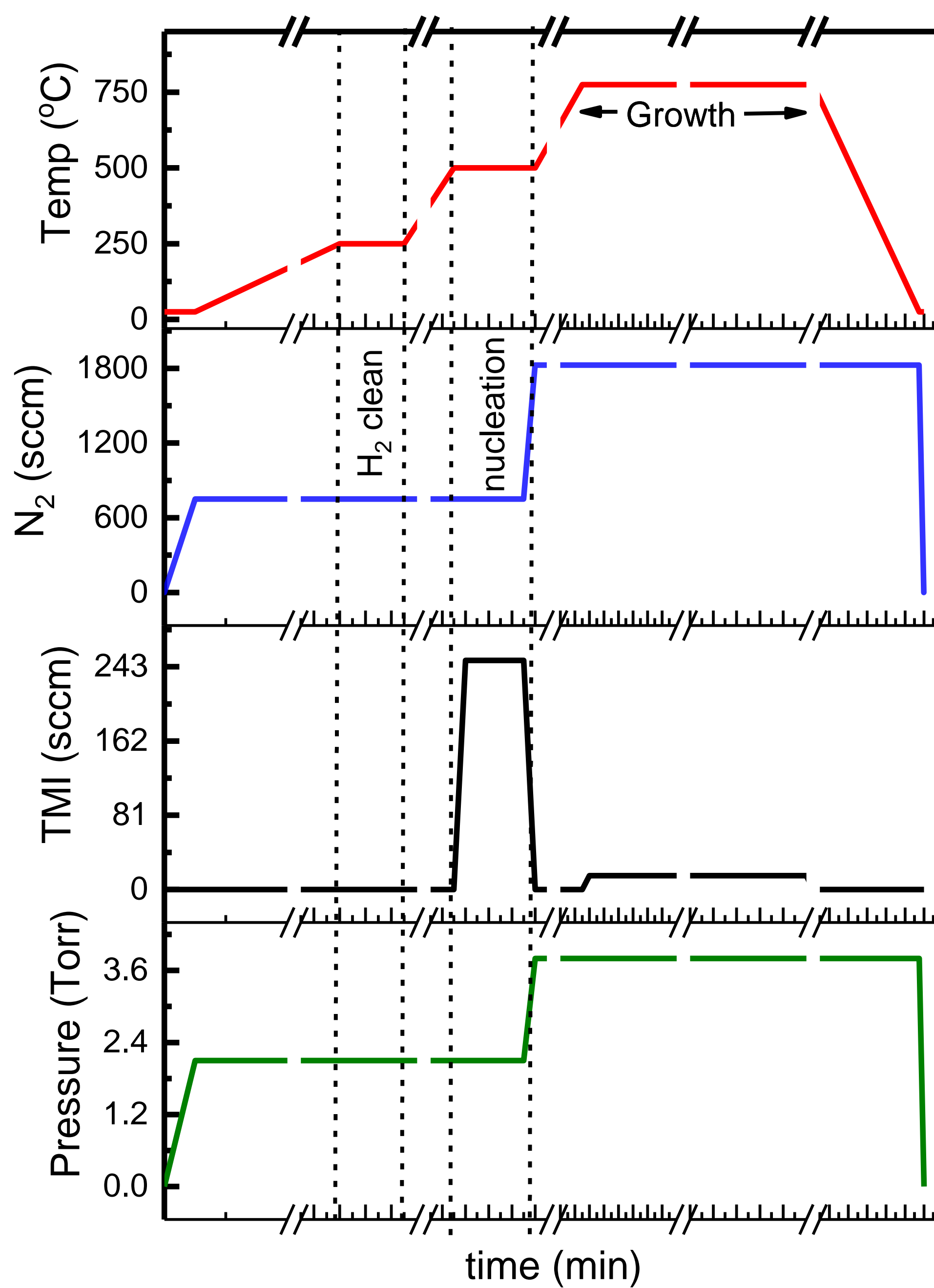

Figure 4.1 Growth conditions for sample set B

4.3 Plasma emission spectroscopy measurements

The glow of nitrogen plasma and corresponding emission spectrum is shown in Fig. 4.1. The emission spectrum of nitrogen is dominated by the molecular transitions (mainly rotational and vibrational) in the spectral range 250nm to 700nm. The rest of the spectrum from 700nm to 11nm is mainly due to the transitions in the atomic nitrogen ions. In the present study the transition's belonging to N+ ions are used to characterize the plasma composition. Most of these emission lines lie in the range 700nm to 900nm. The spectral region used for analysis is showing the dotted line box in Fig. 4.2.

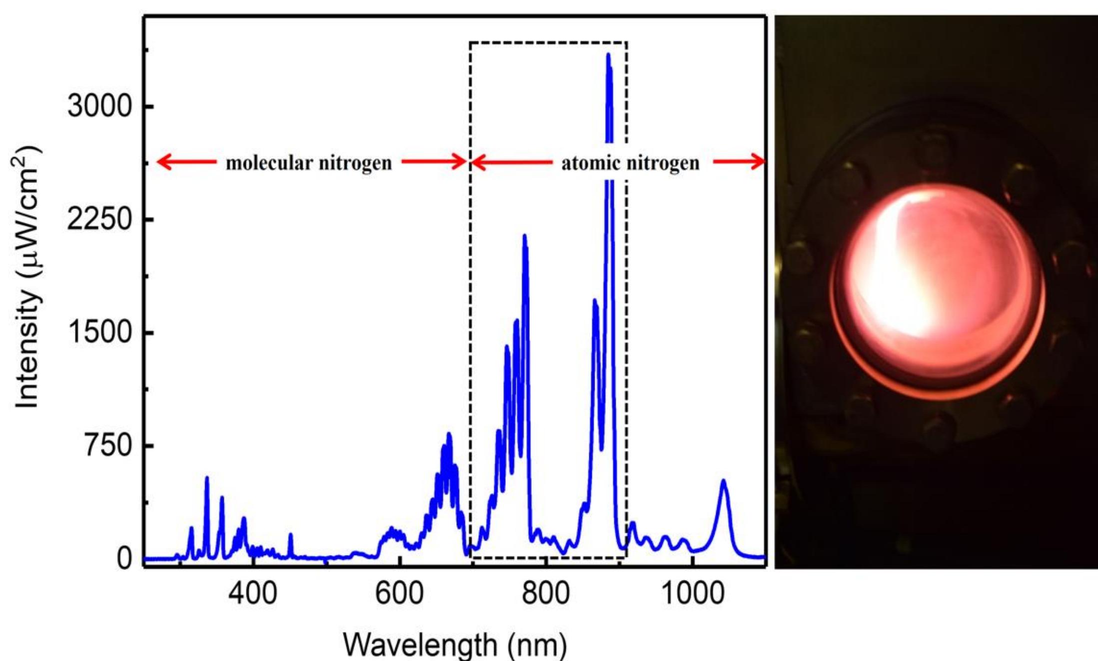

Figure 4.2 (Left) The optical emission spectrum of nitrogen plasma at RF power ~ 300W and 2..2 Torr reactor pressure. The boxed section represents the the spectral range used to analyze the plasma composition in the present study. (Right) Nitrogen plasma glow

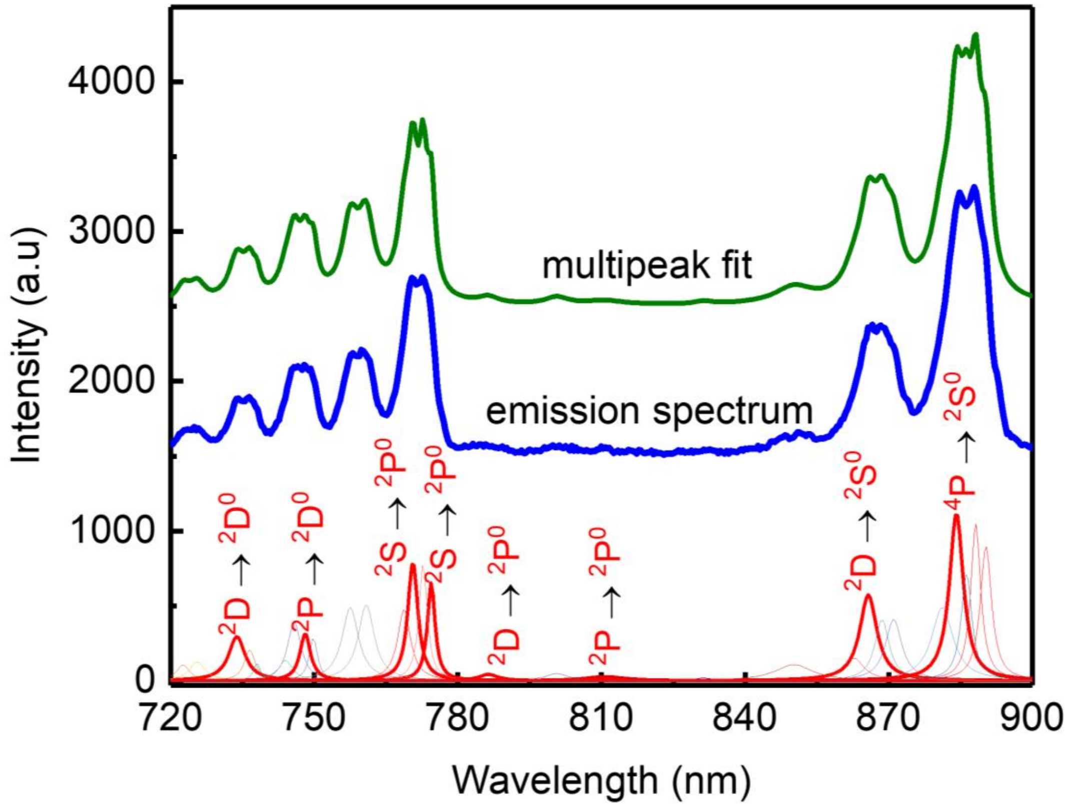

Figure 4.3 Nitrogen emission spectrum (solid line) and its multi-peak fit (dashed line) measured above the sample surface. N+ spectral transitions are labelled

4.1.1 Plasma composition analysis

Plasma emission spectrum can be analyzed not only to identify the gas by its spectral lines, but also to extract its quantitative composition. The ratio of the number densities of the neutral and ionized species is described by the Saha–Boltzmann equation (4.1).

$$\frac{N_e n(X_{i+1})}{n(X_i)} = \frac{2Q_{i+1}}{Q_i} \left(\frac{2\pi m k_B T_e}{h^2}\right)^{\frac{3}{2}} \exp\left(-\frac{\chi_i}{k_B T_e}\right) \qquad (4.1)$$

where N_e is the electron number density, $n(X_i)$ is the concentration of the atoms in the ionization state *i*, Q_i is the partition function that includes both the degeneracy and probability of the atomic states[129, 130], χ_i is the ionization energy of the neutral atom, *m* is the electron mass, T_e is the electron temperature.

T_e was determined from the plasma emission spectra measured above the sample surface during growth (typical spectrum is shown in Fig.1a). Boltzmann equation (4.2) relates spectral line intensities to the electron temperature T_e.

$$\ln(\frac{I_{mn}\lambda_{mn}}{hcA_{mn}g_m}) = -\frac{E_m}{k_B T_e} + \ln(\frac{N}{U(T_e)}) \qquad (4.2)$$

I_{mn} is the intensity and λ_{mn} is the wavelength of the spectral line corresponding to the $m \rightarrow n$ state transition, $g_m = 2J_m + 1$ is the statistical weight, A_{mn} is the Einstein transition probability of spontaneous emission, E_m/k_B is the normalized energy of the upper electronic level. λ_{mn}, g_m, A_{mn} and E_m values for selected N^+ spectral atomic lines were obtained from the NIST Atomic Spectra Database[131], and are shown in Table 4.2. All the emission spectra were fitted by a superposition of Gaussian profiles to determine their position, relative intensity, and full width at half maximum. The results of the fitting are shown in Tables 4.3 nd 4.4. The obtained results of intensity were plugged into Eq. 4.2 and plotted as $\ln(\frac{I_{mn}\lambda_{mn}}{hcA_{mn}g_m})$ versus E it should result in a linear plot as seen in Eq.4.2. Boltzmann plot[132] for the spectrum in Fig. 4.2 is shown in Fig. 4.3. Electron temperatures T_e were extracted from the linear fit of the Boltzmann plot for each spectrum. Numerically, the electron temperature is given by

$$K_B T_e = -\frac{1}{slope\ of\ Boltzmann\ plot}$$

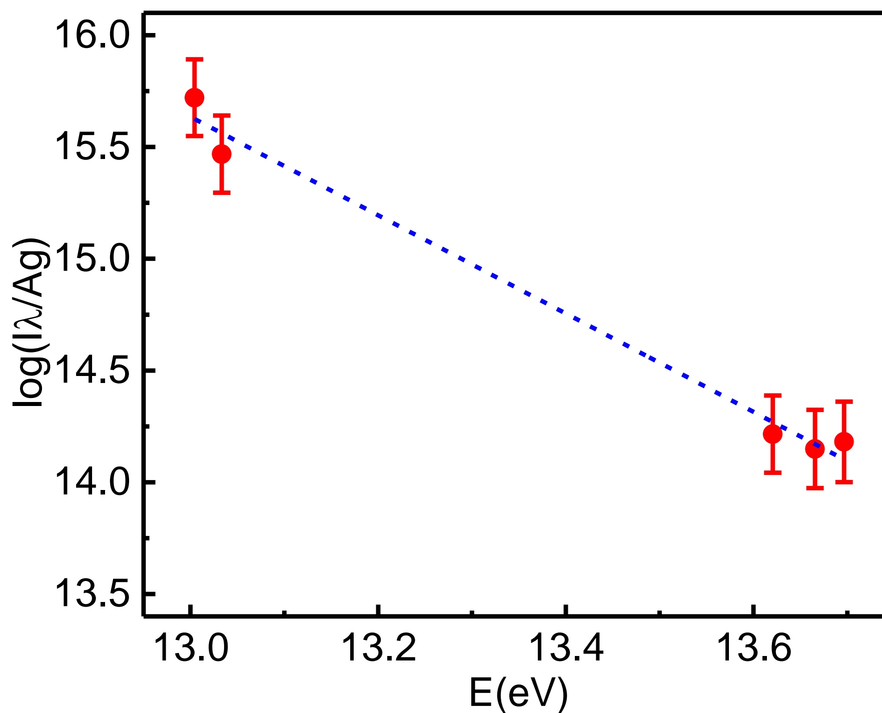

Figure 4.4 Boltzmann plot for the N+ spectral lines (dots) and its linear fit (dashed line)

Table 4.2 Boltzmann plot for the N+ spectral lines (dots) and its linear fit (dashed line)

λ(nm)	**A_{ij} (s^{-1})**	**g_i**	**E_i (cm^{-1})**
734.76	555000	6	110470.244
748.52	7970000	4	110220.107
762.82	690000	4	109856.520
866.44	163000	4	105119.880
884.36	75000	2	104886.10

Table 4.3 Fitting parameters for the plasma emission spectra from sample set A

Sample #	**→**	**1410**	**1413**	**1411**	**1412**
Wavelength	**E**	**Intensity**	**Intensity**	**Intensity**	**Intensity**
734.76	13.69	139.125	681.21	440.169	594.731
748.52	13.66	135.78	432.90	327.359	405.644
762.82	13.62	180.78	700.12	489.158	649.298
866.44	13.03	404.90	1345.65	991.33	1227.58
884.36	13.00	713.21	2345.98	1661.18	2108.73

Table 4.4 Fitting parameters for plasma emission spectra from sample set B

Sample #	**→**	**1348**	**1345**	**1346**	**1344**
Wavelength	**E**	**Intensity**	**Intensity**	**Intensity**	**Intensity**
734.76	13.69	136.71	289.33	455.86	333.81
748.52	13.66	112.94	315.42	543.23	399.12
762.82	13.62	118.13	365.24	849.92	657.36
866.44	13.03	281.72	525.11	689.24	620.43
884.36	13.00	177.21	200.97	516.70	513.85

Neutral nitrogen species concentration $n(X_0)$ was determined using the one-line calibration-free method utilizing equation 4.3 for an optically thin line (884nm)[133-135].

$$Fn(X_0) = \frac{I_{mn}Q_0(T)}{A_{mn}g_m} \exp(-\frac{E_m}{k_B T_e}) \qquad (4.3)$$

The normalization factor F was determined by normalizing the ionized nitrogen concentrations obtained from equation (4.3) and $n(X_0)$.

The electron density N_e in equation (4.1) was calculated from the linewidth of a Stark broadened line [1043nm] using equation 4.4.[136]

$$N_e = \frac{\Delta\lambda_{FWHM} \times 10^{16}}{2\omega_s} \qquad (4.4)$$

where $\omega_s = 4.1 \times 10^{-3}$ nm is the Stark-broadening parameter [45].

The state of local thermal equilibrium (LTE)[126] was verified to be fulfilled for each spectrum using the Mc Whirter criterion[137]. The lower limit of the electron density under this condition can be determined from this relation.

$$N_e \geq 1.6 \times 10^{12} \sqrt{(\Delta E)^6 T_{e(eV)}} \sim 10^{18} \gg \sim 10^{13} \qquad (4.5)$$

The electron number density for all the analyzed spectra remained $\sim 10^{18}$ While the electron temperature stayed in the range of 3000K to 7000K. Hence, the LTE condition was well verified for all the spectra used in this study.

4.4 Results and discussion

4.4.1FTIR measurements

The growth rate was determined by fitting interference fringes measured by Fourier transform infrared (FTIR) spectroscopy. The fitted FTIR spectra for three sample sets are shown in the Figures 4.5, 4.6 and 4.7. Table for all samples with growth time, film thicknesses, and growth rates.

Results of the plasma analysis for each of the grown samples are summarized in Fig.2. The variation in the density of atomic nitrogen ions is found to be in a good correlation with the change in growth rate for the three sets of samples used in this study. However, no correlation is found between the variation in atomic neutrals or molecular plasma species and the growth rate.

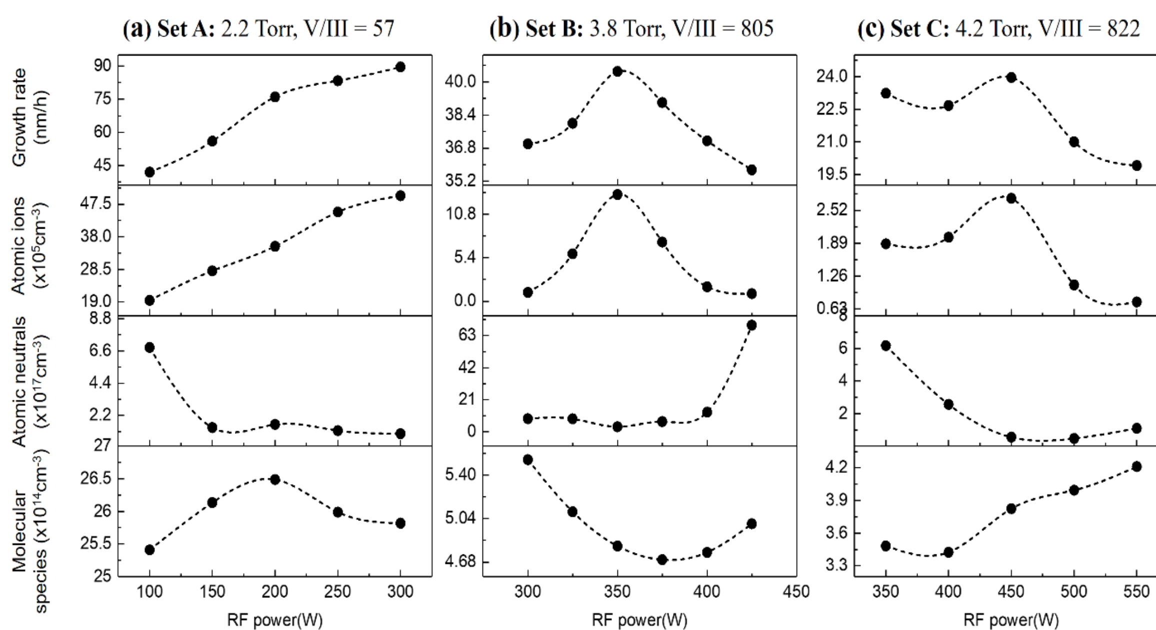

Figure 4.5 InN growth rate and nitrogen plasma species concentrations dependence on plasma power level for sample sets A (a), B (b), and C (c)

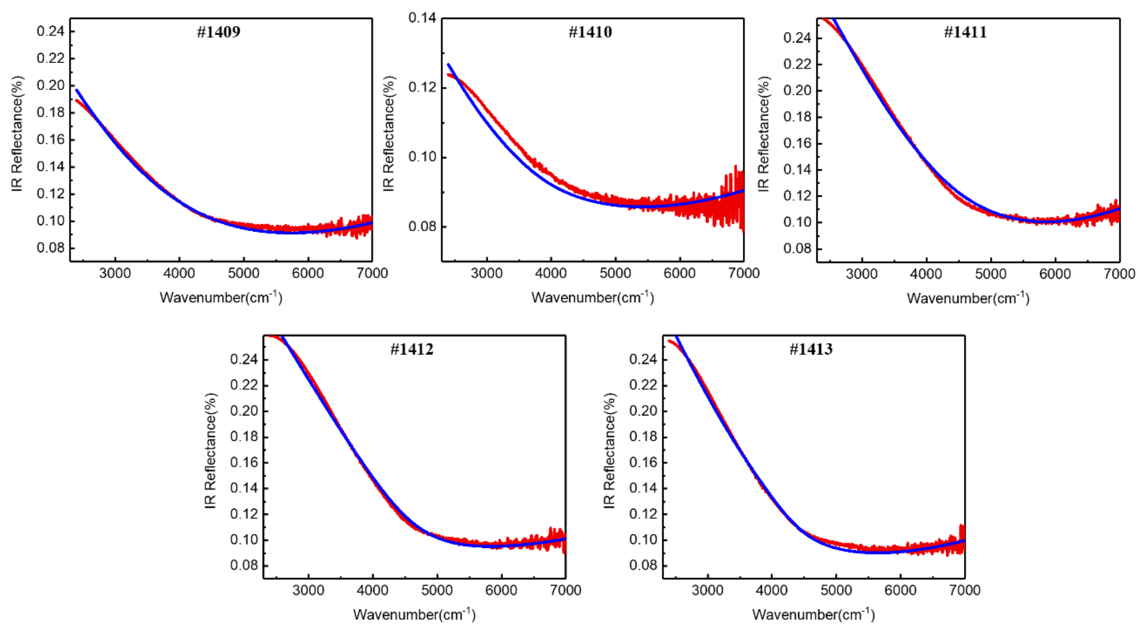

Figure 4.6 FTIR spectra fitting for sample set A

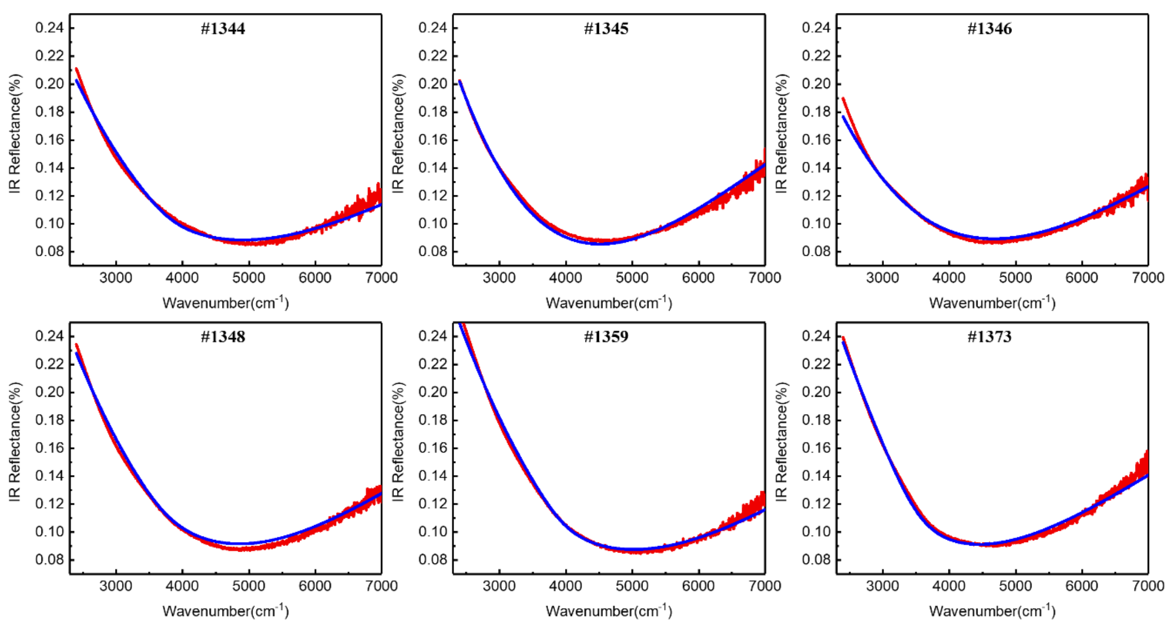

Figure 4.7 FTIR spectra fitting for sample set B

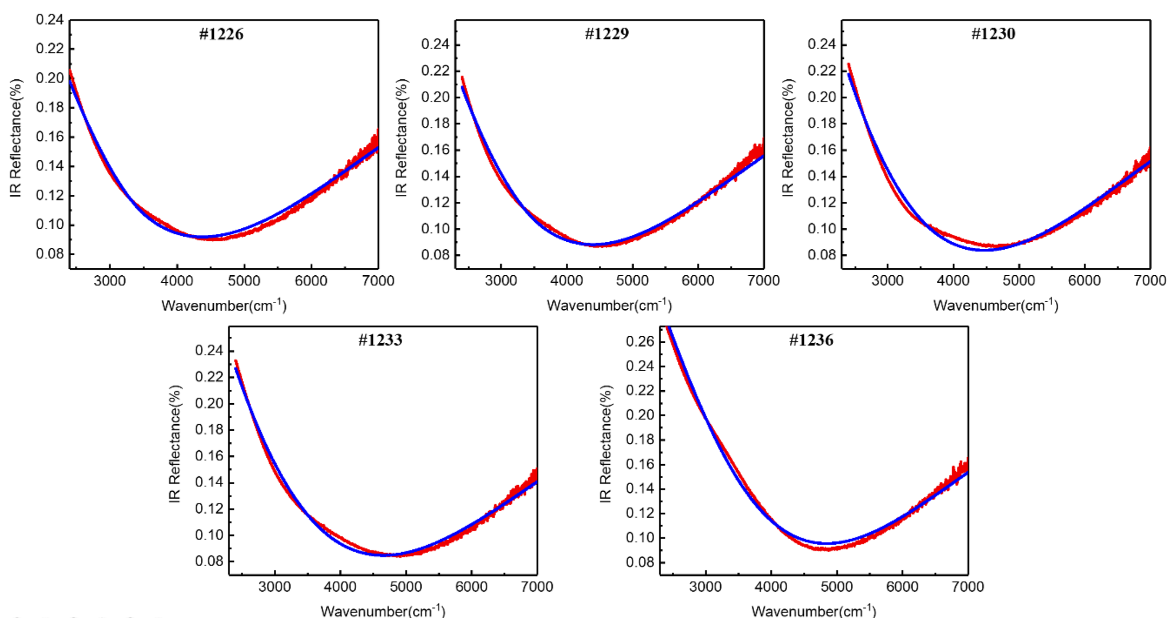

Figure 4.8 FTIR spectra fitting for sample set C

4.4.2 Impact of RF power on plasma parameters

For the set of samples grown at 2.2 Torr (Set A), the molecular nitrogen species density, consisting of both metastable and ionized molecular nitrogen, increases with increasing RF power up to 200W as more nitrogen can be excited by electrons. However, at high RF power, molecular nitrogen species density decreases due to the collisional quenching with other N_2 molecules. The collisional quenching becomes the dominant de-excitation process at higher pressures[126]. In contrast, both neutral and ionized atomic nitrogen loss through N–N gas-phase recombination requires three-body collisions, which do not begin to compete with the loss by diffusion to the chamber walls until higher pressures[126]. Since diffusion losses decrease with increasing pressure, ionized atomic nitrogen density increases with plasma power at lower pressures.

For the sample set grown at 3.8 Torr (Set B), The molecular nitrogen species density decreases with increasing power up to 375W as more N_2 molecules are dissociating into individual atoms and atomic ions as evident from the increase of atomic neutrals and atomic ions. The

increase in molecular nitrogen species after 375W might be caused by diffusion induced recombination of atomic ions into N_2 molecules[126, 137]. This indicates the loss of atomic ions through N-N gas-phase recombination as evident in Fig. 2.

The further increase in molecular nitrogen species seen in the sample set grown at 4.2 Torr (Set C) after 400W is the continuation of the diffusion induced recombination of atomic ions into N_2 molecules observed in the sample set grown at 3.8 Torr (Set B) resulting in an increased density of molecular nitrogen species.

4.4.3 Atomic nitrogen ions are the main contributors from nitrogen plasma

The analysis of the in-situ optical emission spectra along with the variation in growth rate indicates that the most dominant chemical combination resulting in InN formation in the present case is due to the chemical combination of atomic nitrogen ions with indium. The contribution of other nitrogen species to InN growth is negligibly small compared to that of the atomic nitrogen species. Considering the available nitrogen species in the plasma, the following are the possible chemical combinations resulting in InN.

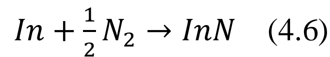

$$In + \frac{1}{2}N_2 \rightarrow InN \quad (4.6)$$

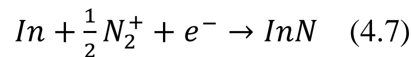

$$In + \frac{1}{2}N_2^+ + e^- \rightarrow InN \quad (4.7)$$

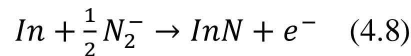

$$In + \frac{1}{2}N_2^- \rightarrow InN + e^- \quad (4.8)$$

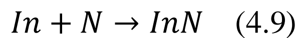

$$In + N \rightarrow InN \quad (4.9)$$

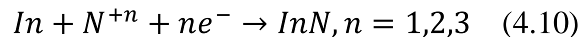

$$In + N^{+n} + ne^- \rightarrow InN, n = 1,2,3 \quad (4.10)$$

The previously discussed analysis of the in-situ optical emission spectra along with the variation in growth rate indicates that the most dominant chemical combination resulting in InN formation in the present case is given by equation (4.10). The contribution of other nitrogen species

to InN formation is either negligibly small, or they are hindering the InN formation rather than contributing to the growth.

Dependence of InN growth rate on the concentration of atomic nitrogen ions:

Correlation of the InN growth rate with atomic nitrogen ions is shown in Fig. 4.8. Growth rate increases with the increase of the atomic nitrogen ion flux controlled by the RF power level. Samples grown at different conditions (pressures, V/III ratios) demonstrate the same correlation.

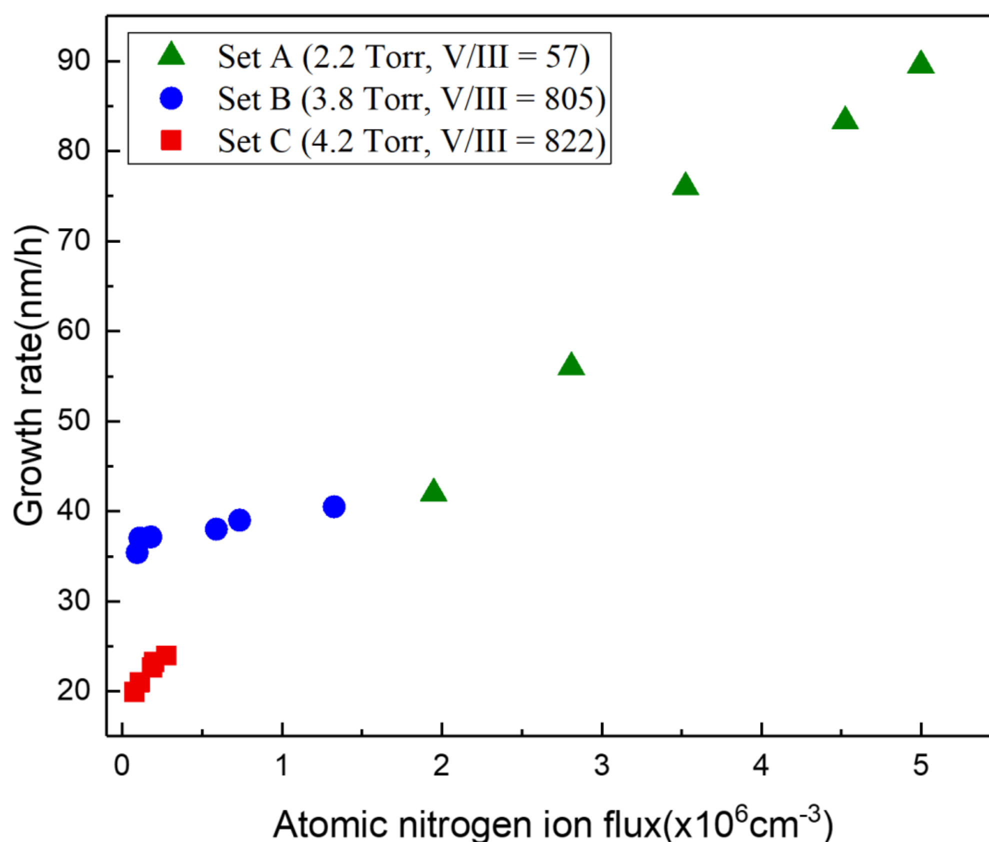

Figure 4.9 The film growth rate as a function of atomic nitrogen ion flux for three different sets of samples

4.4.4 Impact of nitrogen plasma species on InN structural properties

4.4.4.1 Raman spectroscopy

The influence of plasma species on the structural properties of InN has been studied via Raman spectroscopy. Raman spectra for the three sets of InN samples grown at various pressures is shown in Fig. 4. The E_2-high (489 cm^{-1}) and A_1-LO (590 cm^{-1}) phonon modes were observed in each of the sample sets.

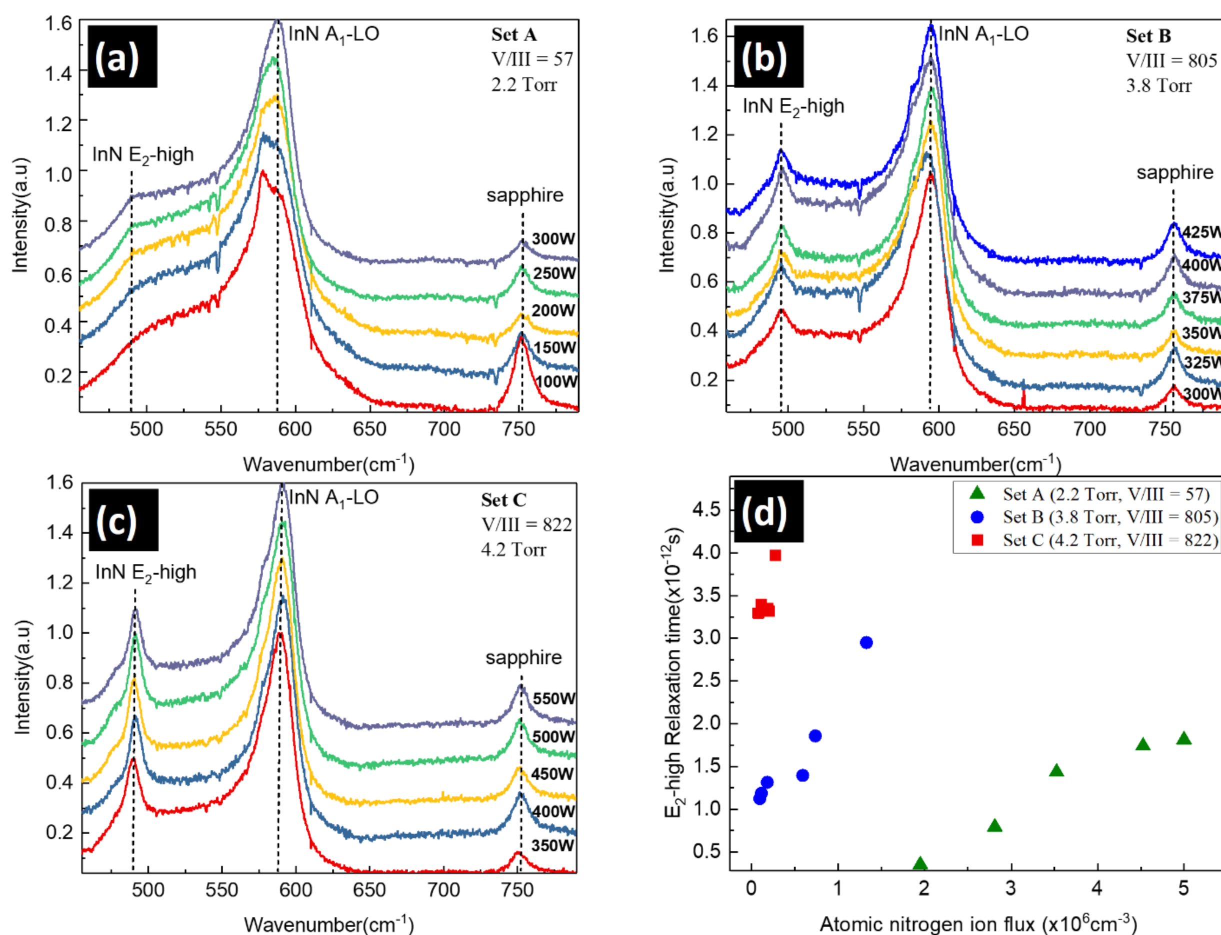

Figure 4.10 Raman spectra measured on InN films plotted for set A (a), set B (b) and Set C (c) . Numbers indicate the RF power levels. (d) The E2-high phonon mode relaxation time dependence on nitrogen ion flux

The phonon relaxation time was estimated using the FWHM and peak position of the E_2-high and A_1-LO phonon modes extracted from a multi-peak fit of the Raman spectra[137]. Fig

4(d) shows the E_2-high phonon mode relaxation time as a function of atomic nitrogen ion flux for each set of samples.

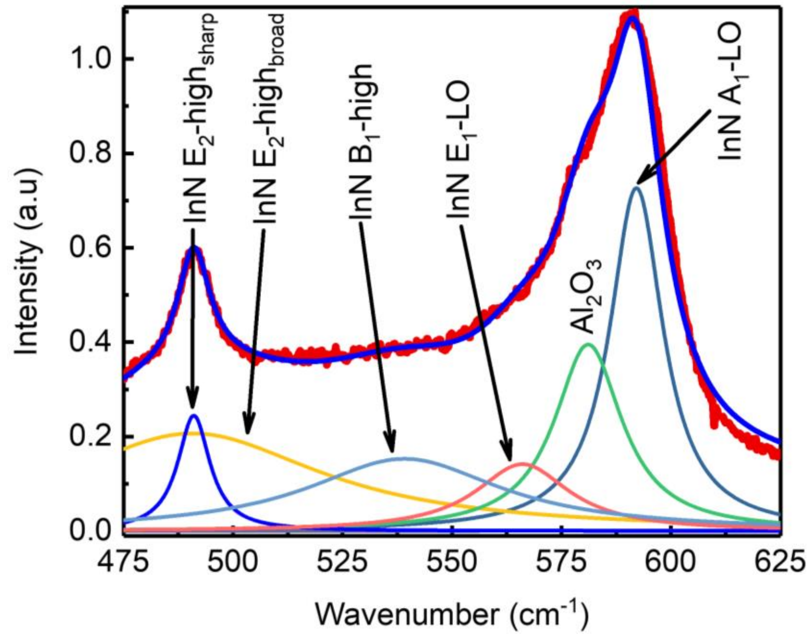

Figure 4.11 Example fitting of the Raman spectra measured on InN films plotted on the InN sample grown at 450W in set C. The phonon modes are labelled

The phonon lifetime in Raman spectroscopy is limited by the following two mechanisms: (i) anharmonic decay of the phonon into other phonons with a characteristic decay time and (ii) the perturbation of the translational symmetry of the crystal due to impurities and defects with distinctive decay time. A longer decay time for a phonon mode means smaller defect densities for that particular phonon mode. Although it is hard to distinguish between the contribution of both mechanisms, a characteristic decay time associated with the defects can be estimated using the FWHM of Raman fits[7]. The phonon lifetime τ can be determined from the Raman linewidth via the energy-time uncertainty relation.

$$\frac{1}{\tau} = \frac{2\pi \times \delta}{h} \qquad (4.11)$$

where δ is the Raman linewidth and "h" is the Planck's constant.

The E_2-high phonon relaxation time increases with the increase of atomic nitrogen ion flux within each of the sample sets. It is likely to be caused by a decrease in nitrogen vacancies in the grown InN which are primary contributors to the E_2-high mode[137]. No significant correlation has been observed between the A_1-LO phonon mode relaxation time and the atomic nitrogen ion flux.

4.4.4.2 X-ray diffraction

XRD spectra were recorded on several samples from Set A grown at 2.2 Torr with V/III=57. Figure 4.5 shows θ-2θ scans for three samples grown at RF power levels of 100W, 200W, and 300W. For all analyzed samples, peaks located at 31.38°, 64.90°, and 41.85° were identified as (0002) InN, (0004) InN, and the (0006) Al_2O_3 substrate respectively. Lower intensity peaks of $(10\bar{1}1)$ InN and $(20\bar{2}2)$ InN located at 33.0° and 69.22° respectively, indicate the polycrystalline structure of the grown film mostly crystallographically locked to the substrate. In order to achieve monocrystalline film most likely the InN growth initiation on sapphire surface should be optimized. The obtained XRD results are consistent with results previously reported by Gao et al.[48] for InN grown at 550 ˚C by MBE. Peaks labeled as "*" are likely artifacts of the 2°-offcut c-plane sapphire substrate as described by Mukherjee et al[138]. Increasing (0002) InN peak intensity with increasing RF power level correlates with increasing growth rate resulting in a thicker InN film.

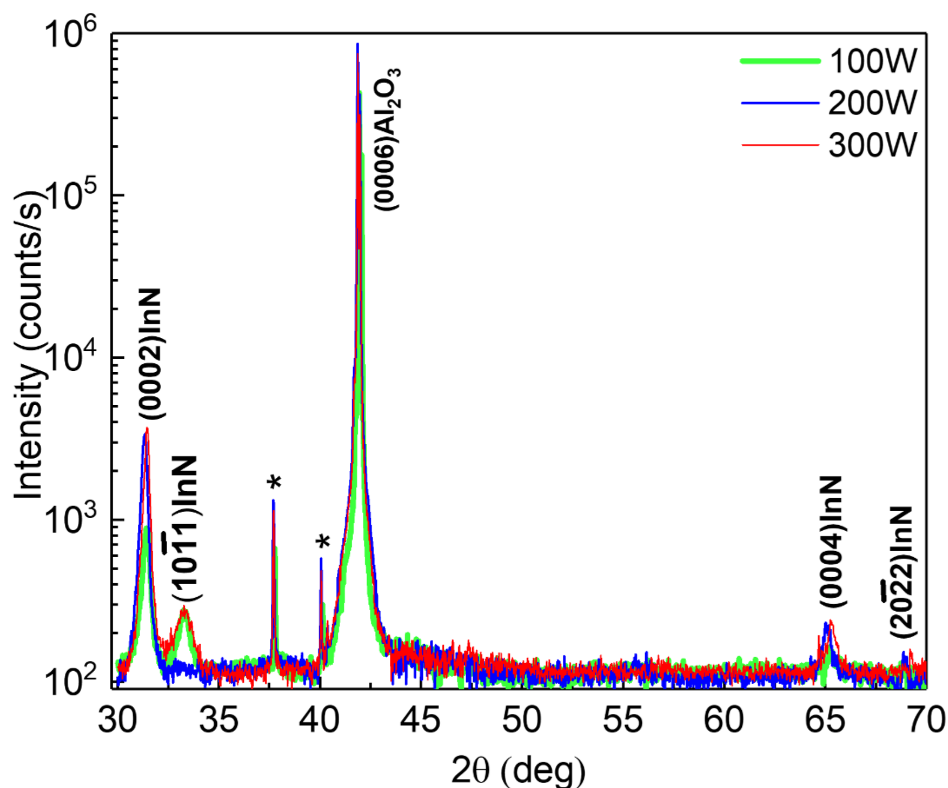

Figure 4.12 XRD spectra measured on InN films grown at 2.2Torr, V/III ratio of 57, at varying RF powers indicated in the legend

4.5 Conclusions

In summary, InN films were grown by PA-MOCVD. The composition of nitrogen plasma, used as the nitrogen precursor, was analyzed using optical emission spectroscopy. The atomic nitrogen ion species were shown to have a dominant impact on the InN growth rate compared to atomic nitrogen neutrals and molecular nitrogen species. The structural quality of the films was characterized by the E_2-high phonon mode relaxation time determined by Raman spectroscopy. InN structural quality was found to depend significantly on the flux of atomic nitrogen ions. This provides us with a better understanding of the InN growth mechanism in PA-MOCVD systems and paves the path for further nitride-based semiconductor growth optimization to achieve industrial-scale high-quality film growth in these systems.

5 SUPER-STURATION MODEL FOR INDIUM NITRIDE PA-MOCVD

5.1 Supersaturation

During InN growth in MOCVD reactor indium and nitrogen precursors decompose to release In and N ions which chemically react to form InN crystal in form of thin film. The crystallization process can be explained using the well-known principles of thermodynamic equilibria and kinetic rate processes. During the crystallization process the phase change from vapor to the solid phase for each reactant is driven by thermodynamics and the law of free energy minimization; in turn, this results from trade between the total enthalpy and entropy of a system.

As the molecules combine to form a crystal lattice, the order in the vapor-solid system increases resulting in a decrease in the global entropy of the vapor-solid system. This results in a reduction of the enthalpy and free energy of the system. This explains why a solid phase may be thermodynamically stable, and the preferred state for a system. Given, that most of the sample growth described in this thesis is done at temperatures above the InN decomposition temperature, thorough understanding of the growth thermodynamics should provide a guidance in finding suitable growth regime in the growth parameter space.

For any crystallization process, the supersaturation is the driving force (that "pushes" the reaction away from the equilibrium). Supersaturation defines weather a solid phase formation in a saturated solution is thermodynamically preferable [139]. In this chapter, the studies on the role of the indium supersaturation/chemical potential on the InN growth process and structural and optical characteristics for the PA-MOCVD process are described. Besides, a method for the thermodynamic indium supersaturation as a function of the certain growth parameters is presented. It was found that the growth surface morphology and the structural and optical properties are strongly correlated with the In supersaturation.

5.2 Calculation of supersaturation

The chemical reaction forming the InN is steered by the supersaturation of indium species in the gas phase. All thin film growth processes, including growth in PA-MOCVD systems, are non-equilibrium processes with a driving force toward the equilibrium. The driving force for thin film formation is the deviation from the thermodynamic equilibrium and can be quantitatively described by the change in free energy of the process[140] $\Delta G = -RT\ln(1+\sigma)$, where the σ is the supersaturation defined for indium as

$$\sigma = \frac{P_{In}^{input} - P_{In}^{eq}}{P_{In}^{eq}} \qquad (5.1)$$

Here P_{In}^{input} is the input partial pressure of the In and P_{In}^{eq} is the equilibrium partial pressure of In at given reaction conditions. The supersaturation for In can be calculated using the procedure described by Koukitu et al. for GaN[141]. The method of calculation will be based upon the molar flows of all the gases into the reactions chamber, the fraction of atomic nitrogen ions, the chamber pressure and substrate temperature. The equilibrium partial pressure of indium is calculated from the growth conditions, which is then plugged in to Eq. 5.1 to get the supersaturation.

Nitrogen gas through the plasma source (Plasma N_2) and trimethylindium (TMI) are injected into the reaction chamber, where they chemically combine to give InN. The chemical co,bination can be described as chemical equations as

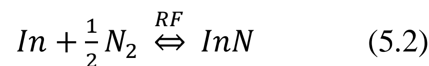

$$In + \frac{1}{2}N_2 \overset{RF}{\Leftrightarrow} InN \qquad (5.2)$$

The equilibrium equation corresponding to this reaction is the ratio of the activity of InN to the equilibrium partial pressure of indium P_{In} and square root of the partial pressure of plasma nitrogen i.e.

$$K = a_{InN}/P_{In}{P_{N_2}}^{1/2} \qquad (5.3)$$

The equilibrium constant "K" for the reaction can be described in terms of the substrate temperature T [129-133] as

$$\log_{10} K(T) = 15.7 + 3.82 \times \frac{10^4}{T} + 0.289 \log_{10}(T) \quad (5.4)$$

The total pressure of the system is assumed to stay constant during the growth process. It can be written as:

$$P_T = P_{In}^{eq} + P_{N_2} + P_{IG} \qquad (5.5)$$

Where P_{IG} is the partial pressure of "inert" gases, gasses that are not contributing to the final product. The examples of such gasses include the skirt flow of nitrogen that keeps heater safe from deposition, the nitrogen push flow in the TMI delivery line (see chapter 3 for details) etc. The sum of the partial pressures of only plasma N_2 and elemental In that are participating in the growth process, is termed as reduced pressure P_r.

$$P_r = P_{In}^{input} + P_{N_2}^{input} \qquad (5.6)$$

As described in in chapter 4, the chemical reaction occurring at the growth surface resulting in InN formation in PA-MOCVD is defined by the chemical combination of atomic nitrogen ions N^* with indium. Since only atomic nitrogen ions are contributing to chemical combination, the decomposition of molecular nitrogen can be expressed as

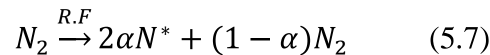

$$N_2 \xrightarrow{R.F} 2\alpha N^* + (1-\alpha) N_2 \qquad (5.7)$$

α is the fraction of atomic nitrogen ions N^* is introduced as in equation 5.7. It is the function of reactor pressure and RF power. At the increased reactor pressure α decreases as more atomic ions are forced to recombine to give neutral nitrogen molecules. Similarly α increases with increase in RF power as increased number of nitrogen molecules have been dissociated into atomic nitrogen ions.

For all PA-MOCVD growth process in this study, α is determined by analyzing the in-situ optical emission spectra of nitrogen, using the atomic emission spectroscopy[134-138]. Detailed description of this method is given in chapter 4.

the reduced pressure in equation 5.6, can be rewritten with use of the equation 5.7 as:

$$P_r = P_{In}^{input}\left\{1 + \frac{V}{III}(1+\alpha)\right\} \qquad (5.8)$$

where $\frac{V}{III}$ is the ratio of the input flow to nitrogen to input flow of indium. The molar conservation considerations (which itself is the consequence of mass conservation) give the following relation between partial pressures.

$$P_{In}^{input} - P_{In}^{eq} = P_{N_2}^{input} - P_{N_2}^{eq} \qquad (5.9)$$

Substituting equations 5.3, 5.4, 5.8 and 5.9 into equation 5.6, the final expression can be solved for the equilibrium partial pressure of indium P_{In}^{eq}.

$$(P_{In}^{eq})^3 - \left\{3P_{In}^{input} + (1+\gamma)P_{plasma\ N_2}^{input}\right\}\left(P_{In}^{eq}\right)^2 + \left(\frac{a_{InN}}{K}\right)^2 = 0 \qquad (5.10)$$

As was concluded in Chapter 4, the main chemical reaction that determines the growth process is defined by the ionized atomic nitrogen species and does not include the other plasma radicals of nitrogen, such as atomic neutrals and molecular ions. Therefore these radicals are not considered. However, these radicals may contribute to the growth process through their kinetic energy, but they will not determine the yield of the end products as given by the supersaturation. Consequently, the reduced total pressure, which remains constant throughout the growth process, is determined in terms of the input partial pressure of group III species, input V/III ratio, and the parameter α which can be determined from the in-situ optical emission spectra using the techniques of atomic spectroscopy.

As the supersaturation and chemical potential is dependent on the PA-MOCVD process parameters, there are various combinations of PA-MOCVD parameters that can lead to the same supersaturation and chemical potential and should, according to the above, produce the same results, which is not evident from the growth parameters themselves. According to the above described thermodynamic model of supersaturation, the III-metal supersaturation is influenced by PA-MOCVD process parameters, as shown in Fig 5.1. According to the model, the supersaturation was found to be more sensitive to the input indium concentration than the other parameters.

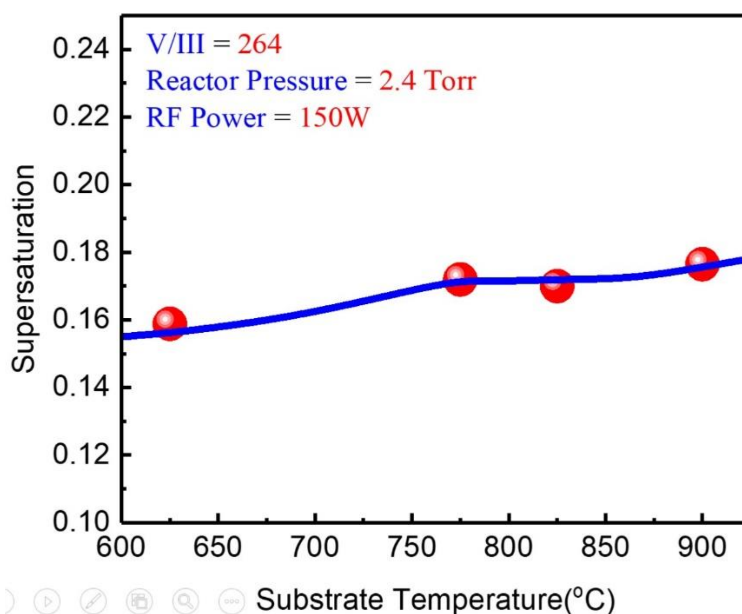

Figure 5.1 The dependence of supersaturation on substrate temperature

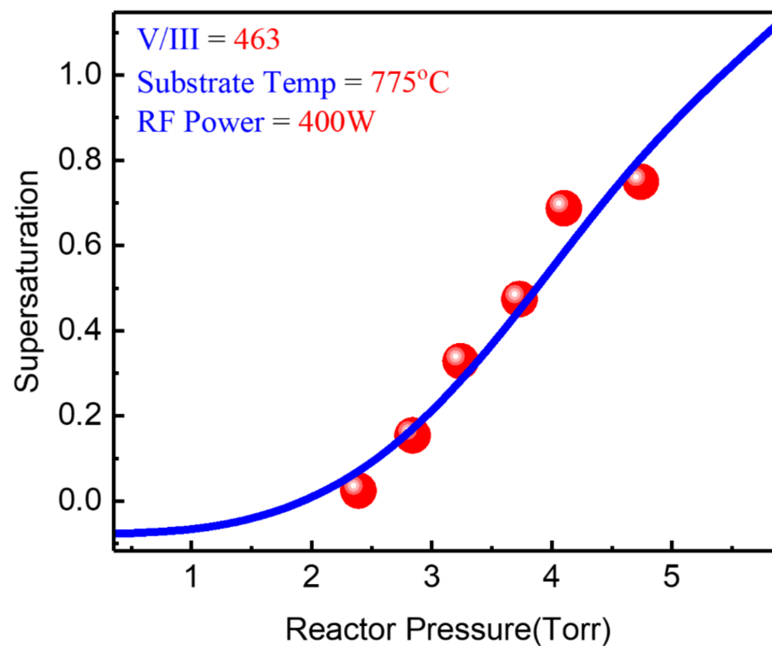

Figure 5.2 The dependence of supersaturation on reactor pressure

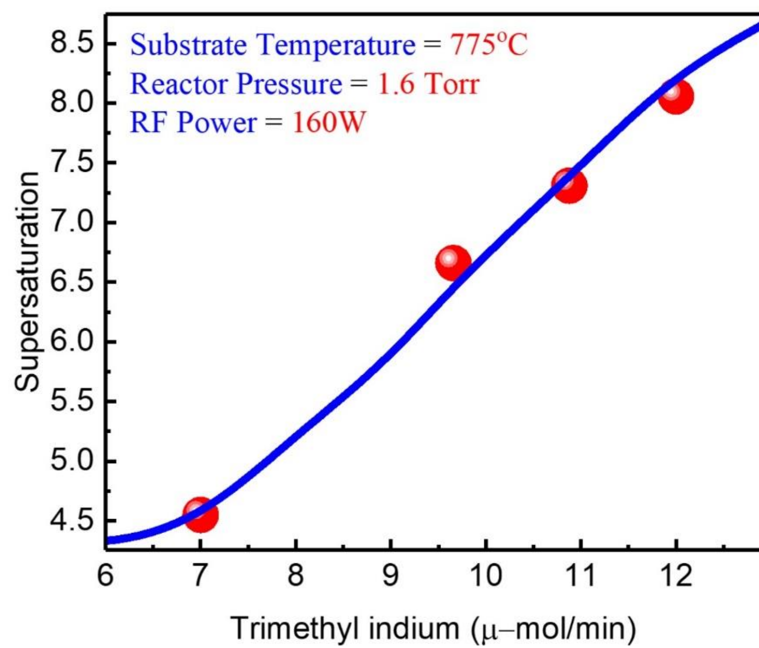

Figure 5.3 The dependence of supersaturation on input trimethyl indium

5.3 Sample growth

The growth parameters of the two sets of InN samples, grown for this study, are summarized in the Table 5.1. The supersaturation for each sample was calculated using the method described in section 5.1.

Table 5.1 The growth conditions used for sample sets D and E. For set D the supersaturation was varied by varying the input indium. For set E, three samples grown at widely different growth conditions resulting into indium supersaturation ~ 2

Set	Sample I.D.	V/III molar ratio	Reactor pressure(Torr)	RF power(W)	σ
D	1393	28	2.6	150	8.26
D	1395	31	2.6	150	7.38
D	1394	35	2.6	150	6.42
D	1396	41	2.6	150	4.61
E	1423	257	3.8	550	2.03
E	1428	217	3.2	530	2.13
E	1425	194	2.4	400	2.09

For the set D of samples, four samples were grown at varying TMI input flows. Supersaturation values varied from 4.61 to 8.26. The RF power was fixed at 150W and the reactor pressure at 1.6 Torr.

For set E of samples (3 samples, listed in the Table 5.1) at TMI input flows, reactor pressure, and RF power growth parameters were selected in a way to have the same In supersaturation σ=2 and hence the same chemical potential. The growth conditions for both the sample sets are summarized in table 1 and original growth logs have also been shown in Fig 5.3.

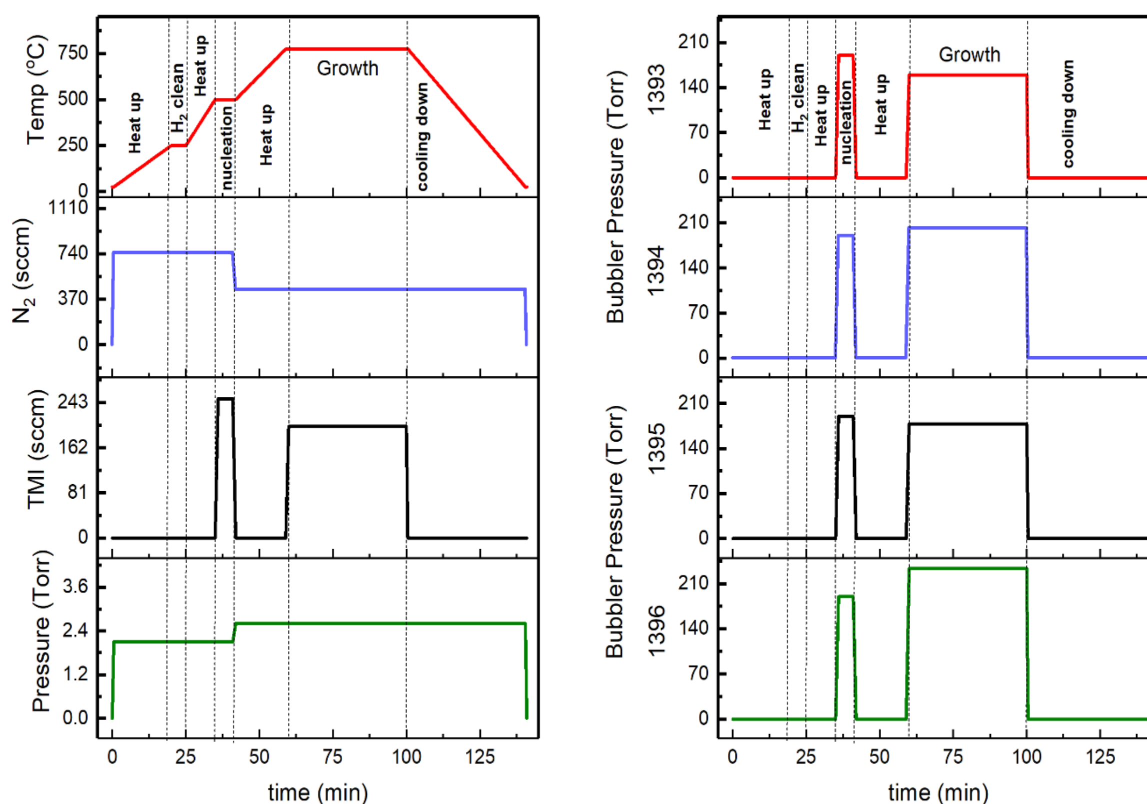

Figure 5.4 Growth conditions for sample set D

The substrate preparation steps for three sets were kept the same and are as follows. Sapphire substrates were heated to 250ºC. At 250ºC the substrates were exposed to 100sccm of H_2 gas at 2.1Torr for 5 minutes. After that, the substrates were further heated to 500ºC in nitrogen gas keeping the pressure at 2.1Torr. The InN nucleation layer was deposited at 500ºC, 2.1Torr, 150W RF power, 750sccm N_2 plasma and 250sccm Trimethylindium for 5 mins. The samples were further heated to 775ºC. And then the films were grown at the conditions mentioned in Table 5.1.

5.4 Results and discussion

5.4.1 Influence of indium supersaturation on structural properties of InN

5.4.1.1 Raman Analysis

The impact of indium supersaturation on the structural properties of InN has been studied via Raman spectroscopy. Raman spectra for the two sets of InN samples grown at various supersaturation levels (and chemical potential) are shown in Figure 5.4. The E_2-high (489 cm^{-1}) and A_1-LO (590 cm^{-1}) phonon modes were observed in each of the sample sets, additionally the substrate (Al_2O_3) peak is also observed at 751cm^{-1} and at around 575cm^{-1}. The phonon relaxation time in Raman spectroscopy is limited by the following two mechanisms: (i) anharmonic decay of the phonon into other phonons with a characteristic decay time and (ii) the perturbation of the translational symmetry of the crystal due to impurities and defects with distinctive decay time. A longer decay time for a phonon mode means smaller defect densities for that particular phonon mode. Although it is hard to distinguish between the contribution of both mechanisms, a characteristic decay time associated with the defects can be estimated using the Raman linewidths[137]. The phonon lifetime τ was determined from the Raman linewidth via the energy-time uncertainty relation.

$$\frac{1}{\tau} = \frac{2\pi \times \delta}{h} \qquad (5.11)$$

Where δ is the Raman linewidth, and "h" is the Planck's constant.

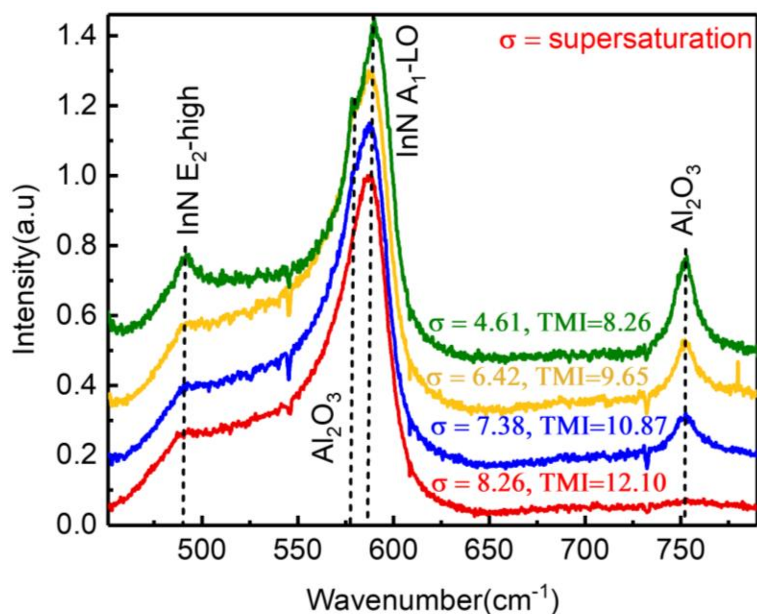

Figure 5.5 Raman spectra measured on InN films plotted for set D. Numbers indicate the indium supersaturation levels

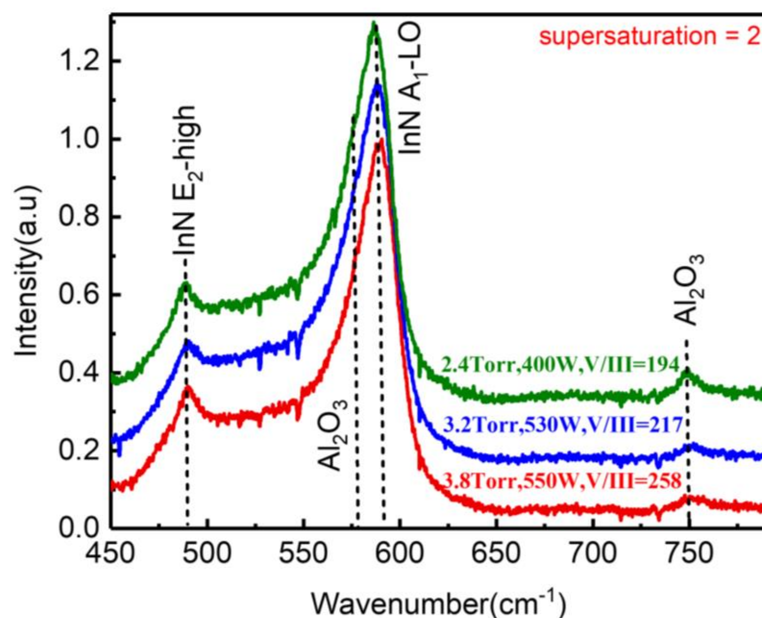

Figure 5.6 Raman spectra measured on InN films plotted for set E. Numbers indicate the growth conditions resulting in indium supersaturation level of 2

The phonon relaxation time was estimated using the FWHM and peak position of the E_2-high and A_1-LO phonon modes extracted from a multi-peak fit of the Raman spectra[137]. Fig 5.6 shows the E_2-high phonon mode relaxation time as a function of supersaturation for each set of samples. The E_2-high phonon relaxation time decreases with the increase of indium supersaturation in sample set A. It is likely to be caused by the increase in nitrogen vacancies in the grown InN, which are primary contributors to the E_2-high phonon mode[137]. No significant correlation has been observed between the A_1-LO phonon mode relaxation time and the indium supersaturation. For the sample set B, the E_2-high phonon relaxation time remains the same for the whole series.

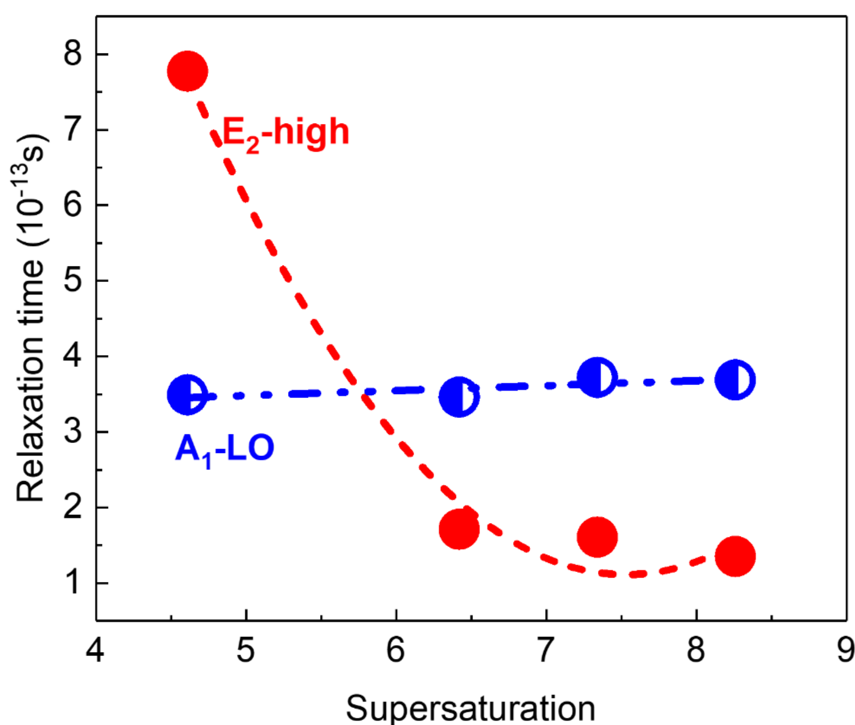

Figure 5.7 The E2-high and A1-LO phonon mode relaxation time dependence on indium supersaturation level for set A.

Table 5.2 Phonon relaxation time for sample sets D and E. For set A the supersaturation was varied by varying the input indium. For set E, three samples grown at widely different growth conditions resulting into indium supersaturation of 2

Set	**Indium supersaturation**	**E_2-high relaxation time (10^{-12} s)**	**A_1-LO relaxation time (10^{-12} s)**
D	8.26	1.35	3.68
D	7.38	1.60	3.72
D	6.42	1.75	3.46
D	4.61	7.77	3.49
E	2.03	7.49	3.75
E	2.09	7.44	3.97
E	2.13	7.39	3.72

It is due to the fact that the indium supersaturation is kept almost constant for the whole series, which results in the same chemical potential and hence dictates the similar reaction kinetics. As a result, the grown films exhibit similar structural properties. The phonon relaxation time for both the sample sets is summarized in table 5.2.

5.4.1.2 X-ray diffraction

XRD spectra were recorded on several samples from SetB grown at the indium supersaturation level of 2. Fig 5.7 shows θ-2θ scans for these samples. For all analyzed samples, peaks located at 31.38°, 64.90°, and 41.85° were identified as (0002) InN, (0004) InN, and the (0006) Al_2O_3 substrate respectively. Lower intensity peaks of $(10\bar{1}1)$ InN and $(20\bar{2}2)$ InN located at 33.0° and 69.22°, respectively, indicate the polycrystalline structure of the grown film mostly crystallographically locked to the substrate. In order to achieve monocrystalline film, most likely, the InN growth initiation on the sapphire surface should be optimized. The obtained XRD results are consistent with results previously reported by Gao et al.[94] for InN grown at 550 ˚C by MBE.

Peaks labeled as “*” are likely artifacts of the 2°-offcut c-plane sapphire substrate as described by Mukherjee et al[138].

The crystallite size in each of the sample in set B was determined using Scherrer equation[142],[143] given as

$$\tau = \frac{k\lambda}{\beta sin\theta_{hkl}} \qquad (5.12)$$

Such that τ is the crystallite size, λ is the X-ray wavelength, β is FWHM of the XRD peak and θ_{hkl} is the diffraction angle. For three samples in set B since the supersaturation values are close enough ~ 2, the crystallite sizes for these samples are also very close, varying between 71nm to 76nm. This trend seen in Table 5.3 is also complemented by the grain sizes determined by AFM for the same sample set.

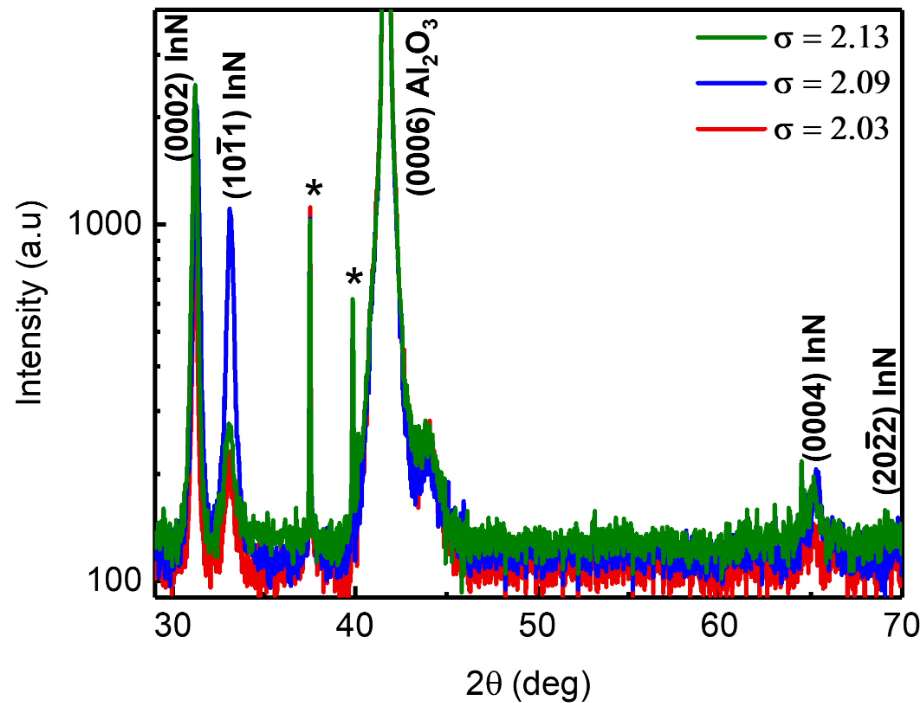

Figure 5.8 XRD spectra measured on InN films grown at widely different conditions, all of which result into Indium supersaturation level 2

Table 5.3 The crystallite sizes in (0002) direction determined from XRD for sample set B grown at indium supersaturation ~ 2

Set	V/III molar ratio	Reactor pressure(Torr)	RF power(W)	Supersaturation	Crystallite size (0002)
B	257	3.8	550	2.03	70.89 ± 2.9
B	194	2.4	400	2.09	73.44 ± 3.1
B	217	3.2	530	2.13	76.09 ± 2.8

5.4.1.3 Fourier Transform Infrared Spectroscopy

The growth rate was determined as the ratio of the film thickness to the total growth duration in the units of nm/h. The film thickness was determined by fitting the FTIR reflection spectra shown in Figure 5.7. The fitting range used in the spectra lies between 2200 cm^{-1} and 7000 cm^{-1}. FTIR fitting was performed using a multi-layer stack modelling method described by Senevirathna et. al[144].

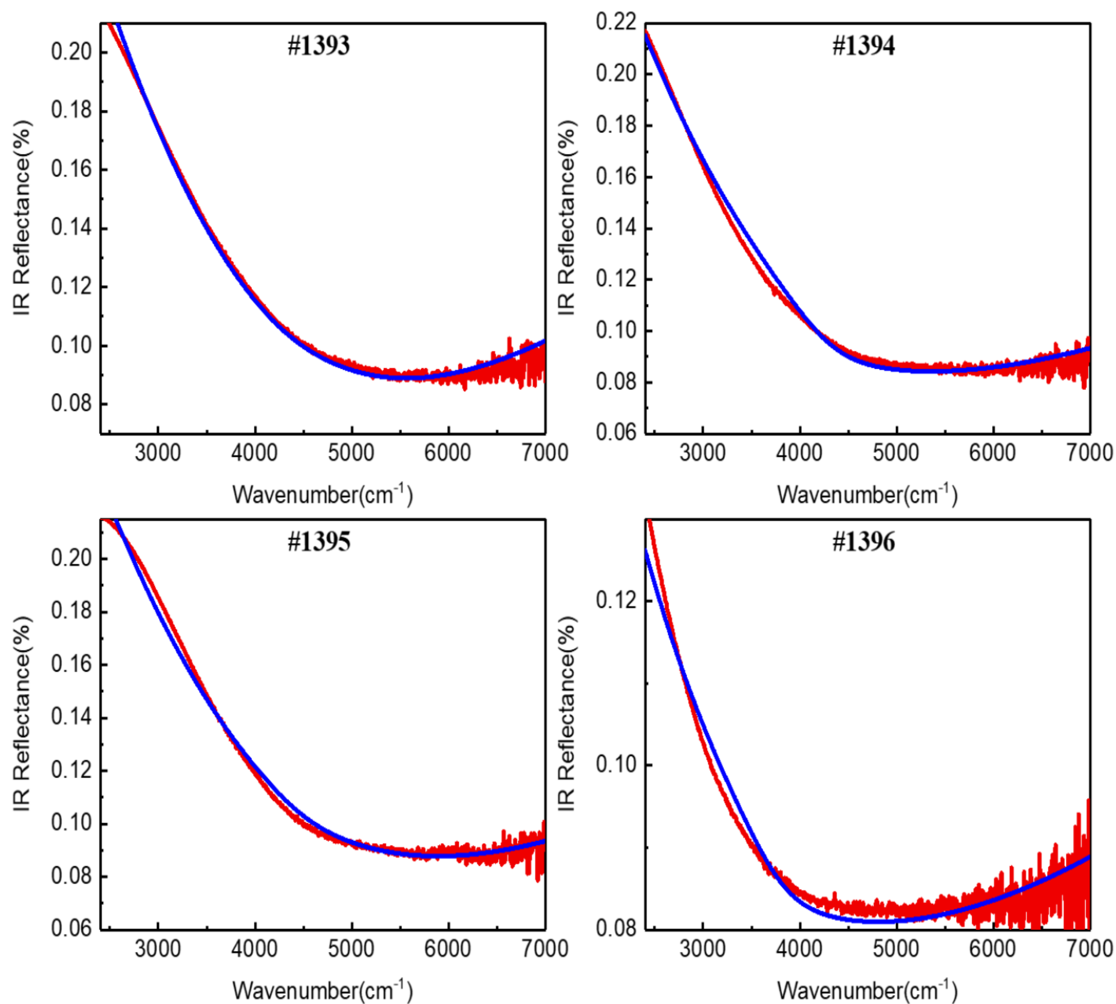

Figure 5.9 Experimental IR reflectance spectra measured on InN films plotted for set D and their simulated fitting

Table 5.4 Growth rate vs. supersaturation for sample sets D. The supersaturation was varied by varying the input indium

Sample ID	Super-saturation	Film thickness (nm)	Growth duration (min)	Growth rate (nm/h)
1393	8.26	67	45	89.34
1395	7.38	61	50	73.2
1394	6.42	64	60	64
1396	4.61	59	70	50.57

5.4.2 Influence of indium supersaturation on the surface morphology of InN

In order to evaluate the influence of supersaturation on the surface morphology of InN in PA-MOCVD, atomic force microscopy was used. Fig 5.8 shows 1x1μm^2 AFM images of InN films grown at widely different growth conditions, all of them resulting in an indium supersaturation of 2. All the grown films exhibited surface morphologies with varying grain sizes and RMS roughness with a strong correlation with the supersaturation. The surfaces of these films exhibited similar surface morphologies with 4.27 nm to 4.41 nm RMS roughness and average grain sizes varying between 40nm to 45nm.

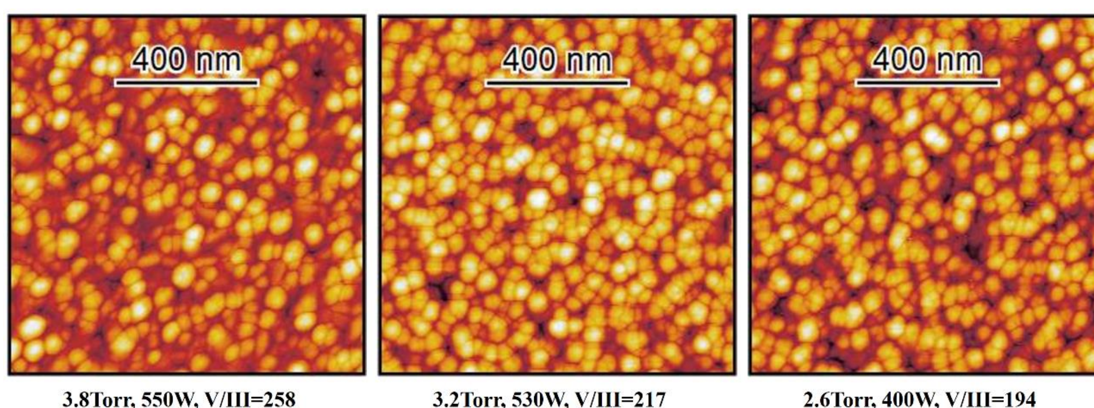

Figure 5.10 Surface morphology measured on InN films plotted for set E via Atomic Force Microscopy. Numbers at the bottom of each image indicate the growth conditions resulting in indium supersaturation level of 2

5.5 Conclusions

In this chapter I described the indium supersaturation model for the PA-MOCVD process is presented. The Gibbs free energy of the reaction of the reaction is linked to the supersaturation by the equation. The supersaturation depends upon the growth conditions used. Since there are many different combinations of growth parameters that can give the same supersaturation, the films grown at those different conditions belonging to a single value of supersaturation should

have similar structural and morphological properties, since the reaction kinetics stay same because of unaltered supersaturation. It was also found experimentally that films that were grown at different growth conditions belonging to the same supersaturation exhibit the similar structural and morphological properties. The grown samples were characterized using Raman spectroscopy, X-ray diffraction, and AFM. This study suggests that the supersaturation should be considered as a universal growth parameter instead of considering the individual growth parameters.

6 IMPACT OF PLASMA POTENTIAL ON INDIUM NITRIDE PA-MOCVD GROWTH KINETICS AND STRUCTURAL PROPERTIES

In this chapter, I am discussing the effect of various growth parameters of PA-MOCVD on the plasma potential. The impact of varying plasma potential on the growth and structural properties of the InN films, and how the growth process and film properties will be affected if an external DC bias perturbs the plasma potential.

6.1 Plasma potential and plasma sheath

A gas-phase plasma consists of electrons, ions, and neutrals. In plasma, the densities of electrons and ions are the same on average so that the plasma is electrically neutral as a whole. In RF plasma, owing to their smaller mass, on average the electron speed is much larger than that of the ions[145]. Hence, the charge distribution between the plasma source and the grounded substrate is not uniform: more electrons reach substrate per unit time than ions.

InN studied in this thesis is grown by plasma-assisted MOCVD, in which the plasma source is positioned above the grounded sample surface (see Chapter 2 for detailed description). Therefore, a negative potential builds upon the substrate with respect to the plasma. The potential at the substrate affects the motion of ions and electrons near it. Therefore, in normal circumstances, the bulk of the plasma is positively charged with respect to the substrate. The plasma sheath, thus, represents the non-neutral potential region between the plasma and the substrate. Ions and electrons recombine at the substrate and leave the plasma system.

The difference in potential of the bulk plasma and the substrate gives rise to an electric field that accelerates ions towards the substrate. A grounded substrate draws currents from the plasma. If not grounded, it floats at a potential, that can be measured. The plasma is essentially

quasi-neutral and is at a constant positive potential V_P. The floating potential developed at the isolated substrate can be termed as V_f. If the substrate is an insulator, different parts of its surface may be at different floating potentials due to the difference in the distribution of electron speeds in the local area surrounding the plasma and the electric field set up in the insulator itself. This can result in a non-uniform film growth.

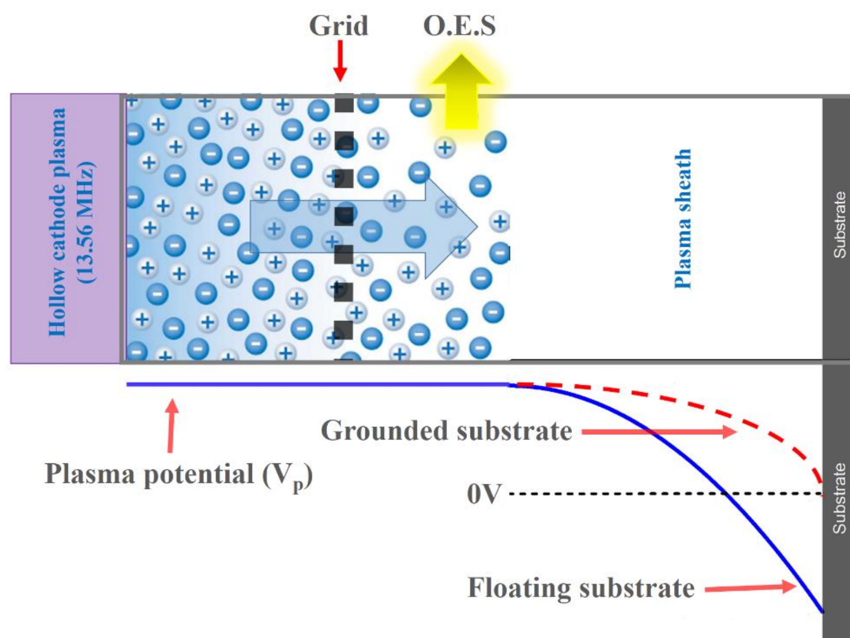

Figure 6.1 Schematic of the electric potential distribution in the remote PA-MOCVD system. OES represents the optical emission spectroscopy (distances are not to the scale)

6.2 Plasma sheath dynamics

A thorough understanding of the dynamics of plasma sheath formed over a substrate by an RF plasma is essential in the fundamental as well as practical aspects. The plasma sheath dynamics control the energy and distribution of ions reaching the substrate, which, consequently, affects the surface reaction rate, surface morphology, crystalline, and electrical properties of the resulting films. High-density plasma reactors have the advantage of quasi-independent control of plasma

density and ion bombardment energy[146]. In PECVD systems, it can be achieved by separating plasma production (Hollow cathode plasma source operating at 13.56 MHz in our case) from the bias voltage applied to the substrate or a grid in between the plasma source and the substrate. The effect of the grid bias on the PA-MOCVD process will be discussed later in the section 6.5 of this chapter.

A plasma sheath model developed by Theodoros and Demetre for a collisionless sheath[147] has been used in the present analysis. The variation in potential within the sheath is described by the Poisson's equation:

$$\nabla^2 V = -\frac{\rho}{\epsilon_o}\ , \quad (6.1)$$

where V is potential, ρ is the charge density in plasma, and ϵ_o is the permittivity of free space. The density ρ in the plasma may be expressed as

$$\rho = e(n_i - n_e)\ , \qquad (6.2)$$

where e is the electron charge, n_i is the ion density, and n_e is the electron density. Following the Boltzmann distribution, the electron density is given by:

$$n_e(x,t) = n_e(x_s,t)\exp\left(\frac{V(x,t)-V(x_s,t)}{k_B T_e}\right), \qquad (6.3)$$

where x_s represents the sheath edge, T_e is the electron temperature. The determination of n_e and T_e from plasma emission spectra is based upon the assumption that electrons have a Maxwellian energy distribution. The electron temperature was also assumed to be constant in the bulk of the plasma, both spatially and temporally. Moreover, if the sheath is considered to be collisionless, the ion density n_i and ion fluid velocity u_i can be described by the following conservation equations.

$$n_i(x,t)u_i(x,t) = n_i(x_s,t)u_i(x_s,t) \quad (6.4)$$

$$\frac{m_i}{2}u_i{}^2(x,t) + e\bar{V}(x,t) = \frac{m_i}{2}u_i{}^2(x_s,t) + e\bar{V}(x_s,t) \quad (6.5)$$

Equation 6.4 is based upon the assumption of adiabatic ions[148]. Equations 6.4 and 6.5 can be solved for the ion density:

$$n_i(x,t) = n_i(x_s,t)(1 - \frac{2e}{m_i u_i{}^2(x_s,t)}\left(\bar{V}(x,t) - \bar{V}(x_s,t)\right))^{-\frac{1}{2}} \quad (6.6)$$

Ions respond to an effective damped potential $\bar{V}$ (or field) rather than the actual potential V.

$$\frac{\partial \bar{V}}{\partial t}(x,t) = \frac{\bar{V}(x,t) - V(x,t)}{\tau_i} \quad (6.7)$$

where τ_i is the time that ions take to transit through the sheath. In Equation 6.7 τ_i acts as a time constant that controls the time averaging of $\bar{V}$. Numerically τ_i is the inverse of the ion plasma frequency.

$$\tau_i = \frac{1}{\omega_{Pi}} = \sqrt{\frac{\epsilon_o m_i}{e^2 n_s}} \quad (6.8)$$

Here, n_s is the plasma density at the sheath edge.

Equations 6.2, 6.3, 6.6, and 6.7 may now be substituted back into equation 6.1 to get the following equations that describe the sheath dynamics.

$$-\frac{e(n_i(x) - n_e(x))}{\epsilon_o} =$$

$$\frac{en_e(x_s)}{\epsilon_o}\left\{\exp\left(\frac{V(x,t) - V(x_s,t)}{k_B T_e}\right) - \left\{1 - \frac{2e}{m_i u_i{}^2(x_s,t)}\left(\bar{V}(x,t) - \bar{V}(x_s,t)\right)\right\}^{-\frac{1}{2}}\right\} \quad (6.9)$$

Equation 6.9 governs the sheath potential and ion and electron densities. The sheath would be a positive space charge region only if

$$\nabla^2 V < 0; \quad x > 0 \qquad (6.10)$$

and

$$\nabla^2 V = 0; \quad x = 0 \qquad (6.11)$$

Condition 6.10 implies that

$$\left\{1 - \frac{2e}{m_i u_i^2(x_s,t)}\left(\bar{V}(x,t) - \bar{V}(x_s,t)\right)\right\}^{-\frac{1}{2}} > \exp\left(\frac{V(x,t)-V(x_s,t)}{k_B T_e}\right),$$

which can be simplified to

$$u_i(x_s,t) > \sqrt{\frac{k_B T_e}{m_i}} \qquad (6.12)$$

Condition 6.10 implies that only the ions that have a velocity $\sqrt{\frac{k_B T_e}{m_i}}$ or greater can enter the sheath. This velocity is called Bohm velocity, and condition 6.12 is the Bohm criterion.

$$u_B = \sqrt{\frac{k_B T_e}{m_i}} \qquad (6.13)$$

The Bohm criterion guarantees the ion flux towards any object that is negatively charged with respect to the plasma. The ions thus have to enter the sheath with a velocity that is much larger than the thermal velocity. Hence there must be an electric field in the quasi-neutral region of the plasma that accelerates ions to an energy of at least $\frac{1}{2}k_B T_e$ towards the sheath edge. This field is usually associated with collisions, ionization, or other sources of particle collisions. This region is also referred to as the presheath, which extends over distances of the order of plasma dimensions, and the presheath field is weak enough not to violate the quasi-neutrality condition.

6.3 Sample growth, plasma potential measurement and emission spectra acquisition

Four InN film sample sets (labeled as A, B, C, and D) were grown using PA-MOCVD on c-plane Al_2O_3 wafers offcut at 0.2° towards m-plane. Trimethylindium (TMI) and nitrogen plasma were used as group-III and group-V precursors, respectively. The nitrogen plasma was produced using an RF hollow cathode plasma source. Nitrogen gas was used as the TMI carrier gas.

The substrate preparation steps for four sets were kept same and are as follows. Sapphire substrates were heated to 250°C. At 250°C the substrates were exposed to 100sccm of H_2 gas at keeping the pressure at 2.1Torr. The InN nucleation layer was deposited at 500°C, 2.1Torr, 150W RF power, 750sccm N_2 plasma and 250sccm Trimethylindium for 5 mins. The samples were further heated to 775°C. The unconventional high-temperature growth of InN has been previously demonstrated by our group[149]. The growth conditions used for each of the sample sets are summarized in Tables 6.1.

Table 6.1 Growth conditions for sample sets A, B and C

Sample set	**Sample ID**	**TMI µ-mol/min**	**Plasma-N_2 µ-mol/min**	**Growth pressure (Torr)**	**RF power (W)**	**Grid bias (V)**	**Growth Temperature (°C)**
A	1254	1.03	**447**	4.11	400	Float	775
A	1253	1.03	**640**	4.11	400	Float	775
A	1252	1.03	**750**	4.11	400	Float	775
A	1248	1.03	**931**	4.11	400	Float	775

B	1281	1.03	484.5	**2.8**	400	Float	775
B	1275	1.03	484.5	**3.4**	400	Float	775
B	1278	1.03	484.5	**3.8**	400	Float	775
B	1277	1.03	484.5	**4.1**	400	Float	775
B	1276	1.03	484.5	**4.8**	400	Float	775
C	1410	8.39	484.5	2.2	**100**	Float	775
C	1409	8.39	484.5	2.2	**150**	Float	775
C	1411	8.39	484.5	2.2	**200**	Float	775
C	1412	8.39	484.5	2.2	**250**	Float	775
C	1413	8.39	484.5	2.2	**300**	Float	775

Optical emission spectroscopy was employed to measure a range of the plasma parameters, including the fluxes and densities of neutral/ionic species and the plasma temperature[150],[151],[152]. Detailed description of this technique can be found in Chapter 4. The emission spectra were measured as close as possible to the growth surface via a quartz window. The floating potential at the grid is the result of a continuous bombardment of the various plasma species onto the grid. It is the function of different process parameters such as chamber pressure, nitrogen flow through plasma source, and the plasma power. The floating potential was externally measured at the grid for each set of samples.

Table 6.2 Growth conditions for set D; the grid bias series

TMI μmol/min	Plasma-N_2 μ-mol/min	Growth pressure (Torr)	RF power (W)	Grid bias (V)	Growth Temperature (°C)
4.25	37.25	0.35	50	**-100**	775
4.25	37.25	0.35	50	**-50**	775
4.25	37.25	0.35	50	**ground**	775
4.25	37.25	0.35	50	**+50**	775
4.25	37.25	0.35	50	**+100**	775

For the sample set A, the input Plasma N_2 flow was varied in the range 447 – 931 μmol/min. For the set B, the reactor pressure was varied in the range 2.8 – 4.8 Torr. For the set, the RF power vas varied in the range 100 – 300 W. For the set D of samples, all the growth parameters were kept constant and the grid was externally biased with a DC potential. The grid bias was varied from -100V to +100V.

6.4 Correlation of plasma potential (V_P) with various plasma species

All the plasma emission spectra were analyzed using the methods of atomic and molecular spectroscopy, using the Boltzmann equation and Saha equation following the method described in Chapter 4. The results of the plasma analysis for each of the grown samples are summarized in Fig. 6.2. The variation in the density of atomic nitrogen ions is found to be in good correlation

with the change in the plasma potential measured at the grid. However, no correlation is found between the plasma potential and the variation in atomic neutrals or molecular plasma species.

For the sample set A (4.12Torr, 400W, 1.03μ-mol/min TMI), the molecular nitrogen

Species density, consisting of both metastable and ionized molecular nitrogen, decreases with increasing input nitrogen flow through the plasma source. The plasma temperature (average ion energy) also decreases with an increase in the input nitrogen flow as the same energy given by the plasma source is now distributed among more of the species than before. The atomic nitrogen ions density increases with input nitrogen at the given conditions.

For the sample set B (varying growth pressure set), the molecular nitrogen species density increases upon increasing the chamber pressure. With increasing pressure, the collisional quenching and diffusion induced recombination become the dominant de-excitation processes. These processes result in the recombination of atomic ions into N_2 molecules[126]. These two processes cause a decrease in atomic nitrogen ions.

For the set C (varying plasma power set), the molecular nitrogen species density, consisting of both metastable and ionized molecular nitrogen, increases with increasing RF power up to 200 W as more nitrogen can be excited by electrons. However, at high RF power, molecular nitrogen species density decreases, likely due to the collisional quenching with other N_2 molecules. The collisional quenching becomes the dominant de-excitation process at higher pressures[126]. In contrast, both neutral and ionized atomic nitrogen loss through N–N gas-phase recombination require three-body collisions, which do not begin to compete with the loss by diffusion to the chamber walls until higher pressures[126]. Since diffusion losses decrease with increasing pressure, ionized atomic nitrogen density decreases with the chamber pressure at constant RF power.

For the sample set D (varying grid potential set), the density of molecular species (consisting of both metastable and ionized molecular nitrogen) and atomic nitrogen ions decreases with increasing grid bias. The plasma temperature (average ion energy) also decreases with an increase in the grid bias. It can be attributed to increased repulsion faced by the positive ions due to increased potential at the grid.

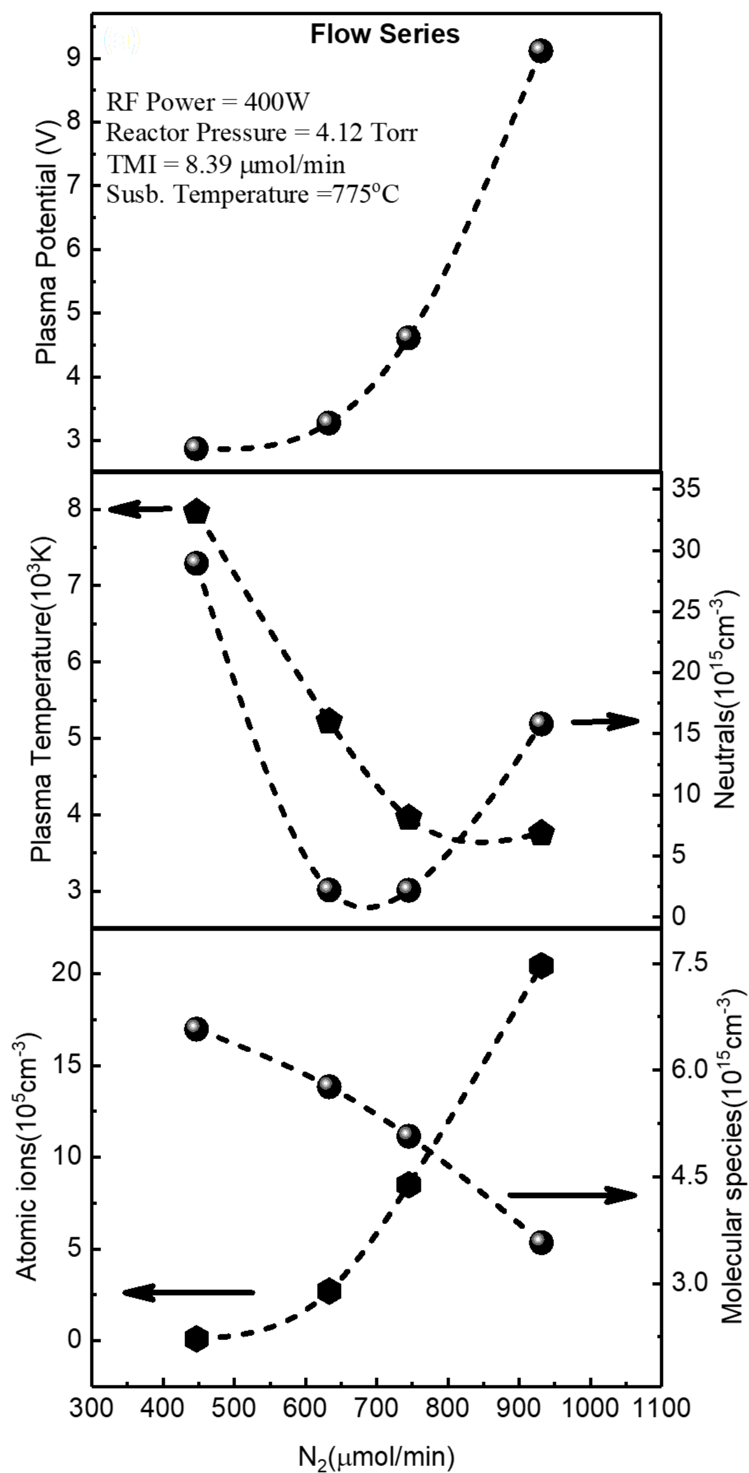

Figure 6.2 Variation in plasma potential and plasma composition with plasma N_2 flow rate

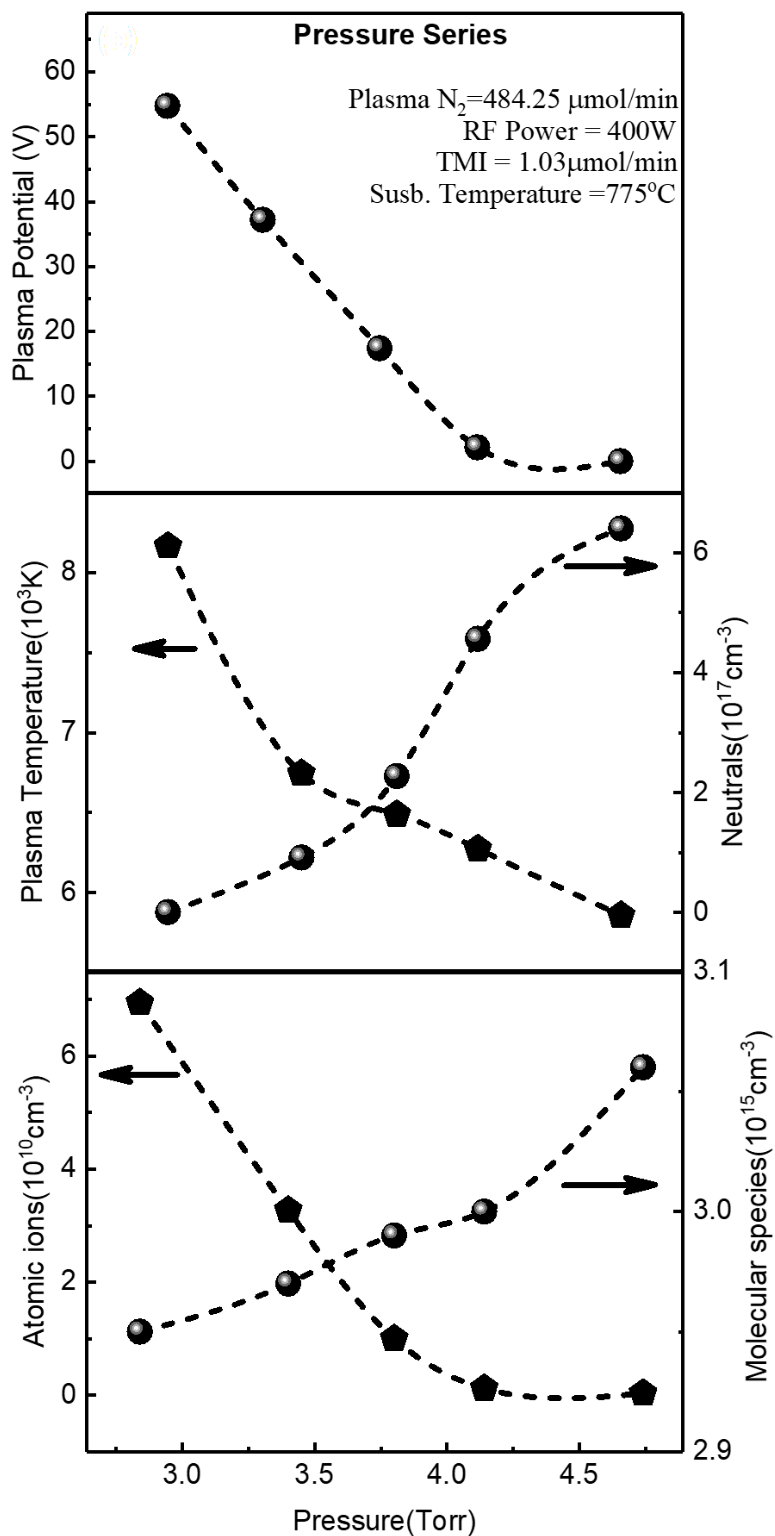

Figure 6.3 Variation in plasma potential and plasma composition with reactor pressure

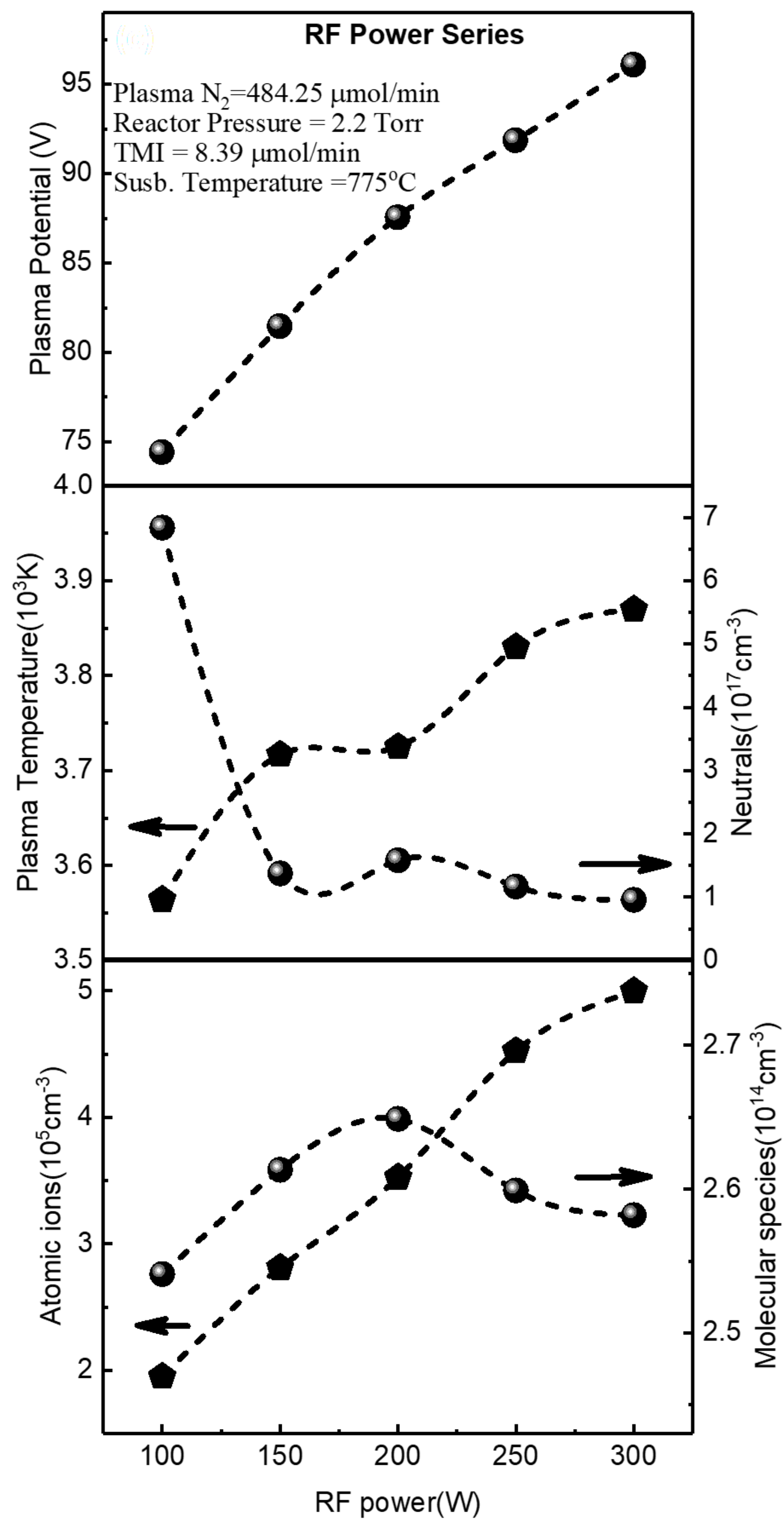

Figure 6.4 Variation in plasma potential and plasma composition with plasma RF power

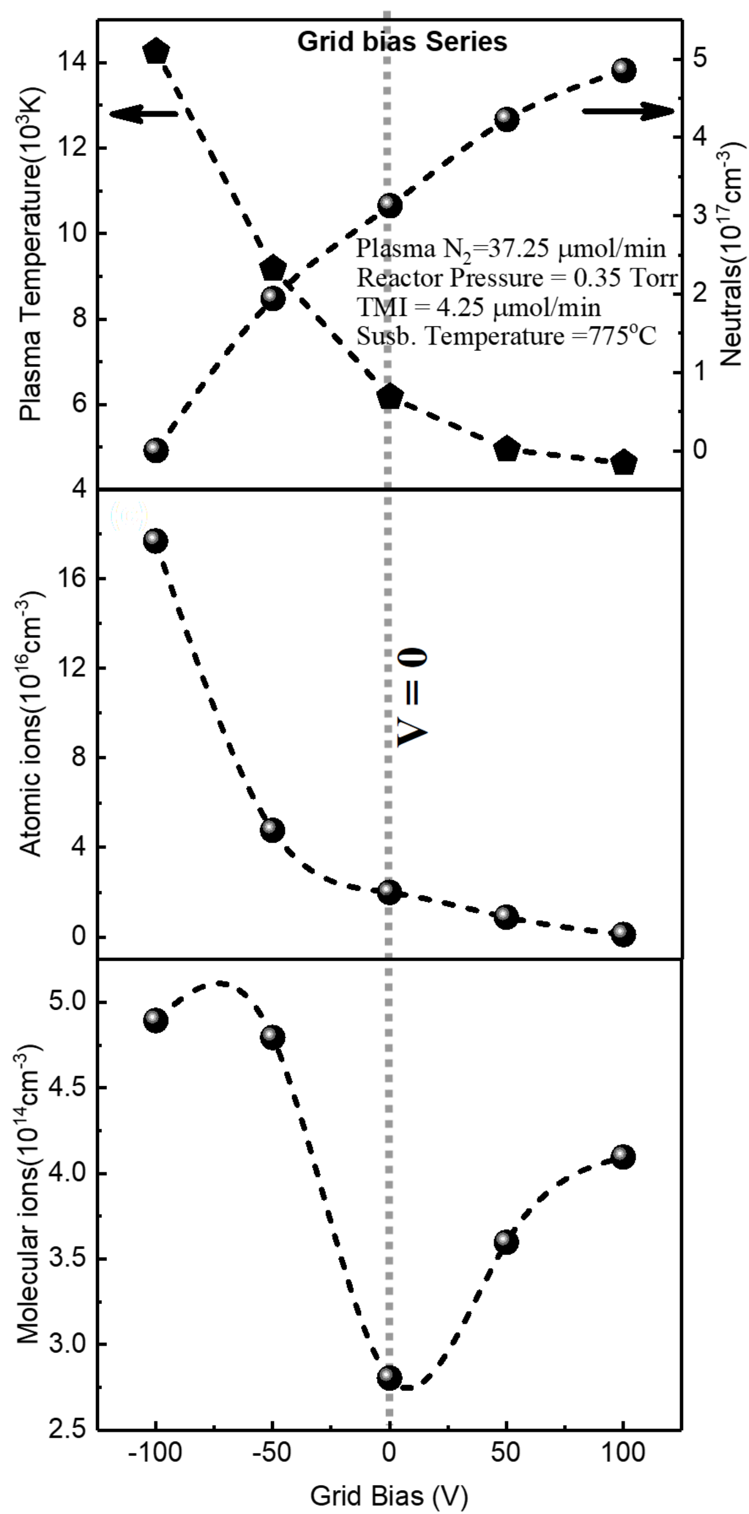

Figure 6.5 Variation in plasma composition with plasma grid bias. V = 0 at the dotted line

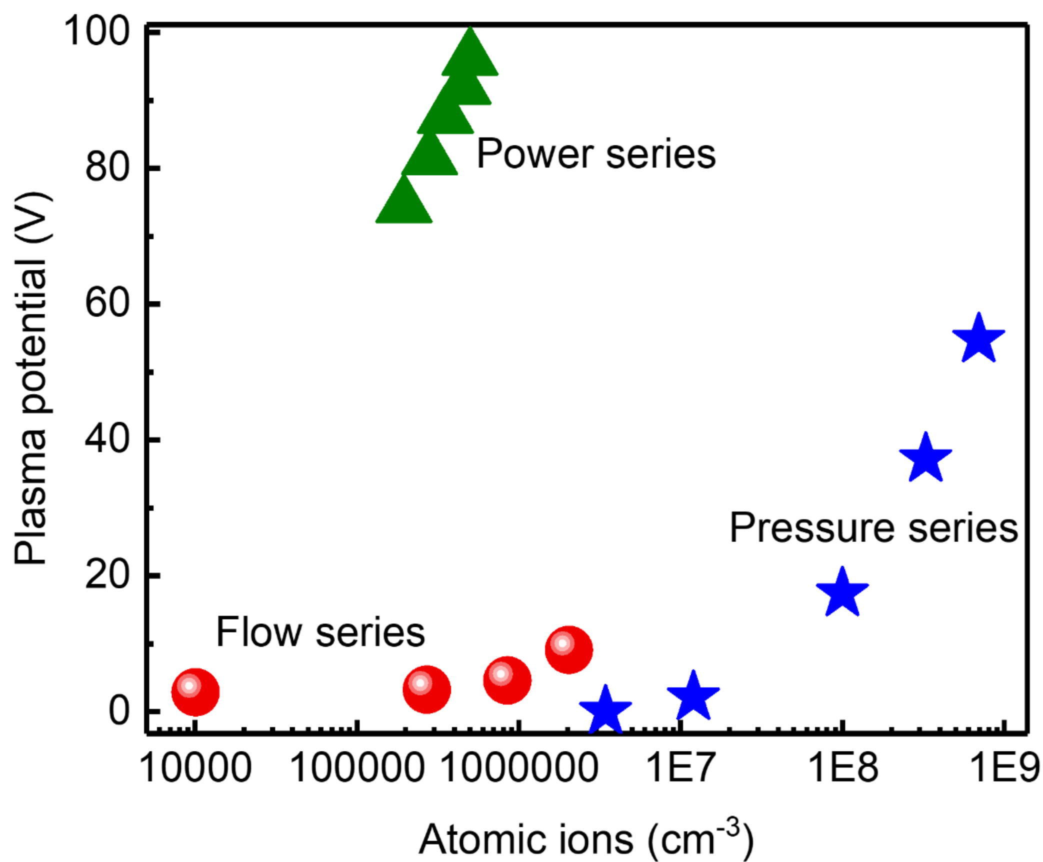

Figure 6.6 The dependence of plasma potential on the concentration of atomic ions

6.5 The impact of plasma potential on structural properties of InN

The influence of plasma potential and grid bias on the structural properties of InN was studied via Raman spectroscopy. Raman spectra for the four sets of InN samples grown at varying

conditions are shown in Figure 6.3. The InN E_2-high (489 cm^{-1}) and A_1-LO (590 cm^{-1}) phonon modes were observed in each of the sample sets.

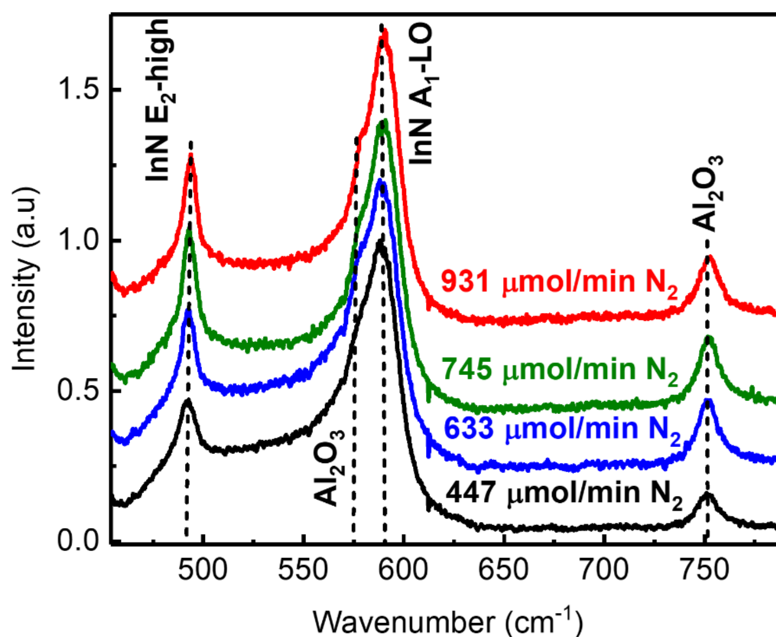

Figure 6.7 Raman spectra for the sample set A

The phonon relaxation time was estimated using the FWHM and peak position of the E_2-high and A1-LO phonon modes extracted from a multi-peak fit of the Raman spectra. Fig. 6.4 shows the E_2-high phonon mode relaxation time as a function of plasma potential for each set of samples. The E_2-high phonon relaxation time increases with the increase in plasma potential within each of the sample sets. Since the plasma potential is directly related to the concentration of atomic nitrogen ions and these species are the primarily contributing[152] to the InN growth, the increase in E_2-high phonon relaxation time is likely to be caused by a decrease in nitrogen vacancies in the grown InN, which are primary contributors to the E_2-high mode[137]. No significant correlation has been observed between the A_1-LO phonon mode relaxation time and the plasma potential.

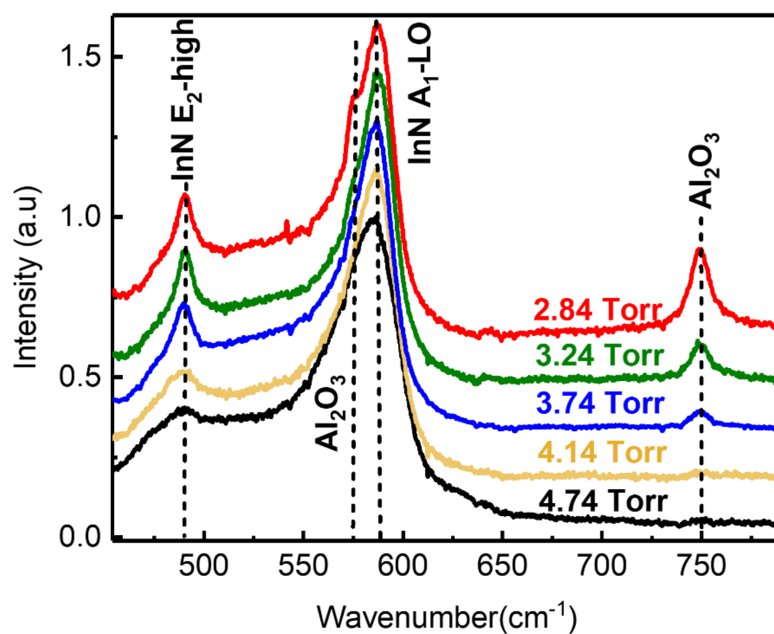

Figure 6.8 Raman spectra for the sample set B

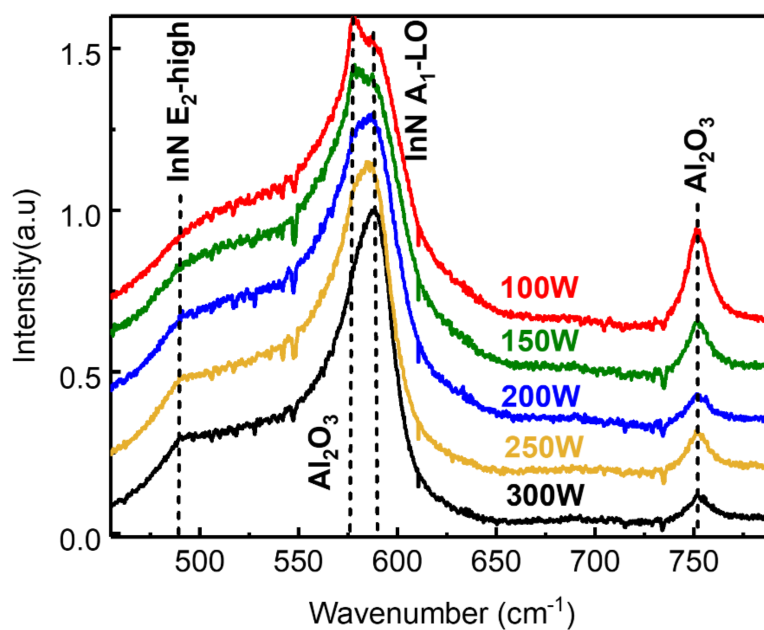

Figure 6.9 Raman spectra for the sample set C

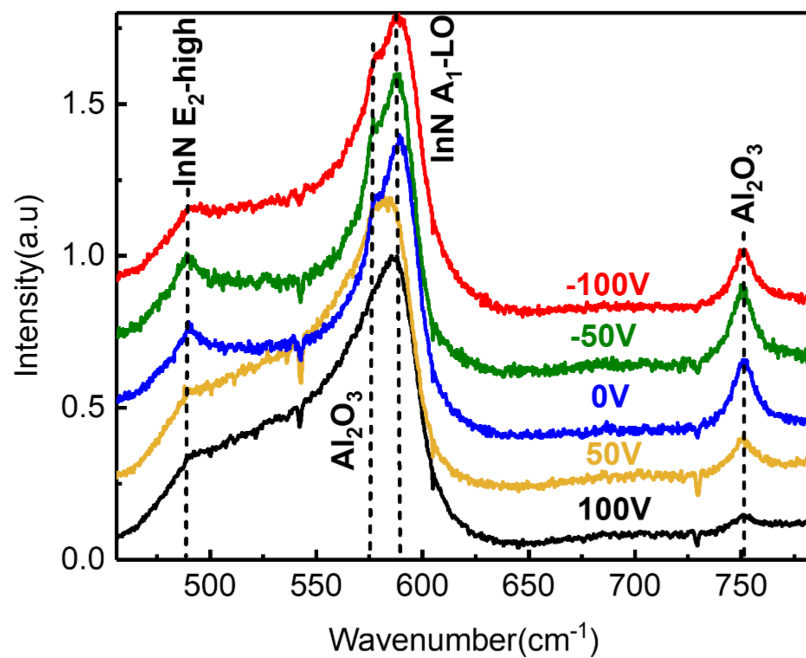

Figure 6.10 Raman spectra for the sample set D

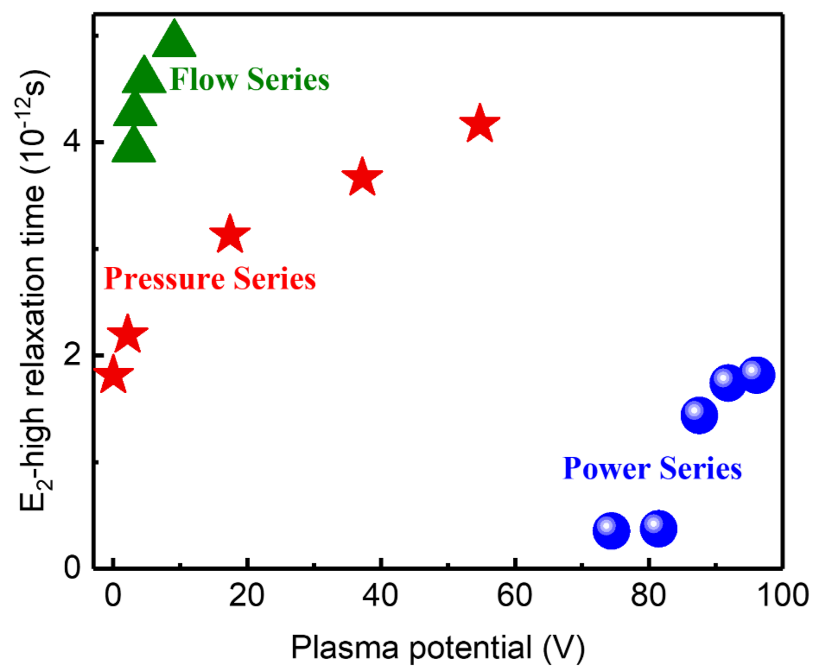

Figure 6.11 The impact of plasma potential on the E2-high phonon mode relaxation time

6.6 Conclusions

The plasma is always at a positive potential with respect to a substrate it is in contact with. In this study the effect of various growth parameters on the plasma potential has been investigated. The plasma potential is found to be in a positive correlation with the concentration of atomic nitrogen ions. For any set of growth parameters, the increase in plasma potential is due to an increase in the concentration of atomic nitrogen ions, and that, in turn, causes to improve the crystalline quality of the InN films grown. These studies also establish the fact that the plasma potential can be used as a qualitative measure of the concentration of atomic nitrogen ions.

7 CONCLUSIONS

InN occurs as wurtzite (hexagonal) or zincblende (cubic) crystal structures. The wurtzite type is thermodynamically stable under ambient conditions. Additionally, a third crystalline form namely rock salt forms as a phase transition from the wurtzite structure at hydrostatic pressure of 21.6 GPa. Each of these structures have optical and structural different properties.

There are many different growth techniques that can be used for InN epitaxy, I have mainly focused on the migration-enhanced plasma-assisted meatal organic chemical vapor deposition (ME-PA-MOCVD) for the growth of InN in this study. Nitrogen plasma and Trimethylindium were used as group V and group III precursors. Characterization of InN films in the present study was performed using Raman spectroscopy, XRD, FTIR and AFM.

The composition of nitrogen plasma, used as the nitrogen precursor, was analyzed using optical emission spectroscopy. The atomic nitrogen ion species were shown to have a dominant impact on the InN growth rate compared to atomic nitrogen neutrals and molecular nitrogen species. The structural quality of the films was characterized by the E_2-high phonon mode relaxation time determined by Raman spectroscopy. InN structural quality was found to depend significantly on the flux of atomic nitrogen ions.

The plasma is always at a positive potential with respect to a substrate it is in contact with. In this study the effect of various growth parameters on the plasma potential has been investigated. The plasma potential is found to be in a positive correlation with the concentration of atomic nitrogen ions. For any set of growth parameters, the increase in plasma potential is due to an increase in the concentration of atomic nitrogen ions, and that, in turn, causes to improve the crystalline quality of the InN films grown. These studies also establish the fact that the plasma potential can be used as a qualitative measure of the concentration of atomic nitrogen ions.

A model of indium supersaturation for the PA-MOCVD process was developed. The Gibbs free energy of the reaction of the reaction is linked to the supersaturation by the equation. The supersaturation depends upon the growth conditions used. Since there are many different combinations of growth parameters that can give the same supersaturation, the films grown at those different conditions belonging to a single value of supersaturation should have similar structural and morphological properties, since the reaction kinetics stay same because of unaltered supersaturation. It was also found experimentally that films that were grown at different growth conditions belonging to the same supersaturation exhibit the similar structural and morphological properties.

This provides us with a better understanding of the InN growth mechanism in PA-MOCVD systems and paves the path for further nitride-based semiconductor growth optimization to achieve industrial-scale high-quality film growth in these systems. The future directions for this work could be to find optimal growth window to optimize growth parameters for high growth rate 2D InN film growth and to controllably grow InN quantum dots at high temperature for InN/GaN heterostructures for electronic / optoelectronic device applications. An example of InN quantum dots grown in MEPA-MOCVD system is shown in Fig. 7.1.

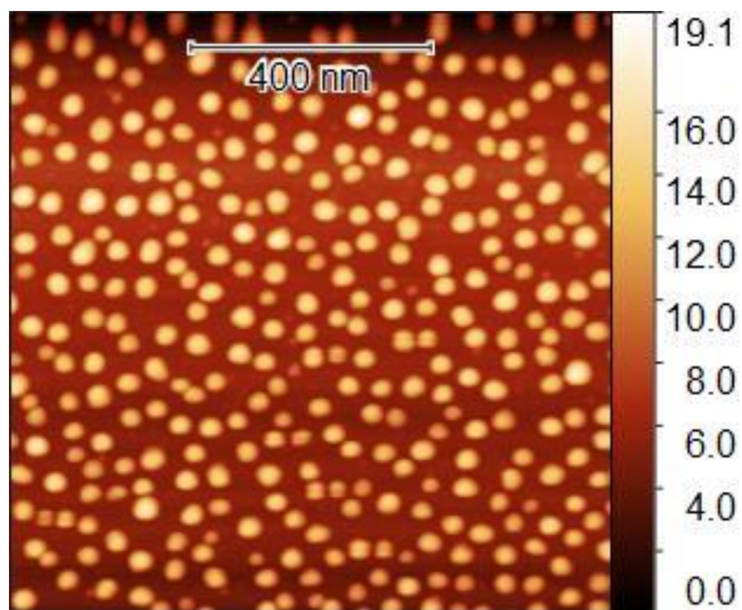

Figure 7.1 InN quantum dots on GaN, grown by migration-enhanced plasma-assisted MOCVD (MEPA-MOCVD)

REFERENCES

1. Trybus, E., et al., *Growth of InN on Ge substrate by molecular beam epitaxy.* Journal of crystal growth, 2005. **279**(3-4): p. 311-315.
2. Akasaki, I., et al., *Conductivity control of GaN and fabrication of UV/blue GaN light emitting devices.* Physica B: Condensed Matter, 1993. **185**(1-4): p. 428-432.
3. Nakamura, S., M. Senoh, and T. Mukai, *P-GaN/N-InGaN/N-GaN double-heterostructure blue-light-emitting diodes.* Japanese Journal of Applied Physics, 1993. **32**(1A): p. L8.
4. Jain, S., et al., *III–nitrides: Growth, characterization, and properties.* Journal of Applied Physics, 2000. **87**(3): p. 965-1006.
5. Mukai, T., M. Yamada, and S. Nakamura, *Characteristics of InGaN-based UV/blue/green/amber/red light-emitting diodes.* Japanese Journal of Applied Physics, 1999. **38**(7R): p. 3976.
6. Zilko, J.L., *Metal organic chemical vapor deposition: technology and equipment*, in *Handbook of thin film deposition processes and techniques*2001, Elsevier. p. 151-203.
7. Seshan, K., *Handbook of Thin Film Deposition Techniques Principles, Methods, Equipment and Applications, Second Editon*2002: CRC Press.
8. Mukai, T., et al., *Recent progress of nitride-based light emitting devices.* physica status solidi (a), 2003. **200**(1): p. 52-57.
9. Narukawa, Y., et al., *Recent progress of high efficiency white LEDs.* physica status solidi (a), 2007. **204**(6): p. 2087-2093.
10. Nakamura, S., et al., *InGaN multi-quantum-well-structure laser diodes with cleaved mirror cavity facets.* Japanese journal of applied physics, 1996. **35**(2B): p. L217.
11. Mohammad, S.N. and H. Morkoç, *Progress and prospects of group-III nitride semiconductors.* Progress in quantum electronics, 1996. **20**(5-6): p. 361-525.
12. Yamamoto, A., et al., *A Comparative Study of MOVPE Growth of InN on GaAs (111) Substrates Using a Nitrided or Grown GaN Buffer Layer.* physica status solidi (a), 1999. **176**(1): p. 595-598.
13. Meziani, Y., et al., *Terahertz investigation of high quality indium nitride epitaxial layers.* physica status solidi (a), 2005. **202**(4): p. 590-592.
14. Lu, H., W.J. Schaff, and L.F. Eastman, *Surface chemical modification of InN for sensor applications.* Journal of applied physics, 2004. **96**(6): p. 3577-3579.
15. Yamamoto, A., et al., *Recent advances in InN-based solar cells: status and challenges in InGaN and InAlN solar cells.* physica status solidi C, 2010. **7**(5): p. 1309-1316.
16. Pollak, F.H., *Effects of homogeneous strain on the electronic and vibrational levels in semiconductors*, in *Semiconductors and Semimetals*1990, Elsevier. p. 17-53.
17. Juza, R. and H. Hahn, *Über die kristallstrukturen von Cu3N, GaN und InN metallamide und metallnitride.* Zeitschrift für anorganische und allgemeine Chemie, 1938. **239**(3): p. 282-287.
18. Juza, R. and H. Hahn, *Über die Nitride der Metalle der ersten Nebengruppen des periodischen Systems. Metallamide und Metallnitride. X. Mitteilung.* Zeitschrift für anorganische und allgemeine Chemie, 1940. **244**(2): p. 133-148.
19. Juza, R. and A. Rabenau, *Das elektrische Leitvermögen einiger Metallnitride.* Zeitschrift für anorganische und allgemeine Chemie, 1956. **285**(3-6): p. 212-220.

20. Renner, T., *Herstellung der Nitride von Bor, Aluminium, Gallium und Indium nach dem Aufwachsverfahren.* Zeitschrift für anorganische und allgemeine Chemie, 1959. **298**(1-2): p. 22-33.
21. Pastrňák, J. and L. Součková, *Herstellung dünner Schichten von Aluminium-, Gallium- sowie Indiumnitrid unter einer Gasentladung.* physica status solidi (b), 1963. **3**(2): p. K71-K74.
22. Acharya, A.R., *Indium nitride surface structure, desorption kinetics and thermal stability.* 2013.
23. Bhuiyan, A.G., A. Hashimoto, and A. Yamamoto, *Indium nitride (InN): A review on growth, characterization, and properties.* Journal of applied physics, 2003. **94**(5): p. 2779-2808.
24. MacChesney, J., P. Bridenbaugh, and P. O'connor, *Thermal stability of indium nitride at elevated temperatures and nitrogen pressures.* Materials Research Bulletin, 1970. **5**(9): p. 783-791.
25. Hovel, H. and J. Cuomo, *Electrical and optical properties of rf-sputtered GaN and InN.* Applied Physics Letters, 1972. **20**(2): p. 71-73.
26. Tansley, T. and C. Foley, *Electron mobility in indium nitride.* Electronics Letters, 1984. **20**(25): p. 1066-1068.
27. Tansley, T. and C. Foley, *Optical band gap of indium nitride.* Journal of Applied Physics, 1986. **59**(9): p. 3241-3244.
28. Marasina, L., I. Pichugin, and M. Tlaczala, *Preparation of InN epitaxial layers in InCl3□ NH3 system.* Kristall und Technik, 1977. **12**(6): p. 541-545.
29. Wakahara, A. and A. Yoshida, *Heteroepitaxial growth of InN by microwave-excited metalorganic vapor phase epitaxy.* Applied physics letters, 1989. **54**(8): p. 709-711.
30. Sato, Y. and S. Sato, *Growth of InN on GaAs substrates by the reactive evaporation method.* Japanese journal of applied physics, 1989. **28**(9A): p. L1641.
31. Blows, J. and D. Tang, *Gratings written with tripled output of Q-switched Nd: YAG laser.* Electronics Letters, 2000. **36**(22): p. 1837-1839.
32. Yamamoto, A., et al., *Characterization of MOVPE-grown InN layers on α-Al2O3 and GaAs substrates.* Journal of crystal growth, 1998. **189**: p. 461-465.
33. Inushima, T., et al., *Physical properties of InN with the band gap energy of 1.1 eV.* Journal of Crystal Growth, 2001. **227**: p. 481-485.
34. Bayerl, D.J., *First-Principles Calculations of Optoelectronic and Transport Properties of Materials for Energy Applications*, 2015.
35. Matsuoka, T., et al., *Optical bandgap energy of wurtzite InN.* Applied Physics Letters, 2002. **81**(7): p. 1246-1248.
36. Jenkins, D.W. and J.D. Dow, *Electronic structures and doping of InN, In x Ga 1− x N, and In x Al 1− x N.* Physical Review B, 1989. **39**(5): p. 3317.
37. Feiler, D., et al., *Pulsed laser deposition of epitaxial AlN, GaN, and InN thin films on sapphire (0001).* Journal of crystal growth, 1997. **171**(1-2): p. 12-20.
38. Butcher, K., et al., *Nitrogen-rich indium nitride.* Journal of Applied Physics, 2004. **95**(11): p. 6124-6128.
39. Nag, B., *Electron mobility in indium nitride.* Journal of crystal growth, 2004. **269**(1): p. 35-40.

40. Fareed, R.Q., et al., *High quality InN/GaN heterostructures grown by migration enhanced metalorganic chemical vapor deposition.* Applied physics letters, 2004. **84**(11): p. 1892-1894.
41. Sato, Y. and S. Sato, *Influence of growth rates on properties of InN thin films.* Journal of crystal growth, 1995. **146**(1-4): p. 262-265.
42. Weyers, M., M. Sato, and H. Ando, *Red shift of photoluminescence and absorption in dilute GaAsN alloy layers.* Japanese Journal of Applied Physics, 1992. **31**(7A): p. L853.
43. Guo, Q., et al., *Deposition of InN thin films by radio frequency magnetron sputtering.* Journal of crystal growth, 1998. **189**: p. 466-470.
44. Ikuta, K., Y. Inoue, and O. Takai, *Optical and electrical properties of InN thin films grown on ZnO/α-Al2O3 by RF reactive magnetron sputtering.* Thin Solid Films, 1998. **334**(1-2): p. 49-53.
45. Yamaguchi, S., et al., *Structural properties of InN on GaN grown by metalorganic vapor-phase epitaxy.* Journal of applied physics, 1999. **85**(11): p. 7682-7688.
46. Bedair, S., et al., *Atomic layer epitaxy of III-V binary compounds.* Applied physics letters, 1985. **47**(1): p. 51-53.
47. McDermott, B., et al., *Atomic layer epitaxy of GaInP ordered alloy.* Applied physics letters, 1990. **56**(12): p. 1172-1174.
48. McIntosh, F., et al., *Epitaxial deposition of GaInN and InN using the rotating susceptor ALE system.* Applied surface science, 1997. **112**: p. 98-101.
49. Inushima, T., T. Shiraishi, and V.Y. Davydov, *Phonon structure of InN grown by atomic layer epitaxy.* Solid State Communications, 1999. **110**(9): p. 491-495.
50. Lu, H., et al., *Improvement on epitaxial grown of InN by migration enhanced epitaxy.* Applied Physics Letters, 2000. **77**(16): p. 2548-2550.
51. Lu, H., et al., *Effect of an AlN buffer layer on the epitaxial growth of InN by molecular-beam epitaxy.* Applied Physics Letters, 2001. **79**(10): p. 1489-1491.
52. Lu, H., et al., *Growth of a-plane InN on r-plane sapphire with a GaN buffer by molecular-beam epitaxy.* Applied physics letters, 2003. **83**(6): p. 1136-1138.
53. Saito, Y., et al., *Growth of high-electron-mobility InN by RF molecular beam epitaxy.* Japanese Journal of Applied Physics, 2001. **40**(2A): p. L91.
54. Qian, Z., et al., *Growth-dependent phonon characteristics in InN thin films.* Physica B: Condensed Matter, 2002. **318**(2-3): p. 180-187.
55. Goldhahn, R., et al., *Anisotropy of the dielectric function for wurtzite InN.* Superlattices and Microstructures, 2004. **36**(4-6): p. 591-597.
56. Kasic, A., et al., *InN dielectric function from the midinfrared to the ultraviolet range.* Physical Review B, 2004. **70**(11): p. 115217.
57. Yang, H., et al., *Optical constants of InN thin films on (111) GaAs grown by reactive magnetron sputtering.* Journal of applied physics, 2002. **91**(12): p. 9803-9808.
58. Yamamoto, A., et al., *Improved electrical properties for metalorganic vapour phase epitaxial InN films.* physica status solidi (a), 2002. **194**(2): p. 510-514.
59. Yamamoto, A., et al., *Nitridation effects of substrate surface on the metalorganic chemical vapor deposition growth of InN on Si and α-Al2O3 substrates.* Journal of crystal growth, 1994. **137**(3-4): p. 415-420.
60. Heinlein, C., et al., *Preconditioning of c-plane sapphire for GaN molecular beam epitaxy by electron cyclotron resonance plasma nitridation.* Journal of applied physics, 1998. **83**(11): p. 6023-6027.

61. Hashimoto, T., et al., *Quantitative study of nitridated sapphire surfaces by x-ray photoelectron spectroscopy.* Journal of applied physics, 1999. **86**(7): p. 3670-3675.
62. Losurdo, M., et al., *Role of sapphire nitridation temperature on GaN growth by plasma assisted molecular beam epitaxy: Part II. Interplay between chemistry and structure of layers.* Journal of applied physics, 2002. **91**(4): p. 2508-2518.
63. Dwikusuma, F. and T.F. Kuech, *X-ray photoelectron spectroscopic study on sapphire nitridation for GaN growth by hydride vapor phase epitaxy: Nitridation mechanism.* Journal of applied physics, 2003. **94**(9): p. 5656-5664.
64. Minor, S.P., *Plasma-Assisted Molecular Beam Epitaxial Growth of Indium Nitride for Future Device Fabrication.* 2012.
65. Nanishi, Y., Y. Saito, and T. Yamaguchi, *RF-molecular beam epitaxy growth and properties of InN and related alloys.* Japanese journal of applied physics, 2003. **42**(5R): p. 2549.
66. Maleyre, B., et al., *Investigation of the influence of buffer and nitrided layers on the initial stages of InN growth on sapphire by MOCVD.* physica status solidi (c), 2005. **2**(7): p. 2309-2315.
67. Drago, M., et al., *InN growth on sapphire using different nitridation procedures.* physica status solidi (a), 2006. **203**(7): p. 1622-1625.
68. Skuridina, D., et al., *Surface and crystal structure of nitridated sapphire substrates and their effect on polar InN layers.* Applied surface science, 2014. **307**: p. 461-467.
69. Xu, K., et al., *Comparative study of InN growth on Ga-and N-polarity GaN templates by molecular-beam epitaxy.* physica status solidi (c), 2003(7): p. 2814-2817.
70. Xie, Z., et al., *The high mobility InN film grown by MOCVD with GaN buffer layer.* Journal of crystal growth, 2007. **298**: p. 409-412.
71. Khludkov, S., I. Prudaev, and O. Tolbanov, *Physical properties of indium nitride, impurities, and defects.* Russian Physics Journal, 2014. **56**(9): p. 997-1006.
72. Himmerlich, M., et al., *N-type conductivity and properties of carbon-doped InN (0001) films grown by molecular beam epitaxy.* Journal of Applied Physics, 2013. **113**(3): p. 033501.
73. Baghani, E. and S.K. O'Leary, *Electron mobility limited by scattering from screened positively charged dislocation lines within indium nitride.* Applied Physics Letters, 2011. **99**(26): p. 262106.
74. Miller, N., et al., *Effect of charged dislocation scattering on electrical and electrothermal transport in n-type InN.* Physical Review B, 2011. **84**(7): p. 075315.
75. Wu, J., *When group-III nitrides go infrared: New properties and perspectives.* Journal of Applied Physics, 2009. **106**(1): p. 5.
76. Gorczyca, I., et al., *Band gap engineering of In (Ga) N/GaN short period superlattices.* Scientific reports, 2017. **7**(1): p. 1-9.
77. Christensen, N. and I. Gorczyca, *Optical and structural properties of III-V nitrides under pressure.* Physical Review B, 1994. **50**(7): p. 4397.
78. Ambacher, O., *Growth and applications of group III-nitrides.* Journal of Physics D: Applied Physics, 1998. **31**(20): p. 2653.
79. Ruterana, P., M. Albrecht, and J. Neugebauer, *Nitride semiconductors.* Handbook on Materials and Devices, 2003.

80. People, R. and J. Bean, *Calculation of critical layer thickness versus lattice mismatch for Ge x Si1− x/Si strained-layer heterostructures.* Applied Physics Letters, 1985. **47**(3): p. 322-324.
81. Hu, S., *Misfit dislocations and critical thickness of heteroepitaxy.* Journal of applied physics, 1991. **69**(11): p. 7901-7903.
82. Wen, K., W. Lv, and W. He, *Interfacial lattice-strain effects on improving the overall performance of micro-solid oxide fuel cells.* Journal of Materials Chemistry A, 2015. **3**(40): p. 20031-20050.
83. Morkoç, H., *Handbook of nitride semiconductors and devices, Materials Properties, Physics and Growth*. Vol. 1. 2009: John Wiley & Sons.
84. Matara Kankanamge, I., *Optoelectronic and Structural Properties of Group III-Nitride Semiconductors Grown by High Pressure MOCVD and Migration Enhanced Plasma Assisted MOCVD.* 2016.
85. Punya, A. and W.R. Lambrecht, *Valence band effective-mass Hamiltonians for the group-III nitrides from quasiparticle self-consistent G W band structures.* Physical Review B, 2012. **85**(19): p. 195147.
86. Rinke, P., et al., *Consistent set of band parameters for the group-III nitrides AlN, GaN, and InN.* Physical Review B, 2008. **77**(7): p. 075202.
87. Yoshida, S., et al., *Fundamental Properties of Wide Bandgap Semiconductors*, in *Wide Bandgap Semiconductors*2007, Springer. p. 25-96.
88. MK, I.S., et al. *Effect of AlN buffer layers on the structural and optoelectronic properties of InN/AlN/Sapphire heterostructures grown by MEPA-MOCVD*. in *Fifteenth International Conference on Solid State Lighting and LED-based Illumination Systems*. 2016. International Society for Optics and Photonics.
89. Hummel, R.E., *Electronic properties of materials*2011: Springer Science & Business Media.
90. Millot, M., et al., *Determination of effective mass in InN by high-field oscillatory magnetoabsorption spectroscopy.* Physical Review B, 2011. **83**(12): p. 125204.
91. Goiran, M., et al., *Electron cyclotron effective mass in indium nitride.* Applied physics letters, 2010. **96**(5): p. 052117.
92. Davydov, V.Y., et al., *Phonon dispersion and Raman scattering in hexagonal GaN and AlN.* Physical Review B, 1998. **58**(19): p. 12899.
93. Bergman, L., et al., *Raman analysis of phonon lifetimes in AlN and GaN of wurtzite structure.* Physical Review B, 1999. **59**(20): p. 12977.
94. Gao, F., et al., *Epitaxial growth and interfaces of high-quality InN films grown on nitrided sapphire substrates.* Journal of Materials Research, 2013. **28**(9): p. 1239-1244.
95. Venables, J., *Introduction to surface and thin film processes*2000: Cambridge University Press.
96. Pimpinelli, A. and J. Villain, *Physics of crystal growth*. Vol. 19. 1998: Cambridge university press Cambridge.
97. Oura, K., et al., *Surface science: an introduction*2013: Springer Science & Business Media.
98. Herman, M.A., W. Richter, and H. Sitter, *Epitaxy: physical principles and technical implementation*. Vol. 62. 2013: Springer Science & Business Media.
99. Stringfellow, G.B., *Organometallic vapor-phase epitaxy: theory and practice*1999: Elsevier.

100. Ludowise, M., *Metalorganic chemical vapor deposition of III-V semiconductors.* Journal of Applied Physics, 1985. **58**(8): p. R31-R55.
101. Stringfellow, G., *A critical appraisal of growth mechanisms in MOVPE.* Journal of Crystal Growth, 1984. **68**(1): p. 111-122.
102. Dapkus, P.D., *Metalorganic chemical vapor deposition.* Annual Review of Materials Science, 1982. **12**(1): p. 243-269.
103. Don, W. *Kinetic aspects in the vapour phase epitaxy of III-V compounds*. in *Vapour Growth and Epitaxy: Proceedings of the Third International Conference on Vapour Growth and Epitaxy, Amsterdam, The Netherlands, 18–21 August 1975*. 2013. Elsevier.
104. McGill, L.M., *MOCVD growth of In GaP-based heterostructures for light emitting devices*, 2004, Massachusetts Institute of Technology.
105. Moss, R., *Adducts in the growth of III–V compounds.* Journal of Crystal Growth, 1984. **68**(1): p. 78-87.
106. Roberts, J., N. Mason, and M. Robinson, *Factors influencing doping control and abrupt metallurgical transitions during atmospheric pressure MOVPE growth of AlGaAs and GaAs.* Journal of Crystal Growth, 1984. **68**(1): p. 422-430.
107. Thrush, E., et al., *Evidence for transient composition variations at GaAs/Ga 1− x Al x As heterostructure interfaces prepared by metal-organic chemical vapour deposition.* Journal of electronic materials, 1984. **13**(6): p. 969-988.
108. Dapkus, P., et al., *High purity GaAs prepared from trimethylgallium and arsine.* Journal of Crystal Growth, 1981. **55**(1): p. 10-23.
109. Manasevit, H., *Recollections and reflections of MO-CVD.* Journal of Crystal Growth, 1981. **55**(1): p. 1-9.
110. Dimitrova, V., D. Manova, and E. Valcheva, *Optical and dielectric properties of dc magnetron sputtered AlN thin films correlated with deposition conditions.* Materials Science and Engineering: B, 1999. **68**(1): p. 1-4.
111. Smekal, A., *Zur quantentheorie der dispersion.* Naturwissenschaften, 1923. **11**(43): p. 873-875.
112. Opel, M., F. Venturini, and B.A. der Wissenschaften, *Raman scattering in solids.* European Pharmaceutical Review, 2002. **7**(3): p. 76-82.
113. Raman, C.V. and K.S. Krishnan, *A new type of secondary radiation.* Nature, 1928. **121**(3048): p. 501-502.
114. Prasankumar, R.P. and A.J. Taylor, *Optical techniques for solid-state materials characterization*2016: CRC Press.
115. Flurry, R.L., *Symmetry groups: theory and chemical applications*1980: Prentice Hall.
116. Gil, B., *Physics of Wurtzite Nitrides and Oxides.* Physics of Wurtzite Nitrides and Oxides: Passport to Devices, Springer Series in Materials Science, Volume 197. ISBN 978-3-319-06804-6. Springer International Publishing Switzerland, 2014, 2014.
117. Atkins, P.W. and R.S. Friedman, *Molecular quantum mechanics*2011: Oxford university press.
118. Stroscio, M.A. and M. Dutta, *Phonons in nanostructures*2001: Cambridge University Press.
119. Henry, D., et al., *X-ray reflection in accordance with Bragg's Law.* Science Education Recearch Center, 2012.
120. Moram, M. and M. Vickers, *X-ray diffraction of III-nitrides.* Reports on progress in physics, 2009. **72**(3): p. 036502.

121. Geisse, N.A., *AFM and combined optical techniques.* Materials today, 2009. **12**(7-8): p. 40-45.
122. Camacho, J., et al., *Optical emission studies of nitrogen plasma generated by IR CO2 laser pulses.* Journal of Physics B: Atomic, Molecular and Optical Physics, 2007. **40**(24): p. 4573.
123. Voulot, D., et al., *Determination of the atomic nitrogen flux from a radio frequency plasma nitride source for molecular beam epitaxy systems.* Journal of Vacuum Science & Technology A: Vacuum, Surfaces, and Films, 1998. **16**(6): p. 3434-3437.
124. Iliopoulos, E., et al., *Active nitrogen species dependence on radiofrequency plasma source operating parameters and their role in GaN growth.* Journal of crystal growth, 2005. **278**(1-4): p. 426-430.
125. Kikuchi, T., et al., *Role of excited nitrogen species in the growth of GaN by RF–MBE.* Journal of crystal growth, 2006. **292**(2): p. 221-226.
126. Agarwal, S., et al., *Absolute densities of N and excited N 2 in a N 2 plasma.* Applied physics letters, 2003. **83**(24): p. 4918-4920.
127. Grün, M., et al., *Doping efficiency and plasma analysis of a nitrogen electron cyclotron resonance plasma.* Journal of crystal growth, 1996. **159**(1-4): p. 284-288.
128. Newman, N., *The energetics of the GaN MBE reaction: a case study of meta-stable growth.* Journal of crystal growth, 1997. **178**(1-2): p. 102-112.
129. Drellishak, K.S., *Partition functions and thermodynamic properties of high temperature gases*, 1964, NORTHWESTERN UNIV EVANSTON ILL.
130. Drellishak, K., D. Aeschliman, and A.B. Cambel, *Partition functions and thermodynamic properties of nitrogen and oxygen plasmas.* The Physics of Fluids, 1965. **8**(9): p. 1590-1600.
131. Ralchenko, Y., et al., *NIST Atomic Spectra Database (version 3.0. 1) URL: http://physics. nist. gov National Institute of Standards and Technology, Gaithersburg*, 2006, MD.
132. Borgia, I., et al., *Self-calibrated quantitative elemental analysis by laser-induced plasma spectroscopy: application to pigment analysis.* Journal of Cultural Heritage, 2000. **1**: p. S281-S286.
133. Miziolek, A.W., V. Palleschi, and I. Schechter, *Laser induced breakdown spectroscopy*2006: Cambridge university press.
134. Grifoni, E., et al., *Extracting time-resolved information from time-integrated laser-induced breakdown spectra.* Journal of Spectroscopy, 2014. **2014**.
135. McWhirter, R., *Plasma Diagnostic Techniques ed RH Huddlestone and SL Leonard (New York: Academic).* 1965.
136. Smith, P.L., et al., *Commission 14: Atomic and Molecular Data 1:(Donnees Atomiques Et Moleculaires).* Transactions of the International Astronomical Union, 2002. **25**(1): p. 381-419.
137. Domènech-Amador, N., et al., *Raman scattering study of anharmonic phonon decay in InN.* Physical Review B, 2011. **83**(24): p. 245203.
138. Mukherjee, D., et al., *Carrier-mediated interaction of magnetic moments in oxygen vacancy–controlled epitaxial Mn-doped ZnO thin films.* Journal of Applied Physics, 2012. **111**(7): p. 07C318.
139. Crafts, P., *The role of solubility modeling and crystallization in the design of active pharmaceutical ingredients*, in *Computer Aided Chemical Engineering*2007, Elsevier. p. 23-85.

140. Mita, S., et al., *Influence of gallium supersaturation on the properties of GaN grown by metalorganic chemical vapor deposition.* Journal of Applied Physics, 2008. **104**(1): p. 013521.
141. Koukitu, A., et al., *Thermodynamic study on the role of hydrogen during the MOVPE growth of group III nitrides.* Journal of crystal growth, 1999. **197**(1-2): p. 99-105.
142. Scherrer, P., *Bestimmung der inneren Struktur und der Größe von Kolloidteilchen mittels Röntgenstrahlen*, in *Kolloidchemie Ein Lehrbuch*1912, Springer. p. 387-409.
143. Zhang, Z., F. Zhou, and E. Lavernia, *On the analysis of grain size in bulk nanocrystalline materials via X-ray diffraction.* Metallurgical and Materials Transactions A, 2003. **34**(6): p. 1349-1355.
144. Indika Senevirathna, M., et al., *Effect of reactor pressure on the electrical and structural properties of InN epilayers grown by high-pressure chemical vapor deposition.* Journal of Vacuum Science & Technology A: Vacuum, Surfaces, and Films, 2012. **30**(3): p. 031511.
145. Harsha, K.S., *Principles of vapor deposition of thin films*2005: Elsevier.
146. Lieberman, M.A. and A.J. Lichtenberg, *Principles of plasma discharges and materials processing*2005: John Wiley & Sons.
147. Panagopoulos, T. and D.J. Economou, *Plasma sheath model and ion energy distribution for all radio frequencies.* Journal of Applied Physics, 1999. **85**(7): p. 3435-3443.
148. Miller, P.A. and M.E. Riley, *Dynamics of collisionless rf plasma sheaths.* Journal of applied physics, 1997. **82**(8): p. 3689-3709.
149. Cross, G.B., et al., *Kinetically stabilized high-temperature InN growth.* Journal of Crystal Growth, 2020: p. 125574.
150. Mozetic, M., et al., *An iron catalytic probe for determination of the O-atom density in an Ar/O 2 afterglow.* Plasma chemistry and plasma processing, 2006. **26**(2): p. 103.
151. Xu, S. and I. Jones, *An experimental investigation of the toroidal magnetic field structure of a rotamak discharge.* Plasma physics and controlled fusion, 1993. **35**(4): p. 531.
152. Ahmad, Z., et al., *Influence of plasma-activated nitrogen species on PA-MOCVD of InN.* Applied Physics Letters, 2019. **115**(22): p. 223101.
153. *Https://Commons.wikimedia.org/Wiki/File:AFM_schematic_(EN)*